Thermal Energy Conversion in Nanofluids

by

Robert Taylor

A Dissertation Presented in Partial Fulfillment
of the Requirements for the Degree
Doctor of Philosophy

Approved, July 2011 by the
Graduate Supervisory Committee:

Patrick E. Phelan, Chair
Ronald Adrian
Steven Trimble
Jonathan Posner
George Maracas

ARIZONA STATE UNIVERSITY

August 2011

ABSTRACT

A relatively simple subset of nanotechnology – nanofluids – can be obtained by adding nanoparticles to conventional base fluids. The promise of these fluids stems from the fact that relatively low particle loadings (typically <1% volume fractions) can significantly change the properties of the base fluid. This research explores how low volume fraction nanofluids, composed of common base-fluids, interact with light energy. Comparative experimentation and modeling reveals that absorbing light volumetrically (i.e. in the depth of the fluid) is fundamentally different from surface-based absorption. Depending on the particle material, size, shape, and volume fraction, a fluid can be changed from being mostly transparent to sunlight (in the case of water, alcohols, oils, and glycols) to being a very efficient volumetric absorber of sunlight. This research also visualizes, under high levels of irradiation, how nanofluids undergo interesting, localized phase change phenomena. For this, images were taken of bubble formation and boiling in aqueous nanofluids heated by a hot wire and by a laser. Infrared thermography was also used to quantify this phenomenon. Overall, though, this research reveals the possibility for novel solar collectors in which the working fluid directly absorbs light energy and undergoes phase change in a single step. Modeling results indicate that these improvements can increase a solar thermal receiver's efficiency by up to 10%.

ACKNOWLEDGMENTS

First and foremost, I would like to thank my wife, Carissa, for sharing in the PhD pursuit with me. Without her support, guidance, and proof-reading, this effort would not have been possible. I would also like to thank the rest of my family for ~30 years of encouragement in my educational pursuits. Special thanks to Dr. Phelan, Dr. Adrian, and Dr. Otanicar for coming up with great ideas and advising me throughout this process. I'd also like to acknowledge the rest of my committee, Steve Trimble, Jonathan Posner, and George Maracas for giving me a constant supply of fresh ideas and interesting/tough questions to ponder. I would also like to thank my 'lab mates' - Mark, Himanshu, Yeshpal, Lucia, Andrey, Willie, Nate, Mark, and Brent - for all the great discussions, support, and help along the way. Finally, I gratefully acknowledge the National Science Foundation (CBET-0932720) for their gracious support which made this research possible. Universally, though, I want to say that I appreciate everyone who devoted their precious time and resources to this project.

TABLE OF CONTENTS PAGE

LIST OF TABLES PAGE

LIST OF FIGURES

FIGURE PAGE

NOMENCLATURE

A	Area (m^2)
c_p	Specific heat : J kg^{-1} °C^{-1}
c	Speed of light (m/s)
C	Concentration ratio
d	Distance (m)
D	Mean particle diameter (nm)
f	Focal length, mm
f_v	Volume fraction (%)
G	Incident solar flux (W m^{-2})
h	Heat transfer coefficient, W/(m^2 °C)
h	Planck's constant (m^2 kg / s)
I	Irradiance (W m^{-2})
k	Thermal conductivity, (W $m^{-1}K^{-1}$)
k_B	Boltzmann's constant (m^2 kg s^{-2} K^{-1})
L	Length (m)
m	Mass flow rate (kg s^{-1})
q”	Heat flux (W/m^2)
R	Thermal resistance (K/W)
ℜ	Reflectance
S	Spectral irradiation (W/m^2)
T	Temperature (^oC)
U	Fluid velocity (m s^{-1})

x	Layer thickness (m)
y	Length (m)

Subscripts

∞	Far away (ambient)
abs	Absorption
Amb	Ambient
c	Cold
cd	Conduction
cv	Convection
e	Electric
eff	Effective
f	Fluid
g	Glazing
h	Hot
HX	Heat exchanger
i	Counter
in	Inlet
j	Incident
o	Outer
out	Outlet
p	Particle
ref.	Reference (room conditions)

sat. Saturation temperature

sf Surface

v Vapor

V Volume

w Wall

Greek Symbols

Δ Change

ε Emissivity

η Efficiency

λ Wavelength, nm

ρ Density (kg/m^3)

σ Extinction coefficient (1/cm)

CHAPTER 1: INTRODUCTION

Energy systems in modern industrial societies are currently fueled almost entirely by fossil resources (EIA, 2010). This fossil foundation is unstable in the long term because fossil resources are non-renewable on human time scales. That is, human society consumes these resources at a much faster rate than they are replaced by geologic processes. This simple fact indicates that yearly production of these fossil resources must eventually reach an unavoidable peak. Also, with most resources the 'lowest hanging fruit' is picked first - this is happening with our energy resources as well. That is, over the last several decades the best, cheapest, and easiest-to-extract fossil resources have been collected leaving the low quality, costly, harder-to-get resources. Mining and drilling companies are continually inventing methods to harvest the remaining resources. This is evident in many deep water drilling, hydraulic fracturing, and complicated deep underground coal mining techniques. Couple this paradigm shift with an exponentially increasing world population (Bureau, 2010) *and* per capita energy usage (BP, 2010) and it becomes very hard for energy supply to keep pace with demand.

Eventually the rate of extraction of fossil resources must reach a peak, however the timeframe of this peak is controversial. Some energy analysts say world production of petroleum (and possibly natural gas) has peaked already or

will peak within 5 years (Gilbert & Perl, 2010), (Heinberg, 2010), and (Simmons, 2006). These analyses also say coal is uncomfortably close to reaching a world peak in production - i.e. within a few short decades. Others, like the United States Energy Information Agency (EIA, 2010), expect fossil fuel production to continue expanding for several decades. Regardless of the timing, however, future global energy demand will rise above the level that our dwindling geological bank of oil, gas, and coal fuel can meet. In the all-too-near future, people will be faced with the choice of paying increasingly exorbitant and volatile prices for energy and investment in new means of primary energy production. Either way, large sums of money will be necessary to meet future energy needs.

I suggest, as a matter of practicality, that countries with the means to do it (such as the United States), commit themselves to developing some new cost-effective technologies based on renewable resources. This presents not only a solution to a colossal challenge, but may also lead to a whole host of opportunities for economic development. Renewable energy represents a path towards harnessing a *vast* amount of energy which humans had no means to directly control until relatively recently. This path is paved by the astonishing quantity of (largely untapped) available solar energy. If, for example, the amount of solar energy hitting the earth were packed in a 1 L bottle, we would only need ~0.07 mL of it to meet the ***world's*** energy demand. That is, if humanity could collect

and use only **~ 0.007%** of freely delivered solar energy, fossil fuels could be completely replaced!

Make no mistake, this is a *huge* economic opportunity. Cumulative yearly revenues of the top utility energy companies are over 160 billion USD, with the largest players (Excelon, AES Corporation, Dominion, and Constellation Energy) pulling in around $15 billion each (EconStats, 2010). If possible, these companies look diminutive compared to oil companies like Exxon Mobil, Shell, and BP who combined gross around $300 billion/year in recent years (EconStats, 2010). Since there are about 70 million new people in the world each year (US Census Bureau, 2010) and some very rapidly developing countries - e.g. China and India - the dollars involved are guaranteed to grow.

All this to say that growth in the solar energy sector is a very safe bet. One clear way for engineers (like myself) to participate in this market is by developing novel solar technologies. New materials which selectively absorb solar energy and minimize losses are continually being developed (Thirugnanasambandam, Iniyan, & Goic, 2010). This development extends even into 'nano'-engineered materials which are being used to make "step-changes in the development of novel solar systems" (N. S. Lewis, 2007). Therefore, the central motivation of this research is to find a way in which new nanotechnology can potentially enable more efficient solar systems and to help these systems become more prevalent. One particular type of nanotechnology, 'nanofluids' -

nanoparticles suspended in conventional fluids, is discussed in this manuscript. That is, this research will explore the possibility of adding nanoparticles to solar thermal working fluids to improve solar collector performance. The central question of this research can be stated as: ***can nanofluids provide a more efficient coupling between a solar input and the final thermal utilization system***? If the answer is yes, and *if* it can be done economically, jobs might be created, our air can be cleaner, and countries employing this technology can become more energy independent.

1.1 The Solar Resource

As mentioned above, the potential solar resource available is enormous and largely undeveloped. Rather than importing energy from other countries, I believe a large share of future energy efforts and investments should, and most likely will, be directed towards expanding the use of solar energy. To provide a feel for the enormity of the domestic solar resource, consider that the lower 48 states receives over 13 quadrillion kW-h/year (NREL, 2010a). This amount is almost 500 times the U.S. annual energy consumption (DOE, 2008). This fact alone demonstrates that solar energy harvesting in the U.S. is constrained by our ability to collect and store it - *not by the resource itself.*

This is especially true in the desert southwest portion of the United States which (with adequate investment) can potentially harvest enough solar energy to provide electrical power to the rest of the United States (NREL, 2010a). Figure 1

shows the solar resource in this region - modified from (NREL, 2010b). The bounded region shows the range where the solar resource is high enough to consider large-scale solar thermal systems. Note: shading in the figure represents varying amounts of direct normal incident solar flux, ranging from 5.5-8 kW-h/m^2/day. That is, a solar collector with a normal area of 1 m^2 will intercept 5.5-8 kW-hrs. of energy in a day in these regions. Of course, only a portion of this land is viable for commercial solar developments - much of the terrain is too rugged, too mountainous, and/or already in use for other purposes. Environmental concerns also present a major barrier to solar installations. Adequate planning and attention must be paid to habitat preservation in fragile desert ecological systems for commercial solar systems to successfully be constructed. Excluding ecologically critical sites, such as migratory paths, nesting areas, etc., there is still ample untapped, high-irradiance land which is suitable for solar projects.

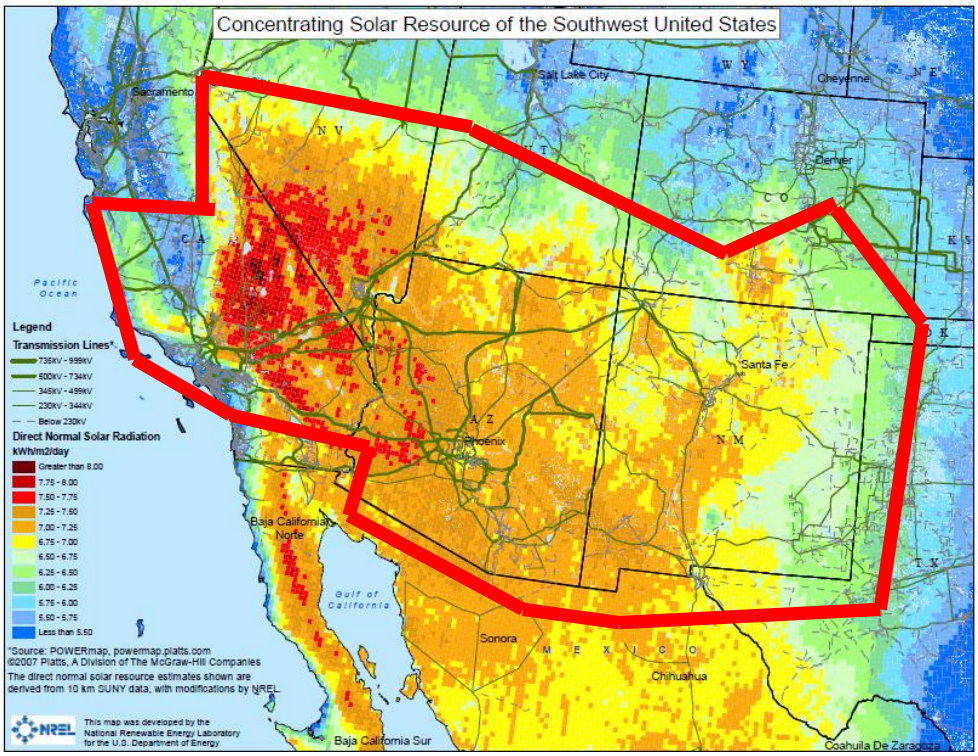

Figure 1. Direct normal solar radiation map - modified from (NREL, 2010b)

1.2 The Case for Solar Thermal

Right now there are two basic categories into which solar energy collection can be lumped – photovoltaic (PV) systems and thermal systems. This research is directed towards efficient collection of high quality *thermal* energy from the sun. One major reason for perusing thermal systems is that they can make use of more of the solar spectrum than photovoltaic systems. Depending on the absorbing medium, over 95% of the incoming radiation to the receiver can be absorbed. Photovoltaic solar systems, however, are limited by their built-in band gap - which is based on their bulk materials and dopants. That is, photons

(packets of light energy) must be of high enough energy to 'bump' electrons up to higher energy levels in a photovoltaic cell. If the photons are of lower energy (i.e. longer wavelength) they will be simply absorbed as low grade heat. If too much heat is absorbed in a photovoltaic cell, the cell efficiency can significantly drop. Figure 2 shows the AM1.5 direct normal radiation, which is a good approximation to the spectrum reaching the ground in most sunny locations (Gueymard, 2001). Figure 2 also breaks up the spectrum roughly into portions which are effectively used by the different solar systems.

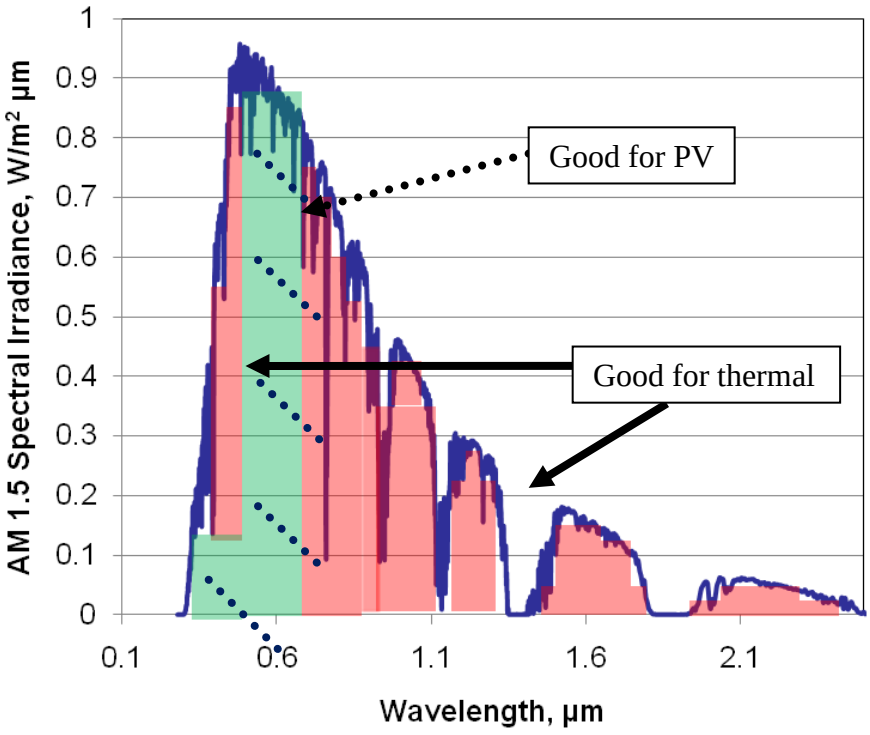

Figure 2. Solar spectrum with PV and thermal highlights - modified from (Gueymard, 2001).

Figure 3 shows, roughly, how the energy is broken down into wavelength / color. As such, Figure 3 is essentially an integrated form of

Figure 2. From these figures we can see that even if a hybrid PV / thermal system is used, the thermal system would actually end up utilizing about twice as much energy as a PV system alone.

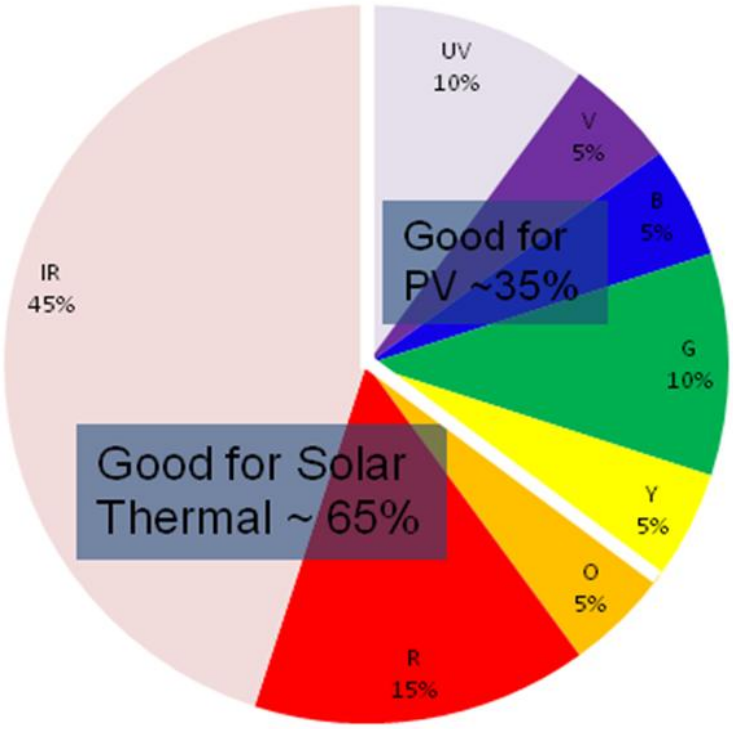

Figure 3. Energy breakdown of the solar spectrum - raw data from (Duffie & Beckman, 2006)**.**

As a further benefit, solar thermal systems can easily store energy - via insulated tanks - which allows them to better meet peak power demand. Storage also helps solar thermal resist harmful transients from weather and shading. Thus,

thermal storage increases reliability and reduces the amount of ancillary costs that can arise from non-dispatchable resources.

For the above reasons, and many others, solar thermal harvesting has been garnering significant interest and investment (Thirugnanasambandam et al., 2010). Solar thermal energy can be harvested for any number of applications - vastly differing in the level of technological sophistication. In its simplest form solar thermal energy can be used passively to do things like dry food/clothes, desalinate water, and heat houses/pools (Duffie & Beckman, 2006). For these applications little to no capital investment is needed to capture what is generally un-concentrated solar energy. Progressing to more active solar thermal technologies, solar energy can be used to cook food, heat water, and provide heat for industrial processes (Duffie & Beckman, 2006). For these applications temperatures well above the ambient and some form of physical collector are required. These technologies may, in many cases, concentrate the incoming solar radiation.

The following research, however, is primarily on the high technological side, which can exploit highly concentrated / high temperature solar thermal energy. To be economic in large scale projects (such as power plants) thermal energy must be of high quality - i.e. in temperature ranges of 300^{o}C and up. That is, solar thermal Rankine cycle power plants and thermo-chemical reactors

become technologically and economically feasible in these temperature ranges (Duffie & Beckman, 2006).

In general, these types of solar applications go through the following steps: 1) sunlight must first be concentrated via some form of optical component(s), 2) the concentrated radiation must be absorbed (i.e. converted to heat) on/in a receiver, 3) thermal energy needs to be moved/transferred through the working medium(s), and then 4) the energy is converted into its final composition - notably electricity, but hydrogen, methanol, metal oxide, or other chemical/manufactured products are also possible. The fourth and final step results in a directly useful form of energy. It should be noted that during step 3, the solar input becomes indistinguishable from a conventional fossil / geothermal / nuclear thermal source. Thus, most existing thermal systems could theoretically be converted to 'run' on solar energy. Because of this variety, there are a number of options which are currently in production for concentrating solar energy. The next section will give a quick summary of solar thermal technologies.

1.3 Solar Thermal Collector Technology Characterization

Anything that is exposed to solar radiation can be called a solar collector. Everything from man-made structures and forests to bodies of water and even snow/ice all end up collecting some solar thermal energy. However, active, modern technology is needed to economically generate electricity or to make

high-value products from solar driven chemical reactions. Thus, we will limit our discussion to these technologies.

Active solar collectors can be categorized by their optical concentration method. As a first cut, solar concentrators can be conceptualized as reflective (i.e. the light is directed to a receiver via one or more bounces off curved reflective surfaces) **or** refractive (i.e. the light is bent towards a receiver via one or more transmitting, refractive elements) technologies. Dividing further, reflective and refractive technologies can focus towards a line/tube or towards a central spot/absorber. Although hybrids of these divisions are also possible, these classifications are a good start. Figure 4 shows this breakdown with some examples.

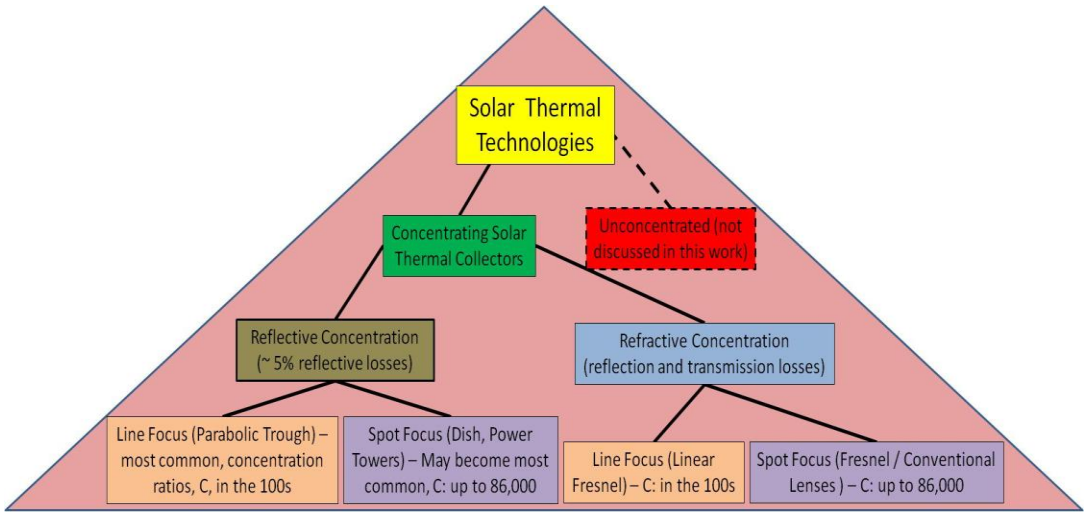

Figure 4. Categorization of solar thermal technologies - C is the solar concentration ratio

The next important distinction that can be made in classifying solar thermal technologies is by the working fluid of the system. The choice of working fluid determines the thermodynamic characteristics of the system. If a liquid working fluid is used throughout (for ease of pumping), maximum temperatures and pressures are limited. For pure water, the critical point occurs at ~375^{o}C and at 22 MPa or 220 atmospheres (Cengel & Boles, 2010). With the exception of some supercritical systems, usually containing extremely high pressure is uneconomic. Thermal oils, like Therminol VP-1, can be used at higher temperatures - in the 200^{o}C - 400^{o}C range (Solutia, 2010). Another category of commonly used solar thermal liquids are molten salts. Molten salts can be operated at even higher temperatures, in the range of 400^{o}C - 500^{o}C (Kearney, 2004). Air and steam systems can be run at even higher temperatures, but higher pressures and pumping powers are usually required to obtain high energy density. Therefore, many systems use heat exchangers to transfer heat between working fluids. At present, no particular working fluid or combination of fluids has proven dominant, but pilot / demonstration -scale projects have been built using each of them (Thirugnanasambandam et al., 2010).

One emerging way of categorizing solar collectors is by those that can absorb light either on an outer solid surface or directly into the volume of the working fluid. Since most of the aforementioned working fluids are transparent to most of the solar spectrum, the absorption medium is *critical* to any thermal

collector. That is, regardless of the technology used, a well designed 'absorber' is the key component that makes thermal collection possible.

1.4 Motivation for Using Nanofluids

Liquids are often used as energy carriers since pumping is relatively easy. For this reason, a large amount of research is devoted to finding new types of fluids and new and novel ways to control fluids. One of these novel types of fluids - nanofluids (suspensions of nanoparticles in liquids) - has been studied extensively in the last 10-20 years. In these studies, researchers have seen evidence that nanofluids can enhance a wide range of liquid properties. Specifically, many researchers have found that a small amount (<1% by volume) of nanoparticles can significantly change the thermal properties of fluids. The following chapter will discuss the thermal properties of nanofluids in detail. For now, we can summarize by saying that, on the whole, thermal properties ***can*** be enhanced from the bulk fluid by adding nanoparticles. However, recent studies indicate that nanofluids must be very carefully chosen to match their application in order to see ***useful*** enhancement. If the type or volume fraction of nanoparticles is wrong - or if breakdown occurs - a nanofluid may actually harm system performance. Thus, the goal of this research is to explore some of these possibilities, with an emphasis on creating a volumetric absorber for high-density light energy. If feasible, this technology would have several applications in solar thermal energy utilization. Consequently, we intend to address some of the

challenges of harvesting solar thermal energy by testing the photothermal energy conversion potential of nanofluids.

Currently, solar thermal collectors capture light energy on an absorbing surface, which must then transfer that energy via convection to a circulating fluid. A simple thermal resistance network, as outlined in Figure 5, demonstrates how this thermal path can conceivably be shortened with a nanofluid. That is, with a volumetric absorber it is possible to save some of the useful energy normally expended due to the finite temperature difference between the absorber plate and the collector fluid. If the system requires phase change, it may be possible to realize even more energy savings by boiling the working fluid directly with radiative energy, rather than going through an intermediary heat transfer liquid. For instance, a solar-driven absorption or Rankine cycle could be significantly improved if concentrated solar energy could be routed directly to the working fluid inside the generator or boiler.

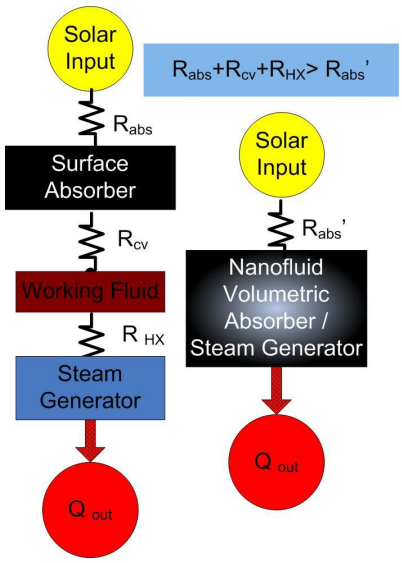

Figure 5. Thermal resistance network - comparison between a conventional solar thermal plant and a nanofluid solar thermal plant. R_{abs}, R_{cv}, R_{HX}, and $R_{abs'}$ refer to thermal resistances present during the solar solid surface absorption, conduction/convection from a solid surface, and solar direct absorption/steam generation heat transfer steps, respectively.

1.5 Research Objectives

The goal of this research is to determine how nanofluids transfer heat, absorb light, and change phase (e.g. boil) volumetrically and/or locally. The major outcome of this research is to determine if these fluids are applicable to solar thermal energy harvesting. To make these determinations, the following research questions need to be answered:

1. To what extent can nanofluids enhance heat transfer in convection, conduction, radiation modes? That is, what are the expected heat transfer

properties of nanofluids (viscosity, specific heat capacity, thermal conductivity, absorbtivity, emissivity, etc.)

2. How does adding nanoparticles to conventional base fluids affect radiative properties? That is, what are the measured and/or predicted extinction coefficients of various nanofluid mixtures as a function of wavelength.
3. How do nanofluids compare to their base fluids in boiling heat transfer?
4. What is the potential for using nanofluids as the medium for solar collection?

Each of the above questions is essentially answered as a complete chapter in this manuscript. To demonstrate the 'state-of-the-art' in the field of nanofluid heat transfer, the next chapter will present a nanofluid literature review. This will include methods for preparing nanofluids and describe how other researchers have quantified and measured various nanofluid properties. In spite of all the research mentioned in the next chapter, nanofluids are still a long way from being well understood. As a result, chapter 3 presents the modeling techniques used in this research to attempt to predict nanofluid properties and performance. Along the same lines, chapter 4 presents the experiments that were done in this research to explore boiling in nanofluids. Chapter 5 uses the results of modeling and experimentation to predict how well nanofluid solar receivers will work in real-

world applications. Finally, chapters 6 and 7 will discuss the conclusions and possible future work that can be formed from these efforts.

CHAPTER 2: NANOFLUIDS AS HEAT TRANSFER FLUIDS

Nanofluids, which are likely the simplest nanotechnology in the emerging 'nano-tech' field, are composed of a mixture of nanoparticles with a conventional base fluid. The extremely small size of the particles (1/1000th the diameter of a human hair), ideally, allows them to pass through pumps and plumbing without adverse effects. Since there are a multitude of nanoparticle materials and geometries to choose from, nanofluids can be tuned to achieve various design goals. That is, by adding nanoparticles one can control the properties of commonly used base fluids. Properties such as thermal conductivity, specific heat, viscosity, the convective heat transfer coefficient, electrical conductivity, the Seebeck coefficient, emissivity, optical absorption, and optical scattering coefficients - to name a few - can all be all changed with the addition of nanoparticles. Although there are many other possible outlets for nanofluids, this research will focus on the applicability of nanofluids as direct solar absorbers. This chapter will scrutinize the basic properties of nanofluids through that lens. That is, this chapter will characterize selected nanofluid properties which can potentially affect the performance of a solar thermal collector.

For this approach we define the properties needed in an ideal 'solar nanofluid' - a nanofluid which works well in solar thermal collectors. If possible, our goal is to create and use nanofluids which allow the collector to do the

following: 1) efficiently absorb solar radiation (in the wavelength range - $0.25 < \lambda < 2.5$ μm), and convert it to heat directly inside the working fluid, 2) minimize heat losses by convection and radiation (in the wavelength range - $\lambda > 4$ μm), and 3) keep system fouling/clogging and pumping costs to a minimum.

2.1. Stable Nanofluid Preparation

A prerequisite in creating good 'solar nanofluids' is that they must be stable. Further, a stable nanofluid is required even to obtain accurately measured thermal and optical properties. Without careful preparation, nanoparticles will agglomerate and settle out of the base fluid in a very short time. Therefore, this section will briefly discuss methods of producing stable nanofluids.

Although there are many methods of nanofluid preparation, they can be roughly categorized into one-step and two-step processes. One-step processes synthesize the nanofluid to the desired volume fraction and particle size inside the base fluid. Thus, the final product is a specific nanofluid which is ready for use (possibly after dilution). The two-step method is accomplished by first synthesizing the dry nanoparticles to a preferred size and shape. In the second step, these particles are carefully mixed into the desired base fluid at the desired volume fraction, usually with some additives for stability. Several researchers have had success fabricating and testing nanofluids using the one-step preparation methods (Kumar, S.A., Meenakshi, K, Narashimahan, B.R.V., Srikanth, S.,

Arthanareeswaran, 2009) and (Zhu, Lin, & Yin, 2004). Based on these results, one-step methods may produce the best results if they can be scaled up and manufactured inexpensively. However, due to its straightforward nature and its controllability, we will only use and discuss the two-step method.

A variety of dry powders are available 'off-the-shelf' from companies such as (NanoAmor, 2010) and (Sigma-Aldrich, 2010). These particles can be mixed into many different liquids at the preferred concentration. Depending on the stability and quality required, this process can take anywhere from a few minutes to several hours. For the test fluids of this article, the particles and up to 1% sodium dodecyl sulfate (aka SDS, a surfactant) were dispersed into the base fluid using a sonicator (a UP200 from Hielsher) for 15-30 minutes. From our experience, probe-type sonicators break particle agglomerates faster and much more thoroughly than bath-type machines. Since it is relatively quick, requires very little 'high tech' equipment, and produces any number of nanofluids, this process is our method of choice.

For stability on the order of days, surfactant (such as sodium dodecyl sulfate - also known as SDS) and/or additives to control the pH are cheap and easy options. To incorporate additives, one should sonicate all of the following at once: the preferred quantity of nano-powder, surfactant and/or some pH buffer, and the base fluid. Since it requires very little 'high tech' equipment and produces any number of nanofluids with good results, this process is our method of choice.

On the other hand surfactant-stabilized nanofluids eventually break down at elevated temperature and/or after several days to several months (Hong, H.-S. Yang, & C. J. Choi, 2005). For longer-term stability in a variety of conditions, one can re-sonicate frequently *or* attempt more exotic preparation methods, such as those given in (X. Yang & Z.-H. Liu, 2010) and (X. Yang & Z.-H. Liu, 2010). The idea behind any stabilization method is to create strong particle-particle repulsive forces and good wettablility with the base fluid to prevent agglomeration and settling. The extent of the resulting stability can be quantified by measuring the zeta potential. A simple way to calculate zeta potential is by using the Helmholtz–Smoluchowski equation (Cosgrove, 2010):

$$\zeta = \frac{U}{\varphi\varepsilon} \qquad (1)$$

where U, φ, and ε are the electrophoretic mobility, fluidity (i.e. the inverse of viscosity), and the liquid dielectric constant. Thus, zeta potential can be interpreted as the ratio of electrophoretic mobility (the relative motion of the particles under an electric field) to fluidity (the relative motion of the fluid under stress) - normalized by the fluid's dielectric constant. For a stable nanofluid, one would like to achieve a fluid which is as far as possible away from the isoelectric point which is usually found at moderate pH levels. The isoelectric point is defined as the pH where the particles carry no net electric charge. At this point particles will have repel each other with surface charge and may easily agglomerate. Very high or very low pH fluids are usually far away from the

isoeletric point and thus may also have large absolute values of zeta potential - i.e. > 30 mV. Since a surfactant like SDS creates a negative zeta potential and increasing the pH does the same, one can choose to do either or both to create a stable nanofluid. For surfactant, up to 1% by volume of SDS has been used often in the literature, although we have had good results with less. For metals and graphite, achieving a pH in the range of 9.5-10 is recommended (Cosgrove, 2010). Recently, we have combined both these methods for stable results.

2.2 Viscosity of Nanofluids

One of the most promising factors of nano-sized particles is that, as opposed to larger-sized particles, they can be put into conventional liquid pumping and plumbing with little adverse affects (i.e. without abrasion or clogging) (R. Prasher, Song, J. Wang, & P. Phelan, 2006) and (Sarit Kumar Das, Stephen U S Choi, & Patel, 2006). Also, ideal nanoparticle volume fractions end up being < 0.001 %v for sizable solar collector fluid depths. This leads to the possibility of achieving the aforementioned goal (3) with a solar nanofluid. That is, any improvements in other heat transfer properties cannot be offset by added pumping costs or particle clogging.

Some of the very first investigations into colloidal suspensions were done by Einstein (Einstein, A., 1906). Einstein considered a very simple case of uncharged, rigid, spherical particles homogenously distributed in a liquid. He

also used a dilute suspension (read: particle-particle interactions are negligible) and he assumed the particles to be unbounded (read: no forces acting on them) and viewed the surrounding fluid as a continuum (read: infinite compared to particle movement). With these assumptions he found that the effective viscosity can be approximated by the following equation:

$$\frac{\mu_{eff}}{\mu_f} = 1 + 2.5 f_v \quad (2)$$

where μ_{eff}, μ_f, and f_v refer to the effective nanofluid viscosity, the base fluid viscosity, and the particle volume fraction, respectively. Unfortunately, this model underestimates nanofluid viscosity as noted by (Cosgrove, 2010) and (Pak & Cho, 1998). To illustrate this, Pak and Cho used relatively high volume fractions (up to 10%) of alumina and titania nanofluids which showed pseudo-plastic viscosity - showing substantial deviation from the Einstein model.

To improve on this underestimate - without adding extra complexity - Prasher et. al. proposed the following equation for effective viscosity in a nanofluid (R. Prasher, Song, J. Wang, & P. Phelan, 2006):

$$\frac{\mu_{eff}}{\mu_f} = 1 + C_\mu f_v \quad (3)$$

where μ_{eff} and μ_f refer to the effective nanofluid viscosity and the base fluid viscosity, respectively. Also, C_μ can be found through a relation to several other

fluid parameters - see (R. Prasher, Song, J. Wang, & P. Phelan, 2006). For many cases, though, $C_u = 10$ is a reasonable approximation (R. Prasher, Song, J. Wang, & P. Phelan, 2006). It should be noted that since C_u is positive and f_v is positive, there must be an increase in viscosity with the addition of nanoparticles - $\mu_{eff} \geq \mu_f$.

It is relatively easy to argue, however, that the pumping power will not increase significantly if the particle volume fraction is very low. If we plug in $C_u = 10$ and $f_v < 1 \times 10^{-3}$, we can see that there is a negligible change in viscosity (i.e. $\mu_{eff} \sim \mu_f$). If viscosity is unchanged, it is even less likely that density would significantly change at these low volume fractions. For these reasons, low volume fraction nanofluids will only require negligible pumping power increases. Further, this also means that 'solar nanofluids' compare favorably with black dyes and micro/macro particle-laden liquids in terms of pumping power which may foul surfaces and require higher volume fractions (Zollinger, 2003). It should be noted that, all things being equal, smaller particles actually increase viscosity according to classical models, which many times take the form (Senapati, Mishra, & Parida, 2010):

$$\mu_{eff} = \frac{C_1}{D}\left(1 + \mu_f C_2 \frac{f_v}{C_3 - f_v}\right)^N \qquad (4)$$

where D is the particle diameter and C_1, C_2, C_3, and N are all constants which depend on the types of particles and the base fluid. We can see from this relation

that small particles actually increase the viscosity more so than larger particles. Fortunately at low volume fractions this phenomena is negligible as can be seen from inspection of equation 4 (noting that C_3 is always greater than f_v).

2.3 Nanofluid Heat Capacity

Researchers have also noted that the specific heat of a fluid can be changed by adding nanoparticles (Shin & Banerjee, 2011a; 2011b; S.-Q. Zhou & Ni, 2008). One relatively easy approach to modeling this change is through the following equation (S.-Q. Zhou & Ni, 2008):

$$c_{p,t} = \frac{f_p \rho_p c_{p,p} + f_f \rho_f c_{p,f}}{f_p \rho_p + f_f \rho_f} \quad (5)$$

where $c_{p,t}$ is the effective specific heat capacity of the mixture, $c_{p,f}$ the specific heat capacity of the fluid, $c_{p,p}$ the specific heat capacity of the particles, f_p the volume fraction of the particles, f_f the volume fraction of the fluid, ρ_p the particle density, and ρ_f the fluid density.

Let us examine this equation. Assume a nanofluid is composed of copper nanoparticles (ρ_p ~ 8,000 kg/m^3, $c_{p,p}$ ~ 0.39 kJ kg^{-1} K^{-1}) in water (ρ_f ~ 1,000 kg/m^3, $c_{p,f}$ ~ 4.2 kJ kg^{-1} K^{-1}). For this situation, we expect a significant decrease in the specific heat of the mixture - depending on the volume fraction. As a matter of fact, by using this equation, one would be hard pressed to find a nanofluid with an effective specific heat higher than the base fluid. This is because almost all liquids (organic and inorganic - except liquid metals) have a

rather high specific heat, greater than 1.5 kJ kg^{-1} K^{-1}. Thus, the specific heat of the base fluid is lowered when solid particles - most of which have specific heats lower than 0.8 kJ kg^{-1} K^{-1} - are added.

The work of (Shin & Banerjee, 2011a), (Shin & Banerjee, 2011b), however, shows that it is experimentally possible to create a nanofluid with a higher effective specific heat than a molten salt base fluid - up to a 24% increase. Their research essentially says that eqn. (3) is a decent first-order averaging scheme approximation, but other contributing factors can cause deviations from this simple approach. This is not a difficult point to make - for instance, local deviations are possible if the nanoparticles agglomerate or are not evenly spaced inside the fluid. On a global scale, however, this is harder to argue. Shin and Banerjee have proposed that a thin 'adhesion layer' or a 'percolation network' forms around nanoparticles due to high surface energy. This phenomenon, if present, can be thought of as creating an artificial ice layer around the nanoparticles. According to this theory, the latent heat of fusion of the base fluid can add to the effective specific heat capacity. If possible, this would be extremely important in a solar thermal system. A 25% increase in the specific heat of the molten salt heat transfer fluid in a solar thermal system essentially means that 25% less working fluid is needed. It also means that the required storage tanks are smaller for the same amount of storage capacity. In a commercial power plant this can mean millions of dollars in savings.

2.4 Conductive Heat Transfer

Thermal conductivity is the intrinsic property of nanofluids that has motivated the most research articles - for more on this work see (Keblinski, R. Prasher, & Eapen, 2008; Kleinstreuer & Feng, 2011; Trisaksri & Wongwises, 2007). This seems to be mostly due to the fact that some early experimental works demonstrated anomalous increases in thermal conductivity. That is, the first few experimental works indicated that the effective thermal conductivity of common base fluids (chiefly water) can be increased by up to 30% with volume fractions of <5%.(Hong, H.-S. Yang, & C. J. Choi, 2005; Kleinstreuer & Feng, 2011; S. Lee, S. U.-S. Choi, S. Li, & Eastman, 1999; Volz, 2010)

Many explanations have been posited as to the fundamental source of these enhancements. Thermal conductivity could theoretically be increased due to higher surface roughness, random particle mixing (Brownian motions), particle-particle interactions in the suspension, high surface areas for heat transfer, and percolation networks which offer high heat transfer paths - just to name a few of the explanations that have been presented in literature. Much of the early work used a traditional 'hot-wire' method for measuring thermal conductivity. In this method a wire is heated and the fluid temperature is measured on the wire and usually at various distances away. By knowing the wire geometry, heat input,

temperatures, time, and distances the following equation can be used to find the thermal conductivity (Carslaw & Jaeger, 1986):

$$T(t) - T_{ref} = \frac{q_{wire}}{4\pi k} \ln\left(\frac{4\alpha}{a^2 C} t\right) \quad (6)$$

where $T(t)$ and T_{ref} are the temperature of the wire at time t=t and t=0, respectively. The parameters q, k, and α are the applied electric power, the thermal conductivity, and the thermal diffusivity of the fluid, respectively. Lastly, a and C represent the radius of the wire and Euler's constant.

In practice, unfortunately, this approach has significant errors at both long (read: steady state) and short (read: transient) measurement times. Thus, some research groups have criticized the results of early work, which used this method and presented large, anomalous thermal conductivity measurements. To get around these errors, some researchers have used optical thermal conductivity measurements. Note: Most optical methods use the fact that the refractive index of the base fluid changes with temperature to obtain temperature gradients in the fluid. Using these methods researchers did not measure nearly as large of improvements in thermal conductivity. In fact, the work of (Putnam, Cahill, Braun, Ge, & Shimmin, 2006), (Rusconi, Rodari, & Piazza, 2006), and (Venerus, Kabadi, Sunmook Lee, & Perez-luna, 2006) indicate that for various nanofluids classical effective medium theories pretty accurately predict the effective thermal conductivity. Thus, with 'well-prepared' (i.e., well distributed) nanofluids one can

expect the effective thermal conductivity to obey the following Hamilton-Crosser model (Venerus et al., 2006):

$$\frac{k_{eff}}{k_f} = \frac{2 + k_p / k_f + 2(k_p / k_f - 1) f_v}{2 + k_p / k_f - 2(k_p / k_f - 1) f_v} \quad (7)$$

where k_{eff}, k_f, and k_p are the thermal conductivities of the suspension, base fluid, and particle, respectively, and f_v is the particle volume fraction.

A consensus seems to be emerging among researchers that while thermal conductivity can be enhanced, it is nothing anomalous. Thus, this research will assume that the Hamilton-Crosser model is a good predictor of nanofluid effective thermal conductivity.

2.5 Convective Heat Transfer

There has also been a lot of recent research into convective heat transfer (Eapen et al., 2007; Lai, 2010; J. Lee, Gharagozloo, Kolade, Eaton, & Goodson, 2010; Putra, Roetzel, & Sarit K. Das, 2003; Zeinaliheris, Etemad, & Nasresfahany, 2006). This is logical because if heat transfer fluids are ever going to be used in heat transfer applications they will undoubtedly be in flowing systems. To truly push the boundaries of heat transfer much of this research is done in micro-channels and in some cases even overlaps with the next section - boiling heat transfer.

When determining a fluid's ability to transfer heat in the form of convection, most researchers either quote the heat transfer coefficient, *h*, or the Nusselt number, Nu, which is the ratio of convective to conductive heat transfer across a normal boundary and is defined as the following:

$$Nu = \frac{hL}{k} \quad (8)$$

where *h* is the heat transfer coefficient, *L* a characteristic length (usually in the direction of boundary layer growth) and *k* the fluid thermal conductivity. In light of the last section, it is important to make sure that the effective thermal conductivity of the nanofluid is known in order to get a good determination of the heat transfer coefficient from the Nusselt number or vice versa.

In the field of nanofluid convective heat transfer research there is a similar debate over the magnitude (if any) of enhancement. There is also disagreement about the source of enhancement as several ideas have been proposed to explain how nanoparticles interact in the fluid. The idea is that energy exchange is improved because particles move randomly via Brownian motion and pull / mix fluid with them. Some researchers - (Duangthongsuk & Wongwises, 2009) for example, have noted that in turbulent flow nanofluid convection increases with Reynolds number and with volume fraction. Others, like (Pak & Cho, 1998), found that for water-based γ-Al_2O_3 and titania (TiO_2) nanofluids, convective heat transfer is actually decreased by up to 12% due to increased viscosity. Others,

like (W. Williams, Jacopo Buongiorno, & L.-W. Hu, 2008), have shown no change from the base fluid for a large range of flow rates (9,000<Re<63,000) in zirconia ZrO_2) nanofluids. Overall, it seems that here again classical models are the best approximation of the enhancement. In selecting nanofluids for convective heat transfer, one must also be very careful not to increase the viscosity as this can cause decreased overall performance.

2.6 Boiling Heat Transfer

As mentioned above, there has been considerable disagreement over the value of using nanofluids in heat transfer applications. This trend continues into the field of nanofluid boiling. Since a major focus of this work is boiling and phase change, this section will give considerable detail of the state-of-the-art in nanofluid boiling.

Interestingly, at the time of writing this manuscript, there is a nearly even three-way split in experimental results for conventional systems where boiling occurs at a heated surface. Seven studies have shown enhancement (Z. Liu, Xiong, & Bao, 2007), (M.H., Shuai, Chen, Q. Li, & Xuan, 2007), (Tu, Dinh, & Theofanous, 2004), (Dongsheng Wen & Ding, 2005), (D Wen, 2008), (Dongsheng Wen, Ding, & R. A. Williams, 2006), (Witharana, 2003), several have shown degradation (I. C. Bang & S. H. Chang, 2005), (Sarit K Das, Putra, & Roetzel, 2003), (Jackson, 2007), (Kim, S.J., Bang, I.C., Buongiorno, J., Hu,

2007), (Milanova & R. Kumar, 2005), (D. Zhou, 2004), (Truong, 2007), and several saw little or both enhancement and degradation (Chopkar, et al., 2007), (Narayan, Anoop, & Sarit K. Das, 2007), (Vassallo, 2004), (S. M. You, J. H. Kim, & K. H. Kim, 2003). Table 1 summarizes the literature results. Note: Unless otherwise stated, the words 'enhancement' and 'degradation' mean relative to pure water - the conventional base fluid.

Table 1. Review of experiments with nanofluid boiling.

Researcher(s)	Heater Type	Nanofluid	Results	Particle Deposition
Liu et al.	Grooved Cu Block	Cu0 / H_20	Enhancement, 25-50%	Yes, A Bonded Coating
Shi et al.	Cu block, D=60 mm	Al_20_3, Fe / H_20	Enhancement, up to ~60%	Yes
Tu et al.	Vapor Deposited Ti Heater, 26 x 40 mm	Al_20_3 / H_20	Enhancement, up to ~64%, 1 data set	Yes
Wen et al.	Stainless Steel Disc, D=150mm	γ-Al_20_3 / H_20	Enhancement, up to ~40%	No
Wen et al.	Stainless Steel Disc, D=150mm	$Ti0_2$ / H_20	Enhancement, up to ~50%	No
Witharana S.	Cu Block D = 100mm	Au , $Si0_2$/ H_20, EG	Enhancement, up to ~15-20%	Not Studied
Truong, B.	Stainless Steel Wire	Al_20_3, $Si0_2$ / H_20	Enhancement up to 68%	Yes, Measured
Ahn et al.	Nano-Structured Cu Block	*MWCNTs / PF-560**	Enhancement 19-33%	Yes, By Design
Coursey and Kim	Oxidized/Metalized Cu block	Al_20_3, / H_20 or Ethanol	Enhancement 0-50%	Yes, Extensive Surface Testing
Bang and Chang	Rectangular, 4mm x 100mm	Al_20_3 / H_20	Deterioration ~20%	Yes
Das et al. (pioneer)	Smooth/Rough, Cartridge Heaters	Al_20_3 / H_20	Deterioration, 10-40%	Yes
Jackson and Bryan	Cu Block	Au / H_20	Deterioration, 10-25%	Yes
Kim et al.	Stainless Steel Wire, D=0.38mm	Al_20_3, $Zr0_2$, $Si0_2$ / H_20	Deterioration	Yes
Milanova et al.	NiCr Wire, D=0.32mm	Al_20_3, $Si0_2$, $Ce0_2$ / H_20	Deterioration	Yes
Zhou, D.W.	Horizontal Cu Tube	Subcooled Cu/Acetone	Deterioration	Not Studied
Sajith, V.	NiCr Wire, D=0.19mm	Al_20_3 , Cu/ H_20	Deterioration	Yes
Trisaksri, Wongwises	Cylindrical Cu Cartridge	$Ti0_2$, Cu/ HCFC 141b	Deterioration	Not Studied
Chopkar et al.	Cu block, D= 60.5mm	$Zr0_2$ / water	Little change	Yes, Smoothened
Kim et al.	Cu, Var. Orient., T_{sat} = 60°C	Al_20_3 / H_20	Little change	Yes

Narayan et al.	Vertical Tube Heater, Var. Roughness	Al_20_3 / H_20	-45% < Dep. on 'surface interaction parameter' < 70%	Yes
Vassallo et al.	NiCr Wire, D=0.4mm	$Si0_2$/ H_20	Little change	Yes, Thin Coating
You et al.	Cu, T_{sat} = 60°C	Al_20_3 / H_20	Little change	Not Studied

* The fluid did not contain nanoparticles, but is mixed with the nano-structured surface

The papers showing enhancement give an average enhancement ranging from 30-60% higher heat transfer during nucleate boiling. (D.-W. Liu & C.-Y. Yang, 2007) used copper oxide (CuO) particles in an attempt to increase the effectiveness of the evaporator of a miniature flat heat pipe. These authors tested nanofluids on smooth micro-grooved surfaces at different pressures. They found significant enhancements (especially at low pressures) until the mass concentration exceeded 1% - after which enhancement decreased. Also, in this same study, a thin layer of 'porous' nanoparticles was found to be deposited on the heater surface after testing. Shi et al. conducted experiments with iron (Fe) and alumina (Al_2O_3) nanoparticles boiled on a Cu block. The authors concluded that Fe particles showed more enhancement than Al_2O_3 particles and that enhancement was mostly due to increases in thermal conductivity and lowered surface tension. It should also be noted that the authors saw some particle deposition. Tu et al. tested Al_2O_3 nanofluids on a 'nanoscopically smooth' vapor-deposited heating surface. Limited data were taken in this study, but they showed enhancement in heat transfer and a four-fold increase in nucleation sites – indicating at least some nanoparticles deposited on the surface. Wen and Ding used gamma phase Al_2O_3 nanofluid boiled on a stainless steel disc of micron-

sized surface roughness. The authors found no particle deposition during their experiments. Wen and Ding , in another study with a similar set-up except with titania (TiO_2) nanoparticles, showed an even larger enhancement (~50%) in boiling heat transfer. The authors, again, did not see much particle deposition. Truong found very high enhancements (up to 68%) in heat transfer during pool boiling experiments with silica (SiO_2) and Al_2O_3 water based nanofluids. Truong did a considerable amount of work to determine the amount and rate of particle deposition, indicating that it had a major influence on the enhancement. Aha et al. boiled refrigerants on nano-structured surfaces in an effort to test critical heat flux enhancement. They saw 19-33% enhancement in nucleate boiling. The surfaces were formed by chemical vapor deposition of multi-walled carbon nanotubes. This can be considered an extended case of nanoparticle deposition – the authors called it 'nano-fin enhancement' - Aha et al.. Coursey and Kim found that Al_2O_3/H_2O nanofluids were unchanged in the nucleate regime, but Al_2O_3/Ethanol showed a significant improvement of 5-50% (depending on concentration) when boiled on a polished copper heater. The contact angle of the heater surface was significantly reduced after boiling in nanofluids.

In summary, these studies of dilute nanofluids showed enhancement ranging from 15-68% in nucleate boiling heat transfer. The studies used a wide

variety of materials and geometries for nanoparticles and heaters. Most of them noticed a deposition of nanoparticles on the heater surface after boiling.

The literature which concluded nanofluids were detrimental to pool-boiling heat transfer performance showed a decrease in heat transfer ranging from 10-40%. Bang and Chang studied Al_2O_3 nanofluids on a surface with a roughness of a 'few tens of nanometers' which was controlled by sandpaper. Relatively high concentrations, up to 4% by volume, showed ~ 40% less heat transfer. The authors noted that the nanofluids significantly changed the surface roughness especially after the heated surface was taken to critical heat flux. Das et al., the pioneers in this area, boiled Al_2O_3 nanofluids on a standard and a roughened cartridge heater, R_a = 0.4-1.6μm, respectively. In all tests the nanoparticles hindered heat transfer. Das et al. concluded that particles fouled the heated surface and caused deterioration. Jackson tested Au nanofluids on a Cu block at various pressures. Overall, Jackson found that heat transfer was reduced and the surface roughness was increased by the nanofluids. Kim et al. tested several nanofluids (Al_2O_3, ZrO_2, SiO_2) on stainless steel wires and plates. The authors saw degradation, but since the electrical resistivity-temperature curve for stainless steel was not well known, it was mostly a qualitative result. The authors *did* find that a significant amount of particles was deposited on the heated surface (increasing surface roughness) and that the contact angle was reduced from ~80^o to 8-36^o, depending on conditions. Milanova et al. also tested

several types of nanofluids: Al_2O_3, SiO_2, and ceria (CeO_2). The authors looked at the effect of changing the pH in pool boiling experiments. The authors observed, in most cases, a decrease in nucleate boiling heat transfer. They also noted that their nichrome (NiCr) wires were oxidized and that there was significant particle deposition during the boiling experiments. Zhou conducted boiling experiments using Cu nanoparticles with acetone as the base fluid. A horizontal Cu tube was utilized as the heating surface and the effects of sub-cooling and acoustic cavitations were investigated. Zhou concluded that there was some enhancement for natural convection, but that the heat transfer during boiling was degraded. The author did not comment on particle deposition. Sajith et al. used the hot wire method with Al_2O_3 and Cu / H_2O nanofluids. The authors attributed deteriorated boiling heat transfer to nanoparticle deposition. Trisaksri and Wongwises showed deterioration under various pressures for TiO_2-R141b nanofluids on copper cartridge heaters. No information was presented about particle deposition.

For this group of papers, deterioration of 0-40% was seen – although many authors did not quantify the change as a percentage. Again, a wide variety of heater and particle materials was used. In most cases, particles were noticed to foul the heater surface due to boiling.

As mentioned above there were a few papers which could not be clearly placed in either the ‘showed enhancement’ or ‘showed degradation’ categories.

These were papers that had both increased and decreased heat transfer during their tests or those that indicated little to no change. Chopkar et al. conducted tests with zirconia (ZrO_2) based nanofluids on a Cu block. At low particle loading heat transfer was enhanced, but at higher concentrations or with repeated runs a decrease in heat transfer was seen. The authors noted that their heated surface became *smoother* after nanofluid boiling, as opposed to most studies that reported nanoparticle deposition on the heated surface. Tests were also carried out with the addition of surfactants. The authors concluded that, overall, it was too early to say whether heat transfer was enhanced or degraded. Kim et al. conducted experiments with Al_2O_3 nanoparticles at low pressure. Their study investigated the effect of different heater orientations mostly with respect to critical heat flux. In this study bubble size was seen to increase while bubble frequency decreased. In spite of these changes, the authors concluded that nucleate boiling heat transfer was unchanged for nanofluids. Narayan et al. tested Al_2O_3 nanofluids on a vertical tube with a variety of surface finishes. The roughness of the heaters used ranged from 48-524nm. The authors defined a 'surface interaction parameter' which was simply the surface roughness (R_a) divided by the average particle diameter. The authors stated that when the parameter is near or less than unity, boiling heat transfer is deteriorated. When the parameter is greater than one, roughness is much larger than particle size and heat transfer is enhanced. The authors concluded that nucleation sites can be

basically blocked if particles are roughly the same size as the nucleation sites – causing deterioration. Otherwise systems can be engineered for enhancement in boiling heat transfer. Vassallo et al. did experiments with SiO_2 nanofluids on NiCr wires. The wires in this study showed a thin coating after boiling. Overall, the data fell on both sides of the curve for pure water, so no conclusions about enhancement or deterioration could be drawn. You et al. conducted experiments with Al_2O_3 nanoparticles at low pressure. This study focused mostly on critical heat flux. Bubble departure was decreased but bubble size was increased giving little net change in the nucleate boiling regime.

This group of literature shows a wide range of results for diverse surface-particle material combinations. Most interestingly, Narayan et al. suggests that enhancement or deterioration can be controlled by surface conditions. All but one of these studies noticed particle deposition as a result of nanofluid boiling.

The classic correlation developed by Rohsenow is widely believed to accurately capture pool boiling phenomena for most conditions. It has been noted, however, by some in the above literature that deviation from the correlation occurs when nanoparticles are added. The correlation can be represented in the following form Carey:

$$q'' = \mu_f h_{fg} \left[\frac{\sigma}{g \cdot \Delta\rho} \right]^{-\frac{1}{2}} \cdot \left(\frac{1}{C_{sf}} \right)^{\frac{1}{r}} \cdot \mathrm{Pr}^{-\frac{s}{r}} \cdot \left[\frac{c_{pl}(T_w - T_{sat})}{h_{fg}} \right]^{\frac{1}{r}} \quad (9)$$

where q'' is heat flux, μ_f, h_{fg} the fluid viscosity and the latent heat of vaporization, σ, g, $\Delta\rho$ the surface tension, acceleration of gravity, and change in density, C_{sf} a surface constant, Pr the Prandtl number and s, r are constants, and c_{pl}, T_w, and T_{sat} the liquid specific heat and temperatures at the wall and at saturation.

The constants in eq. (8) can change for different fluid / surface combinations. For example, pure water on a relatively smooth surface (polished with $^4/_0$ emery paper) matches the following constants: s = 1.7, r = 0.33, and C_{sf} = 0.0142 (Vachon et al.). Vachon et al. examined a large amount of data and concluded that the best fits for different conditions vary significantly. For instance, holding the other factors constant, C_{sf} can change from 0.0065 to 0.0215 for water on a ground or milled surface, respectively (Vashon). Of course a better fit can be obtained by changing the other factors, but for simplicity's sake we will compare data from the literature to the Rohsenow correlation for water only with s = 1.7, r = 0.33, σ= 0.06 N/m, and C_{sf} in the range 0.0065 – 0.05. This may seem like a small range for C_{sf}, but inspection reveals that it is essentially raised to the 3rd power. Therefore, the change from 0.0065 to 0.018 actually multiplies the equation by a factor of ~ 22. That said, Figure 6 shows various existing water-based nanofluid boiling data is easily bounded by Rohsenow's correlation by adjustment of C_{sf}.

The literature data in Figure 6 was collected by reading them off graphs from various articles. As such, the data shown here should be taken as a representation of the literature, not the exact results of the authors. This comparison reveals that since Rohsenow's correlation can bound the nanofluid boiling data, it can also be used as a reasonable fit. Thus, intermediate values of C_{sf} should allow the correlation to match well with most experiments. Since particles are expected to deposit on (and modify) the heated surface throughout boiling, C_{sf} must logically change during the process as well. The only literature data set that cannot be represented by Rohsenow's correlation is Kim et al. - whose data start at exceptionally high superheat values.

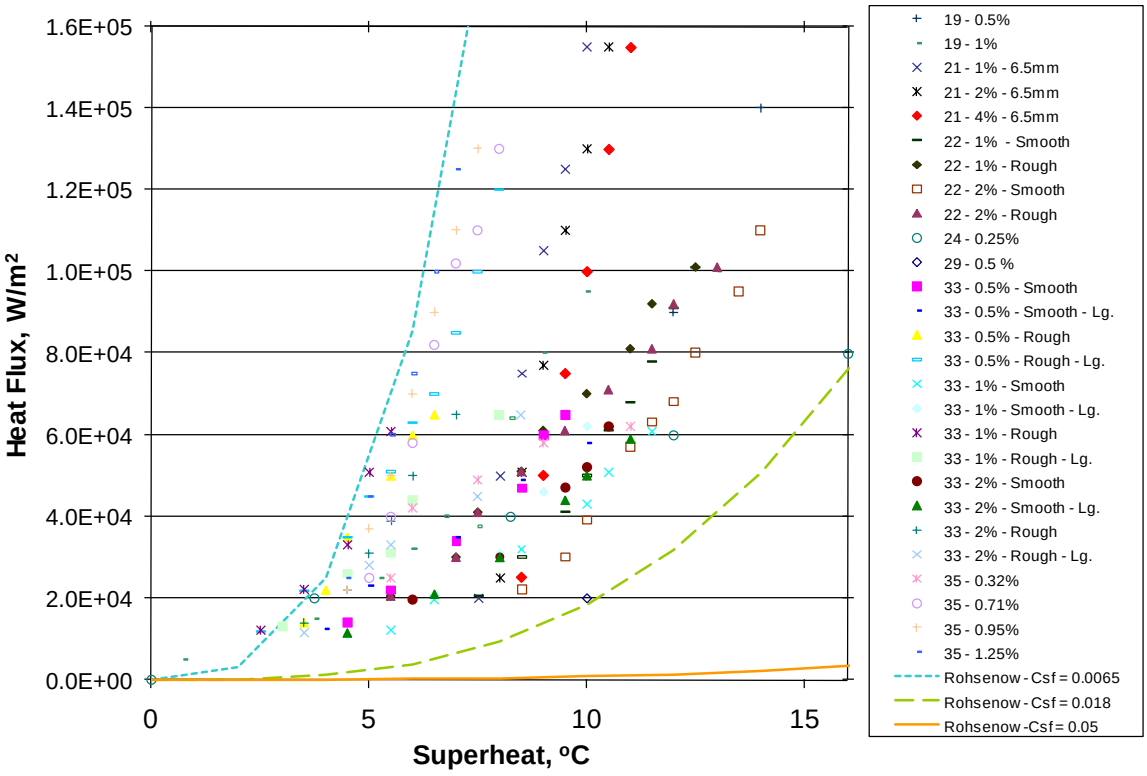

Figure 6. Selected pool boiling data for water-based nanofluids (for a variety of nanoparticle materials) as compared to Rohsenow's correlation (Rosenhow, 1952) **with different surface constants**

Many important phenomena are lumped into the parameter C_{sf}. For the solid heater surface, C_{sf} takes into account thermophysical properties such as thermal mass and conductivity. In general, though, the most complicated part of determining C_{sf} is that the solid, liquid, and vapor all interact at the surface. In the case of a nanofluid, complexity is added since there are also nanoparticles present at the surface. Micro- and nano- scale cracks, pores, and pits in the surface and even defects in the nanoparticles can affect this interaction (Singh, A., Mikic, B.B., Rohsenow, 1976). Surface roughness is certainly a good

indicator of the heater geometry (and of C_{sf}), but it is hard to discern which measurement – average, extreme, spacing, or some combination – and which measurement method is most indicative. Wettability and adhesion are also tied to geometry (Singh, A., Mikic, B.B., Rohsenow, 1976). Thus, there is no simple equation that can be written to describe C_{sf}. Even if C_{sf} could be empirically broken down and analyzed for each liquid-surface combination, it would lose simplicity and generality. Therefore, C_{sf} will have to be interpreted as a constant which accounts for all the complicated interactions that happen at the interface.

Overall, though, if C_{sf} can be determined (based on the particle choice and boiling surface), the Rohsenow correlation is a good predictor of boiling heat transfer for nanofluids. This indicates that enhancements, if seen, are mainly due to surface modification by nanoparticle deposition. Note: this will be discussed in more detail later.

2.7 Radiative Heat Transfer

Very recently, there has also been a reasonable amount of work on radiative heat transfer in nanofluids. Since this research is focused on solar energy harvesting, this section will be slanted towards absorption of radiative heat from sunlight. As the body of published research expands, it is becoming clear that in this arena, as with the other nanofluid phenomena, the nanofluid mix must

be very carefully chosen to match their application in order to see enhancement. This is especially true for the nanofluid optical properties in a solar collector.

The basic concept of using particles to collect solar energy was studied in the '70s with (Hunt, 1978) and (Andresen, et al., 1988) who mixed particles in a gas working fluid. In the last 10-12 years, gas-particle receivers have been extensively modeled and several prototype collectors have been built and tested. This research experimentally demonstrated the absorption of radiation volumetrically using particles and was done by the following: (C L Tien, 1988), (Steinfeld & Schubnell, 1993), (J. Karni, a A. Kribus, Rubin, & Doron, 1998), (Miller & Koenigsdorff, 2000), (Bertocchi, A. Kribus, & Jacob Karni, 2004). However, in these articles the particles were large - greater than or equal to 500 nm in diameter. Also, many of these researches used particles mixed with a gas - not a liquid as in these experiments.

There are a few papers, however, which model the performance of nanofluid solar collectors. These include a few older works on high flux gas-particle suspensions and some more recently published analytical studies - e.g. (Merabia, Keblinski, Joly, L. J. Lewis, & Barrat, 2009). In addition an increasing level of research into the production of hydrogen using zinc oxide has led researchers to pursue other high flux concentrators utilizing nanoparticle gas suspensions (Haussener et al., 2009; Schunk et al., 2008). (Hunt, 1978) and (Abdelrahman, 1979). A fluid layer (volumetric) collector developed by(Minardi

and Chuang, 1975; Caouris et al., 1978) looked at absorbing light inside the fluid volume instead of limiting it to the surface area (Arai et al., 1984). These works were devoted to finding reversible chemical reactions which show promise to provide hydrogen or some other chemical fuel.

Recent work by (Tyagi, 2008) and (Lenert, Zuniga, & E. N. Wang, 2010) numerically and experimentally evaluated the benefit of a direct absorption receiver using nanoparticle suspensions in water in conditions similar to a flat plate collector (low-irradiance). This increase in radiative absorption has been shown numerically to lead to an increase in collector efficiency (Tyagi et al., 2008). All of the previous experimental studies to date have focused on using micron sized particles for particle suspensions for direct absorption.

A lot of insight can be gained from these works, but none of them looked at high irradiance in a liquid nanofluid. Since direct steam generation might be a very economical way to employ nanofluid solar thermal harvesting. On this topic (aside from the work at Arizona State University), the only published article available was some recent molecular dynamics simulations that concluded that curvature-induce pressure around a nanoparticle can inhibit phase change in the base fluid (Merabia, Keblinski, Joly, L. J. Lewis, & Barrat, 2009). Further, these simulations indicated that the solid nanoparticle could actually melt before the surrounding fluid would change phase (Merabia, Keblinski, Joly, L. J. Lewis, & Barrat, 2009). Overall, it is clear that light-induced boiling in nanofluids is not

fully understood. This following chapters will present some simple experimentation and modeling towards developing this field of research.

One of the major advantages of going to a system that uses liquid-nanoparticle suspensions is the tunability of the size, shape, and volume fraction of the nanoparticles for the operating mode of the system. Small changes in these areas can drastically change scattering and absorption. For example, if the volume fraction of nanoparticles is very high, all the incoming light will be absorbed in a thin surface layer where the thermal energy is easily lost to the environment. On the other hand, if the volume fraction of nanoparticles is low, the nanofluid will not absorb all the incoming solar radiation. Therefore, the optical properties of the fluid must be chosen very precisely or a nanofluid could actually be detrimental in a solar collector.

It should be noted that the most important optical properties are both the absorption coefficient *and* the scattering coefficient. For most of this manuscript, scattering will be neglected because we will use very low concentration nanofluids. According to the work of (C L Tien, 1988), presented in Figure 7, nanofluids will experience dependent scattering if the volume fraction becomes larger than ~0.006 or 0.6%. The line in Figure 7 is described by the following equation:

$$\frac{c}{\lambda} = \frac{\alpha}{\pi}\left(\frac{0.905}{f_v^{1/3}} - 1\right) > 0.5 \qquad (10)$$

where c and λ are the inter-particle spacing in the fluid and the wavelength of incident light. The parameters f_v and α are the particle volume fraction and a 'particle size parameter' which is a non-dimensional quantity that relates the particle diameter to the wavelength of incident light - this parameter will be discussed in more detail in chapter 3.

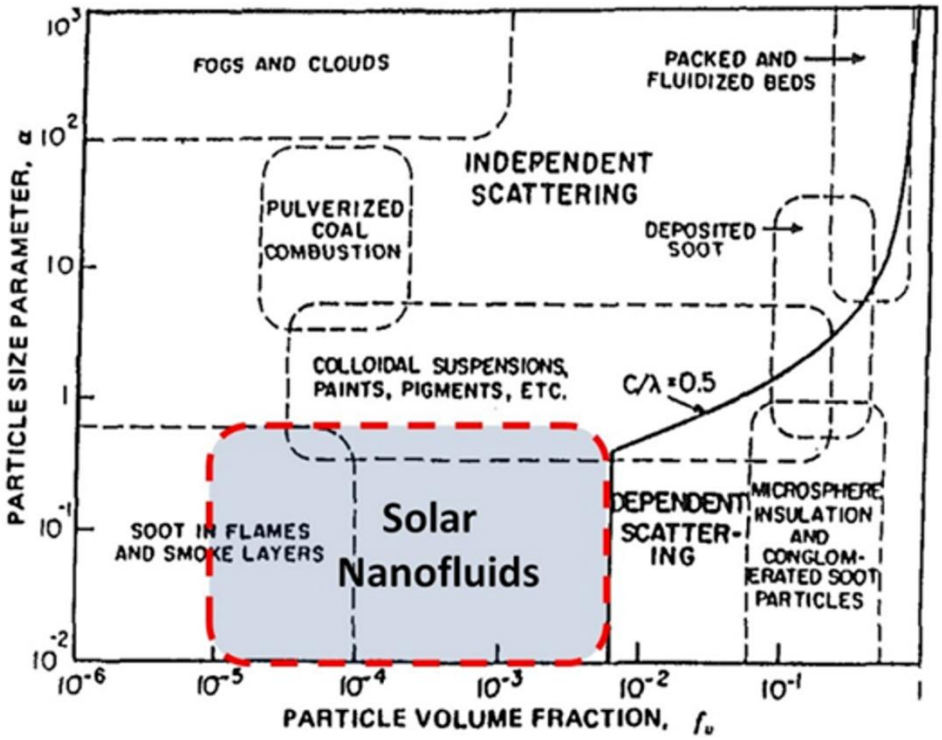

Figure 7. Scattering regime map showing the boundary between dependent and independent scattering (C L Tien, 1988)**.**

For most nanofluid solar collectors, volume fractions will certainly be below this threshold. However, this does not mean that scattering will not be

present, only that the scattering of one particle should not be affected by the scattering of other particles. That is, an incident photon should only encounter one scattering event on its way through the medium. This means the amount of scattered light should be directly proportional to the amount of particles in the fluid. Or looking at it another way, if the amount of particles is doubled, the amount of scattered light should double - if everything else stays the same.

If particles are nano-sized and far apart, the scattering component of the absorption coefficient will be small compared with the absorption component - but not zero. This manuscript will generally make this assumption, but it should be noted that this may not be correct. One major failing in the research is that properties and modeling results are often based on assuming the size of the particles to nominally be that quoted by the manufacturer. In general this is not true, since the particles always agglomerate to some extent with the two-step method of preparation. Dynamic light scattering results indicate the real average particle diameter to be ~100nm, instead of the manufacturer quoted 20-30nm. This can significantly change the amount of scattering that happens in a nanofluid. Equation 10 presents a simplified relationship for finding the fraction of incident light that is scattered (Bohren & Huffman, 1998).

$$\frac{I_s}{I_o} \approx \frac{\pi^4 N D^6}{8\lambda^4 r^2} \left| \frac{m^2 - 1}{m^2 + 2} \right|^2 \left(1 + \cos^2 \theta\right) \tag{11}$$

where D is the particle diameter, N the number of scatterers in the beam path, λ the wavelength of light, m the relative complex refractive index and θ the scattering angle. Thus, a tripling of the diameter (from 30nm to 90nm) gives a 730 fold increase in the amount of scattering! This becomes especially important at short wavelengths.

CHAPTER 3: NANOFLUID MODELING

The modeling focus of this research is on heat transfer and the properties that affect heat transfer. To do this empirical, analytical, and numerical approaches are all described in this chapter. Note: In most cases the simplest possible model which describes the phenomena of interest is employed.

To set the stage for more in-depth analysis and to decide what kind of modeling approach is most likely to yield useful results, this research uses an applications-driven approach. This can also be viewed as an experimental-driven approach, since the modeling effort is geared towards supporting the experiments described in the next chapter. Either way, the goal of this research is to predict performance of, and build/test, a high-irradiance photothermal conversion device. Therefore, to decide which types of modeling approaches are most important, we use a heat transfer modal analysis. A modal analysis - in this context - analyzes conduction, convection, phase change (if applicable), and radiation to see which mode(s) of heat transfer dominate. In order to do this, though, we must define the general application or experimental conditions that should be modeled. This can be done in a general way since we know high irradiance light is going to be incident on an absorbing volume of fluid. As light is absorbed, the fluid heats up and this heat is transferred to other parts of the fluid. Some of the heat is also lost

to the surrounding. This situation can be visualized as is shown in Figure 8 - i.e. the basis for this research.

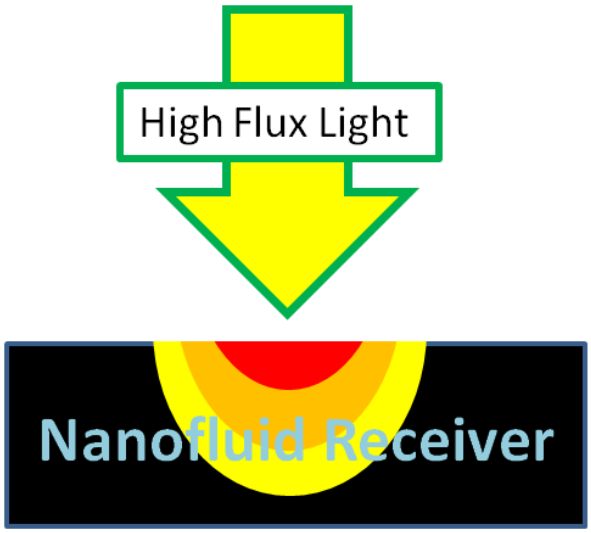

Figure 8. A general nanofluid photothermal energy conversion device

Figure 8 assumes that nearly all of the light that reaches the receiver is absorbed and turned into heat. Therefore, a temperature gradient with the surroundings is induced which can be dissipated by several modes of heat transfer. Initially, this temperature gradient will be quite large locally and ***conduction*** is expected to be important. Conduction analysis can also help to estimate the initial/maximum temperature rise in the heated region. As time progresses, buoyancy driven flow/heat transfer should develop around the heated region - for which ***natural convection*** flow should be a good approximation. We can also see that some energy is taken away in the form of the vapor bubble (i.e. ***phase change***) leaving at the end. Throughout the experiment ***radiation*** will also

transfer some of the heat out of the system. Lastly, the system reflects and transmits some of the light energy – which reduces heating. Each of these mechanisms of heat transfer will be discussed in the next few sections.

3.1 Conductive/Convective Heat Transfer

A simple bulk model can be developed by assuming the fluid is uniformally absorbing - or alternatively has an internal heat source. This can be done in two ways: either by assuming that the region is uniformly heated or by adding together the absorption of the particles in the region. Either way, in the simplest case, heat transfers in one dimension from the generating region into the surrounding fluid. A one-dimensional cylindrical region with heat generation is implied by the heat source being a cylindrical laser beam. As will be discussed in the experimental section, the solar collector can be approximated with a focused laser beam or a hot wire heating mode. These both provide essentially cylindrical heating conditions. A simple governing equation that appears to fit this situation can be expressed as:

$$\frac{\partial^2 T}{\partial r^2} + \frac{1}{r}\frac{\partial T}{\partial r} + \frac{e_{gen.}}{k} = \frac{1}{\alpha}\frac{\partial T}{\partial t} \quad for \quad 0 \le r \le R \tag{12}$$

where e_{gen} is the volumetric heat generation in a cylindrical region, R the radius of the cylinder, and k and α are the thermal conductivity and diffusivity, respectively. The initial and boundary conditions for this model are the following:

$$T\big|_{t=0} = 0 \tag{13}$$

$$\left.\frac{\partial T}{\partial r}\right|_{r=0} = 0 \tag{14}$$

$$-k\left.\frac{\partial T}{\partial r}\right|_{r=R} = hT\big|_{r=R} \tag{15}$$

The heat transfer coefficient, *h*, can vary significantly depending on the temperature gradient - which is driving convection. The solution to this problem can be found by using the integral-transform technique, similar to that presented in (Carslaw & Jaeger, 1986). Since the coordinate system is cylindrical, we get a Bessel series solution. The following series solution equation for temperature decreases with r, but increases with t:

$$T(r,t) = \frac{2e_{gen}}{kR}\sum_{m=1}^{5}\frac{J_1(\beta_m R)J_0(\beta_m r)}{\beta_m\left[\left(\frac{h}{k}\right)^2 + \beta_m^2\right]J_0^2(\beta_m R)}\left[1 - Exp\left(-\alpha\beta_m^2 t\right)\right] \tag{16}$$

The eigenvalues, β_m, of equation (15) can be found by solving for roots of the following transcendental Bessel function equation:

$$k\beta J_1(\beta R) - hJ_0(\beta R) = 0 \tag{17}$$

The steady state value of eq. (15) is found simply by setting the exponential term - the last set of brackets on the right-hand side - to 0. The constants used in the above equations are given in table 3.

Figure 9 gives the solution to this equation plotted as a function of time. It can be seen from the figure that as the heat transfer coefficient goes up, the system quickly reaches a lower steady state temperature rise – and vice-versa. Figure 9 shows that if the heat transfer coefficient is relatively small compared to the thermal conductivity, **very** high temperatures can be reached at the center of the heated region. Conversely, this result indicates that the heat transfer coefficient is likely to be quite large after a short time. This relationship between convection and conduction is best compared using the non-dimensional Biot number - given as the following (Incropera, DeWitt, Bergman, & Lavine, 2006):

$$Bi = \frac{hD}{k} \qquad (18)$$

where h, D, and k, represent the heat transfer coefficient around the heated region, the characteristic diameter of the geometry (i.e. the diameter of cylindrical heat input), and the thermal conductivity inside the heated region. According to (Incropera et al., 2006), we can assume the heated region is one lumped capacitance for Biot numbers less than 0.1. This means that at this level conduction will be large enough inside the heated region that the entire region will be the same temperature, with ± 5% error.

To make sure we account for a wide spectrum of possibilities Biot number values over the range $0.0004 < h < 40$ are presented in this transient heating model. Figure 9 shows that for any Biot number less than 4, we expect a temperature rise in the heated region of at least 300 ^{o}C. For water based nanofluids, this is well above the ambient boiling temperature.

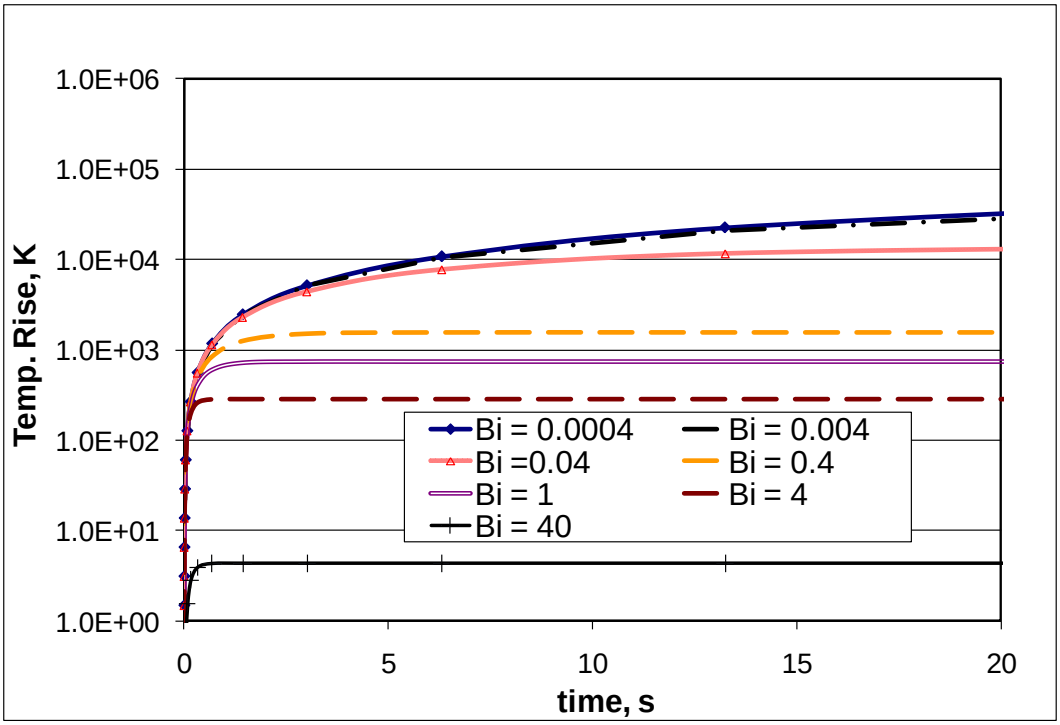

Figure 9. 1-D, transient thermal diffusion for various heat transfer coefficients at r=0

If we assume that heat is transferred from the heated cylinder by convection then we can apply natural convection correlations to find the heat transfer coefficient and the amount of heat leaving the heated area. (*Note: this analysis is only valid when heat is carried in the form of sensible heat - i.e. for*

large Biot numbers. This may not the case as the Biot number becomes small.)

To approximate natural convection from a hot cylinder or from a saturated liquid-vapor interface - at 100°C - we use the following correlation (Incropera et al., 2006):

$$Nu = \left\{ 0.6 + \frac{0.387 Ra_D^{1/6}}{\left[1 + \left(0.559/\mathrm{Pr}\right)^{9/16}\right]^{8/27}} \right\}^2 \quad (19)$$

where Pr and Ra_D are the Prandlt number and the Rayleigh number, respectively. The Rayleigh number is defined as the following (Incropera et al., 2006):

$$Ra_D = \frac{g\beta\left(T_h - T_\infty\right)D^3}{\upsilon^2}\mathrm{Pr} \quad (20)$$

where g, β, and v are the acceleration of gravity, the thermal expansion coefficient, and the kinematic viscosity, respectively. T_h, T_∞, and D are the hot cylinder temperature, the fluid temperature far away from the cylinder, and the diameter of the cylinder. Estimations of this, based on a hot temperature of 100°C and property values for water are given in Table 2. We can see that natural convection alone would be able to carry about 66 mW of the heat away from the region – if the total rate of heat entering the sample is about 120 mW. This heat input was chosen because it is the approximate input during experimentation with our Coherent, diode pumped solid state, continuous, 532 nm laser. Of course, if a different base fluid or a different heat input is used, the resulting natural convection heat transfer coefficient might significantly change. Note also, that

since we are using low volume fractions of nanoparticles we have not included any change in the base properties of water - this may also effect the results.

Table 2. Natural convection calculations

Parameter	Value	Parameter	Value
D	0.2 mm	Pr	2.75
g	9.81 m/s	v	4.75×10^{-7} m^2/s
T_h	373 K	R_{aD}	1.1×10^{-4}
T_∞	298 K	Nu	0.46
T_{film}	336 K	h	1,500 W m^{-2} K^{-1}
β	2.98×10^{-3} K^{-1}	A	6.3×10^{-7} m^2
k	0.65 W m^{-1} K^{-1}	$Q_{conv.}$	66 mW

This analysis shows that under conditions common in the following experiments, we expect natural convection to be the dominant mode of heat transfer, carrying away more than half of the input heat from the heated region. As such, it is estimated that for these conditions that the heat carried away via conduction and phase change combined are much less than 1 mW as compared to the 66 mW that convection can transfer. Radiation is also expected to be low unless temperatures inside the heated region are high - this is discussed below in section 3.3. This simple analysis also shows that under these conditions, we can

expect a Biot number of just under 1. Thus, according to the analytic results shown in Figure 9, we expect several hundreds of degree Centigrade temperature rise at the center of the heated region. This may indeed be the case if a hot wire is the heat source, or possibly for nanoparticles in this region, but water-based fluids must undergo phase change - taking up a significant amount of this heat in phase change. The amount of heat that is required for phase change on this scale is estimated in the next section.

3.2 Liquid to Vapor Phase Change

The amount of energy necessary to cause sub-cooled fluid to change phase can be approximated by the following equation:

$$Q_{total} = \dot{m}_{liquid}\, c_p \Delta T_{subcool} + \dot{m}_{vapor} h_{lv} \qquad (21)$$

where Q is the rate of heat input needed, and $\dot{m}$ is the average rate of mass changing phase during the changing phase during the trial. The specific and latent heats, c_p and h_{lv}, are defined as that of pure defined as that of pure water.

Table 3 shows the amount of heat it would take to raise the cylinder from sub-cooled conditions to vapor.

Table 3. Power needed to create a bubble in the experiment

Sub-cooled Liquid Parameters		Vapor Parameters	
D	0.4 mm	D	0.4 mm
V_{bubble}	0.125 mm^3	V_{bubble}	0.125 mm^3
p	983 kg/m^3	p	0.6 kg/m^3
$\dot{m}_{liquid}$	1.24 x 10^{-7} kg	$\dot{m}_{vapor}$	7.54 x 10^{-11} kg
Δt	1 s	Δt	1 s
ρ_{liquid}	1.24 x 10^{-7} kg/s	ρ_{vapor}	7.54 x 10^{-11} kg/s
c_p	4.2 kJ kg^{-1} $^oC^{-1}$	h_{lv}	2.26 x 10^6 kJ/kg
$\Delta T_{sub\text{-}cool}$	70 ^oC	Q_{Latent}	0.17 mW
$Q_{Sensible}$	0.036 mW	**Q_{total}**	**0.2 mW**

We can see that the rate of heating necessary to create phase change in the small volumes used in the experiment is negligible when compared to the input heat rate ~ 120 mW. This indicates that the creation of a single bubble takes relatively little energy. It should be noted, however, that if vapor is leaving the region phase change heat transfer could become significant.

There are several correlations for phase change heat transfer, but it is unclear whether they will be applicable to nanofluids under light-induced boiling. Correlations also require knowledge of the temperature at the surface and accurate measurement of fluid properties. For instance, Rohsenow's correlation as described above, requires a good estimate of surface tension and the surface constant, C_{sf}. These parameters are expected to change significantly when the

nano-sized particles *become* the surface where heat is distributed. Surface tension, particle sizing, and thermal/radiative property measurements will also be needed to fully model the system. Another important factor that requires consideration in modeling is the motion and interaction of the particles. At elevated temperatures the particles will become more active due to Brownian motion. This is expected to influence mass and heat transfer. The particles also seem to agglomerate under high irradiance leading to different optical properties and new paths for heat transfer.

Overall, this simple analysis indicates that, theoretically, natural convection should be the most important mode of heat transfer and is able to dissipate most of the heat from a small cylindrical region. This analysis also showed that very high temperature rises are possible inside the heated region. To get a more accurate model of how the heat is absorbed and emitted in the nanofluid, we need to understand the radiative/optical properties.

3.3 Radiation/Optical Properties

This research is mostly focused on how nanofluids absorb radiation. As such, this section will discuss in detail the modeling approaches that were used to examine this issue. To start, the first section will give an estimation of the radiative heat loss that is possible using the same reasoning as the last 2 sections. Next the assumption of the previous sections that a nanofluid absorbs all incoming light is scrutinized. Since a nanofluid is a composite medium, we can

using modeling techniques to determine how it absorbs light volumetrically. Lastly, a coupled optical and thermal model which brings together all the topics of this chapter will be presented.

3.3.1 Radiation Heat Transfer Estimation

A simple check for thermal radiation heat loss can be done by assuming that the heated area is a blackbody at ~100^{o}C. With this method, an estimated rate of heat loss due to radiation is about 0.08 mW, which is ~ 0.1% of the heat input. This is found from a simple radiative exchange between the surroundings and the heated region (Incropera et al., 2006):

$$Q = \varepsilon A \sigma \left(T_h^4 - T_{surounding}^4 \right) \tag{22}$$

However, the temperature could actually be much higher in the heated regions due to low thermal conductivity in the vapor as is shown in Figure 9. Since radiation is dependent on temperature to the fourth power, a significant amount of heat could be dissipated, around 19 mW (~15%) if the bubble had an effective temperature of ~1,000^{o}C. The experiments discussed in the next chapter suggest, however, that temperatures can be in the neighborhood of 350-400^{o}C, giving heat losses on the order of 1-2 mW (~1%) in the experiment.

3.3.2 Optical Property Determination: Rayleigh Approximation

In their simplest form, nanofluids are mixtures of nanoparticles (1-100 nm in diameter) and pure base fluids - such as water, alcohols, oils, glycols, molten salts, etc. If the resulting fluid is well mixed, the particles are between 1 and 100 particle diameters apart (depending on volume fraction). Also, since the particles are by definition nano-sized, the diameter of the particles are much smaller than light. Figure 10 gives a visualization of this situation (from a nano-scale viewpoint). We can see that green light (the peak of the solar spectrum) has a wavelength that is nearly 20 times as large as a 30 nm diameter particle. Figure 10 also shows how the spacing ratio (inter-particle distance to particle diameter) changes as a function of volume fraction for a stable nanofluid.

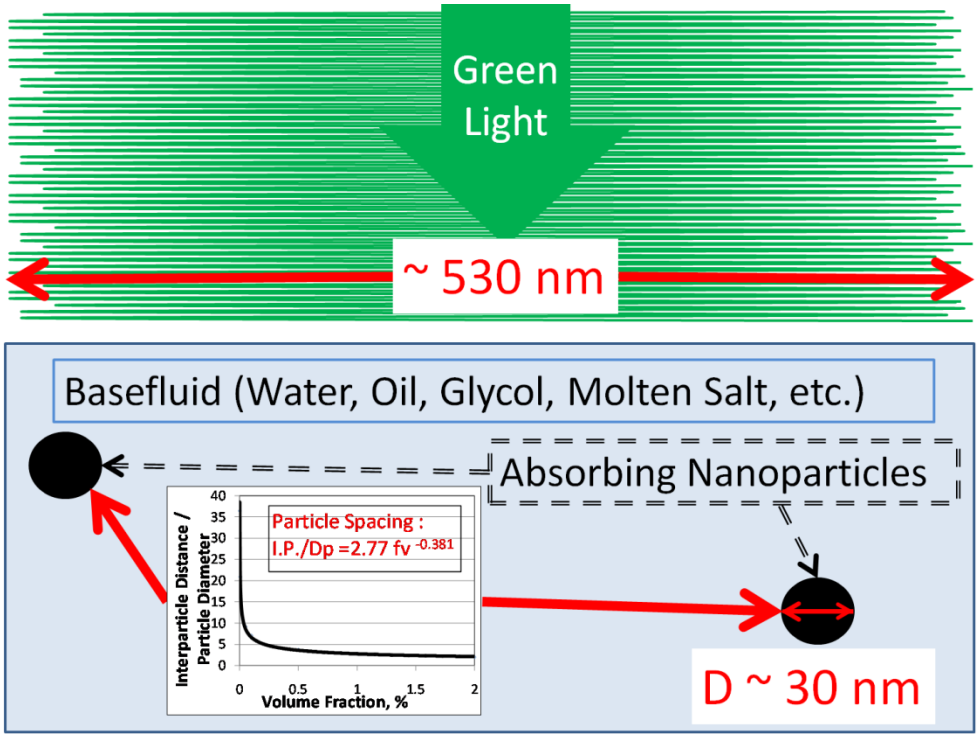

Figure 10. Schematic of the nano-scale interaction of light and a nanofluid.

Starting from these assumptions, we can now begin to determine how the nanofluid will interact with radiation. This is done by obtaining the optical properties of the bulk materials used to create the nanofluid. That is, we need to know the complex refractive index (or dielectric constant) of the base fluid and of the bulk nanoparticle material. These can be found for many pure substances in an optical properties handbook, such as (Palik, 1997). Given this information, one still needs to know the optical properties of the nanofluid mixture, which can be very difficult to predict if the nanofluid is a strongly scattering medium. At higher particle concentrations (typically more than 0.6 %v), dependent and multiple scattering phenomena can play a role since the particles are closely packed (C L Tien, 1988). However, it turns out for any solar collector with sizable absorption path lengths (anything thicker than 1 mm), an effective solar collector can be achieved at very low volume fractions. Figure 7 is a scattering regime map which helps visualize how nanofluids which are suitable for solar applications compare to other common fluids. The particle size parameter, α, which determines where on the y-axis of Figure 7 a material lays is defined as (C L Tien, 1988):

$$\alpha = \frac{\pi D}{\lambda} \tag{23}$$

where D is the diameter of the nanoparticle and λ the wavelength of incident light. Note: It is important to ensure that D and λ be of the same units to get a non-dimensional α. This non-dimensional parameter is a comparison of the circumference of a particle to the wavelength of incident light. Thus, very small particle sizes and volume fractions make it safe to assume that we are working in the independent scattering regime which allows the higher order terms of the full Mie scattering theory to be neglected. Commonly available nanoparticles are in the range 10-50 nm in average particle diameter, for which most of the incident light from the sun has a wavelength that is at least 10 times larger. As a result, the following equations can be used to solve for the scattering, Q_{scat}, absorption, Q_{abs}, and extinction, Q_{ext}, efficiencies of individual particles. These equations, termed Rayleigh approximation equations, are found in several standard texts, such as (Modest, 2003).

$$Q_{scat} = \frac{8}{3}\alpha^4 \left| \frac{m^2 - 1}{m^2 + 2} \right|^2 \tag{24}$$

$$Q_{abs} = 4\alpha \,\mathrm{Im}\left\{ \frac{m^2 - 1}{m^2 + 2} \left[1 + \frac{\alpha^2}{15} \left(\frac{m^2 - 1}{m^2 + 2} \right) * \frac{m^4 + 27m^2 + 38}{2m^2 + 3} \right] \right\} \tag{25}$$

$$Q_{ext} = Q_{scat} + Q_{abs} \tag{26}$$

where m is the relative complex refractive index of the nanofluid, and α is the size parameter given above. The relative refractive index is found through the relation:

$$m = \frac{n_{particle}}{n_{fluid}} \tag{27}$$

In general, absorbing nanofluids have a Q_{scat} of at least an order of magnitude smaller than Q_{abs} due to the fact that scattering is proportional to D^4.- as was discussed in section 2.7. Consequently, for a true, stable nanofluid scattering is negligibly small. If scattering can be neglected, the scattering coefficient simply drops out of the following equation for nanofluid extinction coefficient, $\sigma_{particles}$ (Bohren & Huffman, 1998):

$$\sigma_{particles} = \frac{3}{2}\frac{f_v\left(Q_{abs} + Q_{scat}\right)}{D} \approx \frac{3}{2}\frac{f_v Q_{abs}}{D} \tag{28}$$

Lastly, we must also incorporate any absorption of the base fluid. The above approach assumes the base fluid is totally transparent. However, water very strongly absorbs near infrared and infrared radiation. For wavelengths ≥0.9 μm, where ~35% of the sun's energy is located, water is actually a much better absorber than most of the nanoparticle materials used in this study. To find the extinction coefficient of the base fluid, we use the following equation (Bohren & Huffman, 1998):

$$\sigma_{basefluid} = \frac{4\pi k_{basefluid}}{\lambda} \quad (29)$$

where $k_{basefluid}$ is the complex component of the refractive index for the base fluid, which varies as a function of wavelength.

As a first-order approximation, we propose in this research that the total nanofluid extinction coefficient is a simple addition of the base fluid extinction coefficient, $\sigma_{basefluid}$, and that of the particles, $\sigma_{particles}$. We define this are as the following:

$$\sigma_{total} = \sigma_{particles} + \sigma_{fluid} \quad (30)$$

Note: For comparison with other research we will discuss extinction coefficients throughout in units of cm^{-1}. This means that λ, and the fluid depth, L, must be in cm in the following equation of Beer's Law (Bohren & Huffman, 1998).

$$\frac{I}{I_o} = e^{-L\sigma_{total}} \quad (31)$$

3.3.3 Optical Property Determination: Maxwell-Garnett Approximation

A different, yet common, approach to finding properties in a composite material is the Maxwell-Garnett theory. It is possible to use a Maxwell-Garnett effective medium calculation to calculate the complex refractive index. Equation 10 shows this approach, where the subscripts *eff*, *f*, and *p* define the effective

medium (i.e., the nanofluid), the base fluid, and the particles, respectively (Bohren & Huffman, 1998):

$$\varepsilon_{eff} = \varepsilon_f \left[1 + \frac{3 f_v \dfrac{\varepsilon_p - \varepsilon_f}{\varepsilon_p + 2\varepsilon_f}}{1 - f_v \dfrac{\varepsilon_p - 2\varepsilon_f}{\varepsilon_p + 2\varepsilon_f}} \right] \quad (32)$$

Note: if ε_f is very small, as it is in the complex dielectric component for water (from 0.1-1 μm), large rounding errors may occur when using this approach. This limits the applicability of this method. Once the effective dielectric constant is found, it is relatively easy to convert back to the refractive index using (Bohren & Huffman, 1998):

$$n_{eff} = \sqrt{\frac{\sqrt{\varepsilon_{eff}'^2 + \varepsilon_{eff}''^2} + \varepsilon_{eff}'}{2}} \quad (33)$$

$$k_{eff} = \sqrt{\frac{\sqrt{\varepsilon_{eff}'^2 + \varepsilon_{eff}''^2} - \varepsilon_{eff}'}{2}} \quad (34)$$

In these equations ε' and ε" represent the real and imaginary component of the dielectric constant. The real part, n_{eff}, of the refractive index for several nanofluids, determined from equations (30) and (31), is plotted in Figure 11.

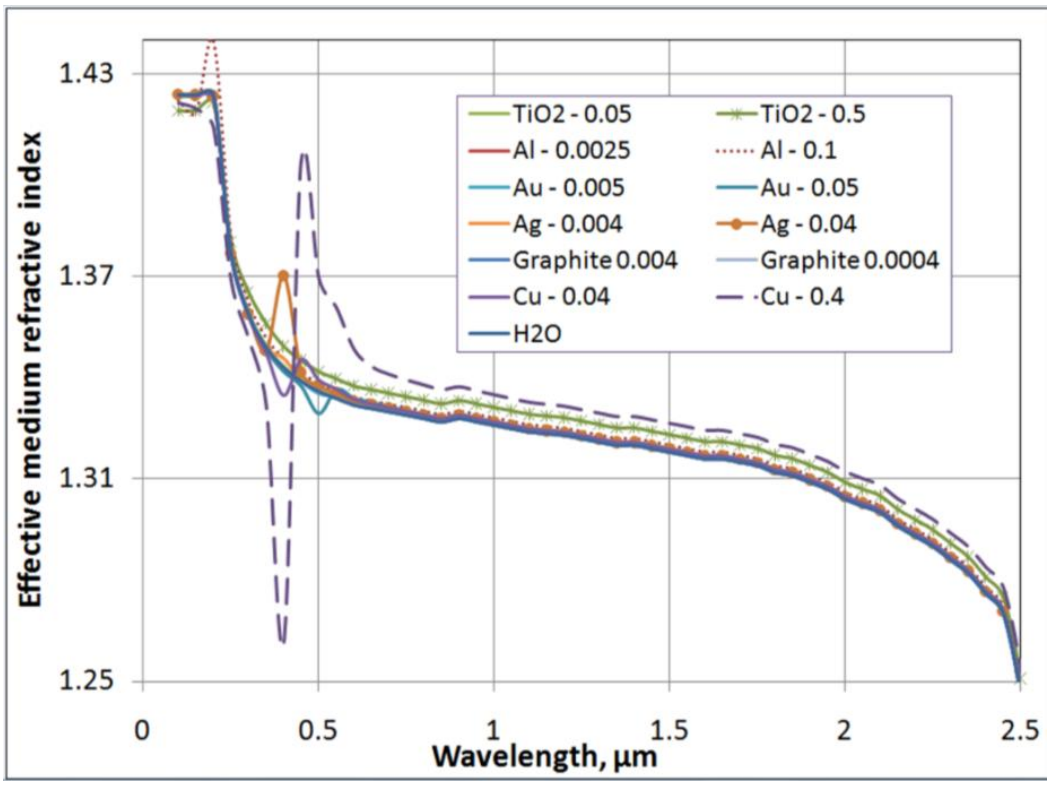

Figure 11 Maxwell-Garnet (MG) approximation of the real part of the refractive index for water-based nanofluids. The numbers in the legend represent the volume fractions of the specified nanofluids w/ 30 nm average particle size.

Since there is, at most, a factor of ten difference (and many times less than 100% change) in the real part of the refractive index between the bulk particle material and the base fluid, this approach gives rather accurate results. Figure 11 shows little deviation from the real part of the refractive index for low volume fractions, which is logical. Note: Properties for the bulk materials were taken from (Palik, 1997)for the effective medium analysis.

For the imaginary component, k_{eff}, the effective medium approach yields a severe under-prediction. For the sake of consistency, Figure 12 plots extinction coefficients, which are calculated using equation (7), with k_{eff} replacing $k_{basefluid}$. The results given in Figure 12 are many orders of magnitude below the measured values for these volume fractions. In the visible range, k_{eff} for water is many orders of magnitude (~10 orders!) less than that of metal nanoparticles. Due to this large difference, the Maxwell-Garnett theory is generally not an accurate approach to obtain the extinction coefficient for nanofluids.

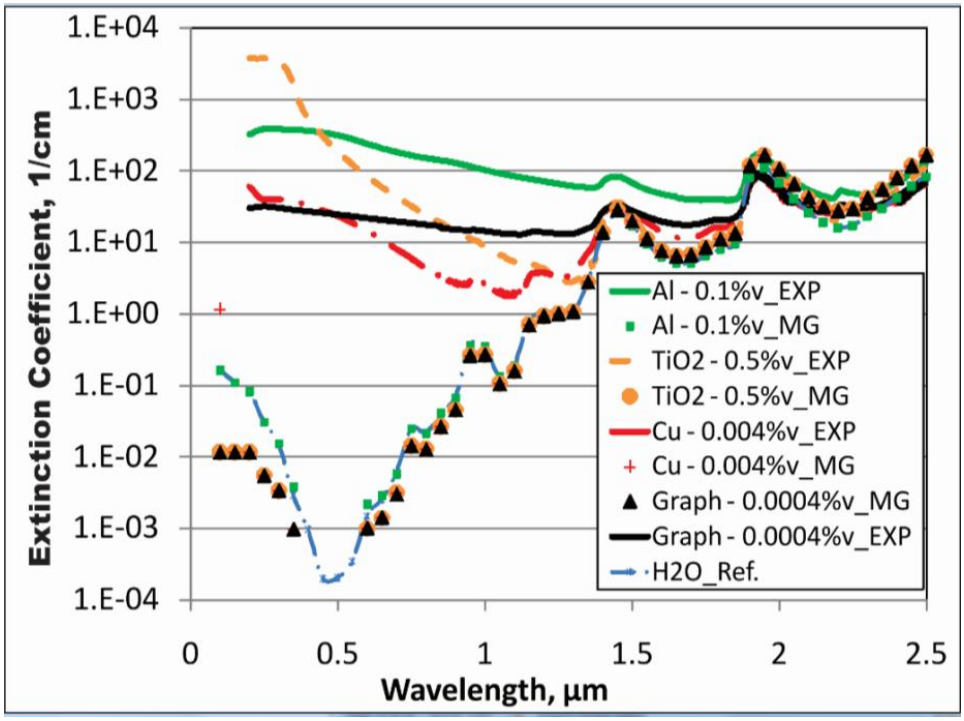

Figure 12. Maxwell-Garnett (MG) modeling of the extinction coefficient for water-based nanofluids

Another weakness of this model is that there is no way to account for scattering. Thus, the Rayleigh scattering model is a better choice because it can incorporate scattering if it is large enough to be important - e.g. in an imperfect nanofluid. Therefore, the Rayleigh scattering model will be the main model used in the remainder of this manuscript.

3.4 Nanoparticles as Photothermal Converters

In the previous sections, nanofluids were looked at as a far-field, bulk absorbing fluid. Up to this point, we have discussed the bulk heat transfer in a nanofluid via conduction, convection, phase change, and radiation, but neglected that the bulk properties arise from individual particles. Therefore, this section will take more of a 'bottom-up' or 'near-field' approach to nanofluid heat transfer modeling.

3.4.1 Individual Particle Heat Transfer

To truly understand heat transfer in a nanofluid we also need to understand heat transfer around a individual particle. In this section we will do this analytically by applying the heat equation on that, very localized, scale. The diffusive heat flow equation for a homogeneous medium with a source term can be written as the following (Carslaw & Jaeger, 1986):

$$k\nabla^2 T + \frac{dq}{dt} = c_p \frac{\partial T}{\partial t} \tag{35}$$

where k is the thermal conductivity, T the temperature field, c_p the specific heat capacity and t time. The term, $\frac{dq}{dt}$, is the power generation term for a single nanoparticle. This term can be estimated from the concentration of light hitting a particle, particle characteristics (material, size, and shape), and the particle's resulting absorption properties (as discussed above). Also, this solution can be significantly simplified by only solving the symmetric 1-dimensional case.

This use of this approach, however, needs some justification. A big implicit assumption is that heat transfers nearly instantaneously across the characteristic distances involved. More specifically, this equation is only valid if the heat carrier (phonon or electron) has a mean free path smaller than the nanoparticle dimension. In most crystalline solids, mean free paths are on the order of tens of nanometers. Thus, a 'lagging' term which accounts for a finite time of heat transfer should be incorporated when modeling small-scale heat transfer in most solids. In contrast, liquids and amorphous solids - due to their lack of a crystal structure - have very short, < 1 nm, mean free paths (Keblinski, et al., 2006), (Sheonogin et al., 2004). Since we are mostly interested in the surrounding liquid outside of the particle, the use of the heat equation is justified. The assumption of symmetry can be argued through the use of the Biot number. To restate, the Biot number is the ratio of convective forces to conductive forces, and is defined as the following (Incropera et al., 2006):

$$Bi = \frac{hD}{k} \tag{36}$$

For a conservative estimate of metallic nanoparticles, the characteristic dimension, D, is on the order of 100 x 10^{-9}, and the thermal conductivity is on the order of 100 W $m^{-1}K^{-1}$. Thus, if the convective heat transfer coefficient is less than 100 million W $m^{-2}K^{-1}$, an individual particle can be thought of as a lumped (read: symmetric) heat source inside the fluid. In other words, because a metallic nanoparticle is relatively thermally conductive and extremely small, it can be uniformly treated as a homogeneous heat source. This is likely to be the case for all reasonable particle temperatures.

Equation 34 can be solved by the method of Laplace transforms as is described in (Carslaw & Jaeger, 1986). The initial and boundary conditions for this situation are the following:

$$\left.\frac{\partial T}{\partial r}\right|_{t=0} = 0 \tag{37}$$

$$\left.\frac{\partial T}{\partial r}\right|_{r=R} = \frac{dQ}{dt} \tag{38}$$

$$T_{r=\infty,t=t} = T_{\infty} \tag{39}$$

These initial and boundary conditions can be described as the following: initial thermodynamic equilibrium, constant heat flux at the particle surface, and constant temperature far away in the infinite medium. Note: 'infinite' means from

the perspective of the particle medium - i.e. generally more than 10 particle diameters between particles.

Using all these assumptions we have derived the following solution to the heat equation. This equation is validated by the fact that with some modification it is equivalent to the solution presented in (Keblinski et al., 2006):

$$T(r,t) - T_\infty = \frac{Q_{particle}}{4\pi r k}\left[erfc\left(\frac{r-R}{2\sqrt{Dt}}\right) - \exp\left(\frac{r-R}{R} + \frac{Dt}{R^2}\right) erfc\left(\frac{r-R}{2\sqrt{Dt}} + \sqrt{\frac{Dt}{R^2}}\right)\right] \quad (40)$$

$$for \quad r > R$$

where T represents temperature and the independent variables, r and t represent distance in the radial direction and time, respectively. $Q_{particle}$ is the total power generated by the nanoparticle and k is thermal conductivity. The functions denoted *erfc( )* and *exp( )* are the complementary error function and the exponential function. Lastly, R and D represent the particle radius and the thermal diffusivity of the liquid, which is defined as (Incropera et al., 2006):

$$D = \frac{k}{\rho c_p} \quad (41)$$

Note that, for water, $D \sim 1 \times 10^{-7}$ m^2/s.

There are a couple of interesting limiting conditions which arise from eqn. 39. For example, as $r \to \infty$ or $t = 0$, the *erfc ( )* function approaches 0, and the resulting temperature approaches T_∞, $T \to T_\infty$. This indicates that our final

equation checks with the boundary conditions For $t \to \infty$ at $r = R$ - representing the highest steady state temperature expected - we get the following:

$$T(r) = T_{\infty} + \frac{Q_{particle}}{4\pi k R} \tag{42}$$

For this simplified equation, the difficult task is to determine the maximum possible heating rate, $Q_{particle}$. Taking the maximum achievable focused laser power in the experiments of the next chapter to be 770 W cm^{-2} and an absorption cross section of a nanoparticle to be 5 x 10^{-14} m^2, it is possible to have a nanoparticle be a generator of up to 4 x 10^{-7} W. With a 30-nm particle, this will result in a temperature rise around the particle of nearly 3.25 ^{o}C. It should also be noted that this can be achieved exceptionally quickly. The characteristic time of the above equation can be determined from solving for the following quantity:

$$t_{diffusion} = \frac{R^2}{D} \tag{43}$$

Since R less than 50 nm and D ~ 1 x 10^{-7}, the characteristic time is less than 25ns. After several time constants, say 4 time constants or ~100 ns, we expect the local region to come close to the steady-state temperature. Thus, this analysis indicates that in a sub-cooled, liquid water surrounding fluid, steady state is reached very quickly and that the localized temperature rise is modest. If, however, the surrounding fluid is at saturated conditions and vapor forms around the particle - which has a much lower thermal conductivity, 1/40th that of liquid water - much

higher temperatures can result. Since the maximum achievable temperature is inversely related to thermal conductivity, a 1/40th reduction in thermal conductivity could theoretically give a temperature rise around the particle of 130 ^{o}C. The next section will discuss how vapor may form around a single nanoparticle or a group of nanoparticles and the resultant forces that are theoretically present.

3.4.2 Vapor Nucleation and Kinetics in Nanofluids

While on the topic of vapor generation in a nanofluid, it is interesting to discuss bubble nucleation and kinetics. Since much of this takes place on nano/micro temporal and spatial scales, for the most part these answers lie below the resolution limits of our experimental set-up. Therefore, the discussion of this chapter is mostly academic/theoretical. Nonetheless, this section will attempt to answer the following questions: What temperatures and pressures are expected inside nano-sized bubbles? How do bubbles nucleate? How fast do bubbles grow? What are the buoyancy forces on the resulting bubbles?

The answer to the first question can be estimated by the Young-Laplace equation simplified for spherical coordinates (Carey, 2007):

$$P_{vapor} - P_{liquid} = \frac{2\sigma}{R} \qquad (44)$$

where P_{vapor} and P_{liquid} are the pressures inside and outside of the bubble. The parameter, σ, is the liquid vapor surface tension, and R is the radius of the bubble.

It was found by (Matsumoto & Tanaka, 2008) through Lenard-Jones molecular dynamic simulations that the Young-Laplace equation holds even for nano-sized bubbles. (Matsumoto & Tanaka, 2008) also indicated that planar values for surface tension are good approximations even for the very high curvatures of nano-sized bubbles. Thus, if we take $\sigma = 0.04$ N/m (water's surface tension at ~ 300 ^{o}C) and R = 10 nm (the smallest particles we use in the experiments), we expect the vapor pressure inside a bubble to be ~ 8 MPa (about 80 atmospheres) from the Young-Laplace equation. If we assume the vapor inside this bubble is saturated, the saturation temperature at 8 MPa is ~295 ^{o}C. As the bubble becomes larger the pressure and temperature inside it is likely to go down.

As will be discussed later in the experimental section, nanoparticles have a tendency to agglomerate. This always happens to some extent, despite treatment with surfactant or other methods. This is, in part, due to the fact that nature seeks to reduce surface energy and nanoparticles have a lot of surface area. This fact also holds for bubble nucleation as well (Carey, 2007). Because of this bubbles tend to nucleate at certain sites - usually micro-cavities on a solid surface (Carey, 2007). In the case of a nanofluid, however the particles themselves are heat sources. Therefore, while bubbles may be formed around individual particles, it is more likely that bubbles form in concave sites inside particle agglomerates - see Figure 13.

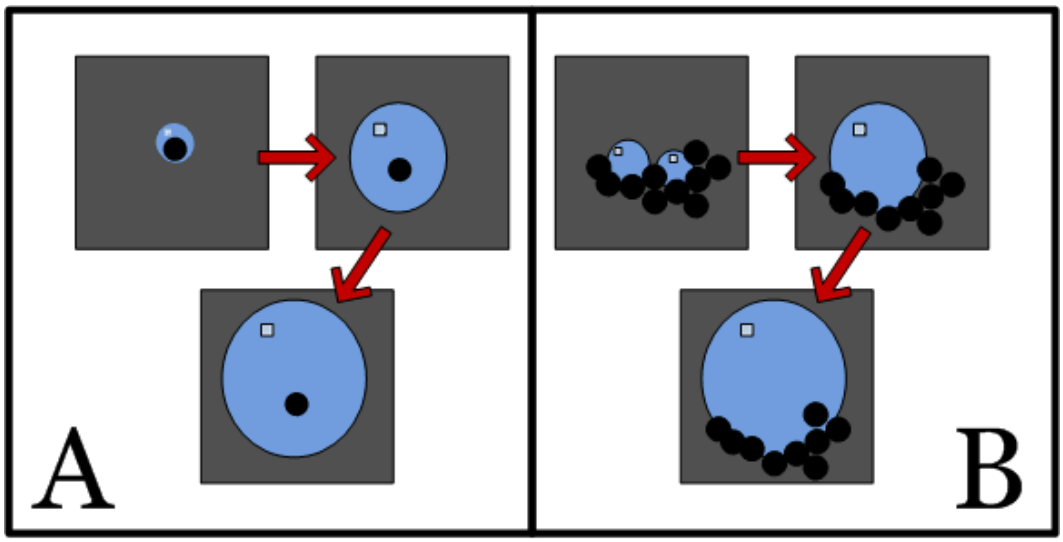

Figure 13. Bubble formation paths - (A) Bubble formation around a singular particle, (B) Bubble formation on particle agglomerates

The next question we will estimate is how fast do bubbles grow. To answer this question we can draw on a rich, extensive body of research. This topic can be discussed in terms of two bounding models - inertial driven bubble growth (fast) versus heat-transfer-driven bubble growth (slow/steady-state growth). There are also several correlations which essentially track between these extremes, but which are based on empirical data for given conditions. We did not have time to test all of the parameters that determine where our situation lies.

Inertial-driven bubble growth is driven by pressure differences inside and outside of the bubble. Forces which are initially out of equilibrium cause the bubble to expand at a very fast rate. The simple Rayleigh solution to this problem results in the following simplified equation (Carey, 2007):

$$D(t) = 2t\sqrt{\frac{2}{3}\frac{T_\infty - T_{sat}}{T_{sat}}\frac{\rho_{liquid}h_{lv}}{\rho_{vapor}}} \quad (45)$$

where D is the diameter of the bubble and t and T are time and temperature respectively. The constants ρ_{liquid}, ρ_{vapor}, and h_{lv} are the liquid density, vapor density, and latent heat of phase change from liquid to vapor. In this equation the bubble grows linearly with time. This growth is shown as the upper curve in Figure 14.

The other extreme, heat transfer -induced growth, is governed by the following equation (Carey, 2007):

$$D(t) = 4Ja\sqrt{3\pi\frac{k_{liquid}c_{p,liquid}}{T_{sat}}t} \quad (46)$$

where D is still the diameter of the bubble as a function of time, t. The constants k_{liquid}, $c_{p,liquid}$ are the liquid thermal conductivity and the specific heat of the liquid, respectively. The nondimensional variable Ja is the Jakob number and is defined as (Carey, 2007):

$$Ja = \frac{\rho_{liquid}c_{p,liquid}}{\rho_{vapor}h_{lv}T_{sat}}(T_\infty - T_{sat}) \quad (47)$$

For this equation, we can see that the bubble size is dependent on the square root of time. Thus, it is a much slower mechanism of growth than inertia driven growth.

It follows that bubble growth is initially inertia-controlled, while at longer times, the growth is heat transfer-controlled. That is, based on the thermo-physical properties of the fluid and the boiling surface we expect to see fast initial growth and slow steady-state growth. It has been argued by a number of researchers that there should be a smooth transition between these two extremes (Carey, 2007), (Mikic & Rohsenow, 1969), (Griffith, 1956). One very simple approach to determine this transition is to find a transitional radius below which growth is inertia-controlled and above which is heat transfer-controlled. This transitional radius is given by (Carey, 2007):

$$R_{transition} = \frac{\left(\frac{12k_{liquid}}{\pi \rho_{liquid} c_{p,liquid}} \right) Ja^2}{\left\{ \frac{2\left[T_\infty - T_{sat}\left(P_\infty\right)\right] c_{p,liquid} \rho_{liquid}}{\rho_{vapor} h_{lv}} \right\}^{1/2}} \quad (48)$$

That is, we estimate that bubble growth follows inertia-induced bubble growth until the transition size, where it then follows heat transfer growth. This estimate is shown as the middle (dashed) curve in Figure 14.

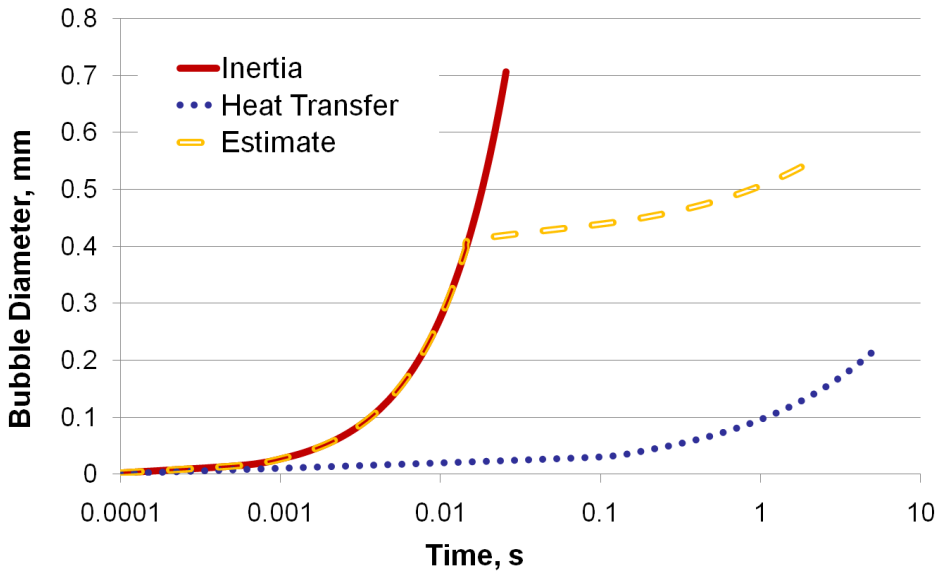

Figure 14. Bubble size approximations for inertia induced bubble growth, heat transfer induced bubble growth, and an estimate of Zubber's correlation for nucleate bubble growth.

Another question mentioned above is what are the forces acting on a vapor bubble? In order to see sizable forces, we will examine a larger bubble that encompasses the larger heated area. In this region we assume that forces are balanced and there is a restricting force in the downward direction which balances with the buoyancy/thermal convective forces pulling the bubble upwards. In the experiments of the next section, we have seen a cylindrical bubble roughly 0.4 mm diameter and a 0.1 mm depth. For this situation the total force in the positive y-direction is calculated to be ~ 0.12 μN. A free body diagram of the forces is shown in Figure 15.

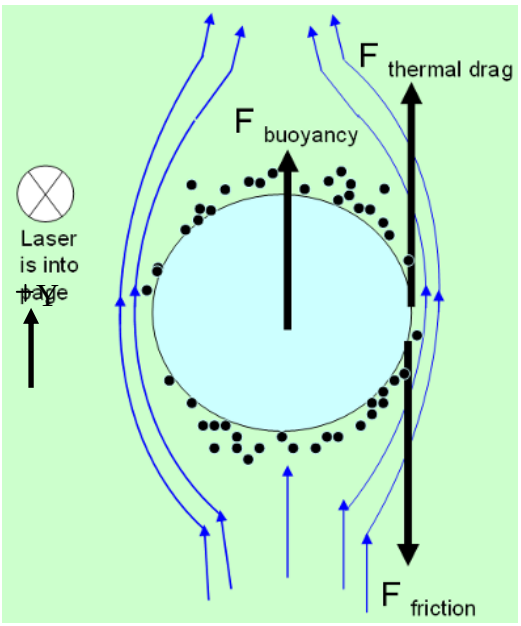

Figure 15. Free body diagram of bubble during the experiment

It is proposed that the force of friction from the bubble being pressed against the front and back surface of the cuvette provides the balancing force. Van der Waals forces holding the particles together or other particle/bubble interactions could also provide the necessary restricting force in the negative y-direction. Either way, the buoyancy and/or restrictive forces on a single, relatively large bubble are very small. We expect the forces to be orders of magnitude smaller on the nano-scale bubbles shown in Figure 13.

3.4.3 Superposition of Particles

Another analysis that can be done without too much difficulty is heat diffusion surrounding a group of heat generating nanoparticles. That is, if each

particle absorbs some heat, then the total heat input will be dependent on the particle absorption cross section and the density of absorbers. The following equation, which is slightly modified from ΔT_{global} presented by (Keblinski et al., 2006) gives an estimate for the steady-state temperature rise on the outside surface of the heated region in a light absorbing nanofluid:

$$\Delta T = \frac{\rho_N R^2 I \sigma_a}{2k} \tag{49}$$

where ρ_N is the particle density, R the radius of the heated region, I the irradiance, σ_a the particle absorption cross section, and k the thermal conductivity of the surrounding fluid. It should be noted that this equation applies to steady state in an infinite medium. Also, this equation implies a homogenous medium and thus does not take into account contact resistance. The main difference between this analysis and that of section 3.4.1 is that a particle density is included which also implies that as compared to a single point heat source this analysis can be thought of as a superposition of heat sources. Table 4 shows the values used to calculate the temperature rise in the heated region.

Table 4. Values used during this conduction analysis

Parameter	Value	Parameter	Value
$D_{particle}$	30 nm	k_{water}	0.65 W/(m K)
R	0.125 mm	α_{water}	1.2×10^{-7} m^2/s
$V_{heated\ region}$	0.012 mm^3	I_{laser}	766 W/cm^2
f_v	0.0004-0.1%	σ_a	1.15×10^{-16} m^2
T_∞	298 K	Particles/mm^3	70 billion

This solution is plotted for a wide range of particle densities in Figure 16. This analysis gives similar results to that of the convection analysis presented above. As in the previous analysis - all things being equal - very high temperature differences between the sub-cooled surrounding fluid can be achieved - up to 500 ^oC. Since this can take place in less than a millimeter, we expect temperature gradients of up to half a million degrees centigrade per meter.

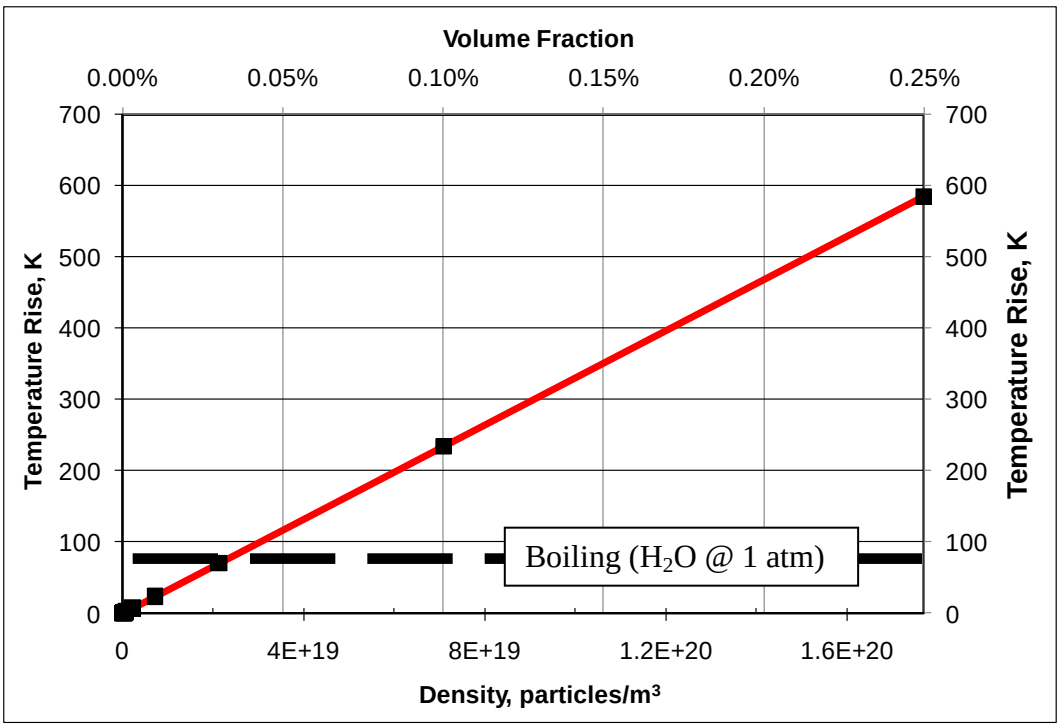

Figure 16. Temperature rise in heated region for various concentration groups of graphite nanoparticles

It is also interesting to note even at a uniform 0.1% volume fraction almost 70 billion - 30 nm particles are expected to be present and interacting in a volume of just 1 mm^3!

3.5 Finite Element Modeling

To determine how a proposed solar collector might perform without actually building it, we must use a model. For this paper a general discretized, numerical model is used. The model is a coupled solution of the radiative transfer

equation and energy equation, and is briefly described in the following section. In short, the optical properties of small particles (which are relatively far apart) can be found without too much difficulty. After the optical property calculations given above, the extinction coefficient, $\sigma_{e,\lambda}$ can be found such that:

$$\sigma_{e,\lambda} = f\left(bulk.properties, D_p, \lambda, f_v\right) \quad (50)$$

That is, $\sigma_{e,\lambda}$ is a function of material, particle size, wavelength, and the volume fraction. The most commonly available nanoparticles are in the range of 10-100 nm (MTI, 2011). For this study we will assume 20 nm average diameter particles to limit the number of variables. Also, choosing a receiver depth of 5cm we find that a ~0.01% volume fraction will absorb >95% of the incoming light in one pass. After these assumptions are applied, the extinction coefficient versus wavelength is plotted in Figure 17 for some common highly absorbing materials. These results take into account the fact that the size of these particles is on the order of the mean free path size of electrons. A simple Drude model is also used to account for this as described in (Hunt, 1978). Accounting for particle size essentially broadens the absorption peaks (and slightly lowers them).

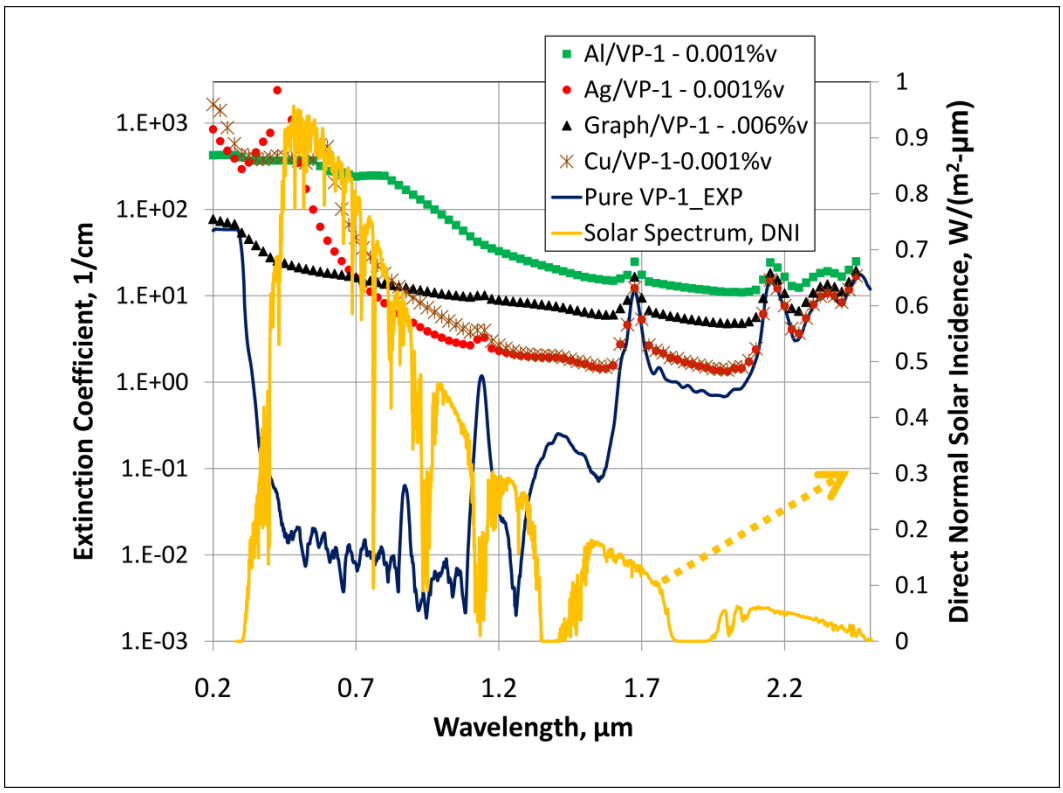

Figure 17. Extinction coefficient over the visible range for copper, graphite, silver, and gold—*D*=20 nm, *fv*=0.1%. The "Pure VP-1_ EXP" is an experimental result for the pure base fluid, Therminol VP-1—as found with a Jasco V-670 spectrophotometer.

One major loss of energy in the receiver is from reflections off the surface of the absorbing fluid. In order to make sure this is not a major drawback, we modeled the reflectivity using the Maxwell-Garnett effective medium theory. Note: if only the real part of the refractive index is used, the Maxwell-Garnett model is a reasonable approach. Next, reflectance at the fluid interface (simplified for normal incident light) can be found. The following equations are used (Pettit & Sowell, 1976):

$$\frac{\varepsilon_{eff} - \varepsilon_f}{\varepsilon_{eff} + 2\varepsilon_f} = f_v \frac{\varepsilon_p - \varepsilon_f}{\varepsilon_p - 2\varepsilon_f} \quad (51)$$

In this expression, ε and f_v are the dielectric constant and the volume fraction respectively where the subscripts *eff*, *f*, and *p* define the effective medium (what we are solving for), the fluid, and the particles, respectively. Once we know properties for the effective medium we can apply the following Fresnel equation to estimate reflectance (assuming light is near normal incidence) (Pettit & Sowell, 1976):

$$\Re = \frac{\left(n_{eff} - n_{air}\right)^2}{\left(n_{eff} + n_{air}\right)^2} \quad (52)$$

In this expression, *n* is the refractive index and $\Re$ is used to represent reflectance and distinguish it from thermal resistance, *R*. Also, the subscripts *eff* and *air* denote the effective nanofluid and air, respectively. It should be noted that any variation due to temperature is neglected in these calculations.

These results are compared in Figure 18 to a selective surface absorber. These results show that, according to our model, a nanofluid receiver would actually lose less of the incoming radiation to reflections than a selective coating. Note that there are several nanofluid materials that have essentially coincident curves over the solar spectrum (except for a slight deviation in copper between 04-0.5 μm) in Figure 18.

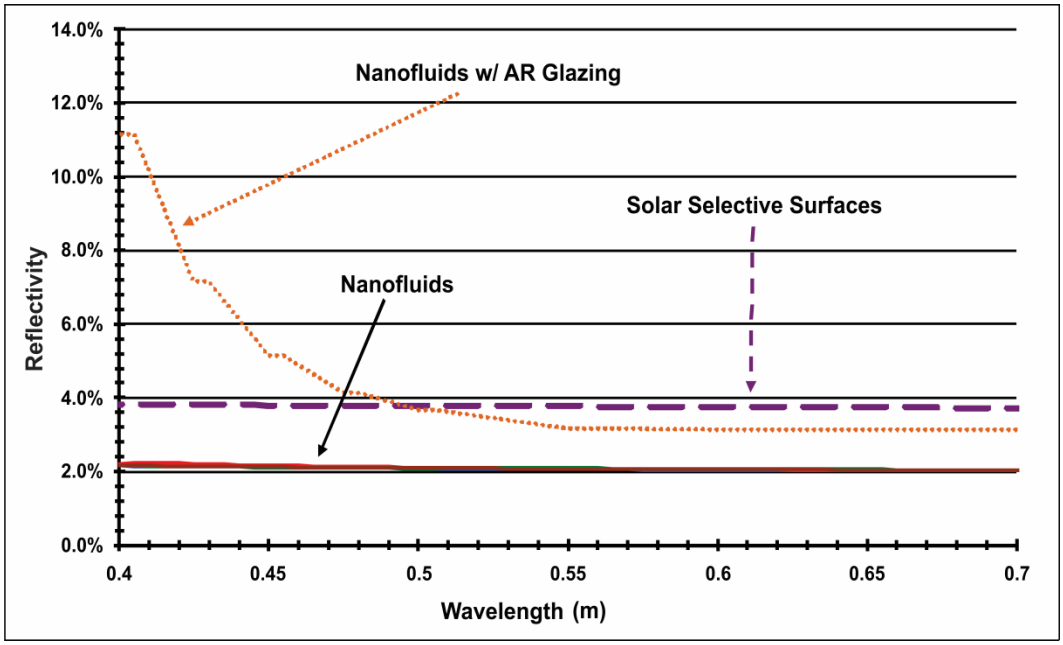

Figure 18. Reflectivity as a function of the wavelength of copper, graphite, silver, and gold (20 nm) nanofluids with a volume fraction of 0.1% and (w/ and w/o) glazing as compared to that of a conventional selective surface absorber (Pettit & Sowell, 1976).

Of course, these reflective losses are only one part of a whole gamut of optical losses which add up to de-rate solar receivers. Dust in the system, limitations in the mirrors, etc. will most likely add to account for a much larger share of the losses in optical efficiency. System optical efficiencies are usually, at best, 80-90% for new, very clean optics .

After the optical properties are found, we must numerically solve the following one-dimensional radiative transport equation, which can be found in standard radiation texts such as (Modest, 2003):

$$\frac{dI_{i,\lambda}}{dy} = \sigma_{a,\lambda} I_{b,\lambda}(T(y)) - \sigma_{e,\lambda} I_{i,\lambda} \tag{53}$$

where $\sigma_{a,\lambda}$ is the spectral absorption coefficient. The subscript *i* is used to keep track of which direction light is propagating – i.e. either incoming (+1) or outgoing (-1) light. As described in (S. Kumar & C.L. Tien, 1990), the boundary conditions are the following:

$$I_{-1,\lambda}(L) = \varepsilon_{w,\lambda} I_{b,\lambda}(T(L)) + \rho_{w,\lambda} I_{+,\lambda} \tag{54}$$

$$I_{+1,\lambda}(0) = S_{\lambda} + \rho_{g,\lambda} I_{-1,\lambda}(0) \tag{55}$$

For these equations we need to know: spectral reflectance of the wall and the glazing, respectively, $\rho_{w,\lambda}$ and $\rho_{g,\lambda}$, and the spectral radiation incident on the receiver S_{λ}. The spectral wall emittance, $\varepsilon_{w,\lambda}$, is also needed. We also assume incoming light to be blackbody radiation – i.e. the following equation is used (Modest, 2003):

$$I_{\lambda}(T) = \frac{2hc_0^2}{\lambda^5 \left[\exp\left(\frac{hc_0}{\lambda k_B T} \right) - 1 \right]} \tag{56}$$

where *h* is Planck's constant, k_B the Boltzmann constant, and c_0 the speed of light. To model the temperature profile we need to couple the above equations with the following 2-D energy equation and its boundary conditions.

The equations necessary for this model are the following (Modest, 2003):

$$k \frac{\partial^2 T}{\partial y^2} - \frac{\partial q_r}{\partial y} = \rho c_p U \frac{\partial T}{\partial x} \tag{57}$$

$$x = 0,\ 0 < y < L \quad T(0, y) = T_{inlet}$$
$$y = L,\ x > 0 \qquad q_r(L) - k\left.\frac{\partial T}{\partial y}\right|_{y=L} = 0 \tag{58}$$

where k, ρ, c_p, *and* U are the fluid thermal conductivity, density, specific heat, and velocity, respectively. To simplify the model, the velocity profile is assumed constant. Further, we also assume an overall loss coefficient (which combines convection and radiation) at the boundary to be in the range of 15-25 W $m^{-2}C^{-1}$ - depending on fluid temperature. Finally, we shall define receiver efficiency as:

$$\eta = \frac{\dot{m}c_p\left(T_{out} - T_{in}\right)}{CG_T A_R} \tag{59}$$

where $\dot{m}$, c_p, T_{out}, T_{in} are the mass flow rate, specific heat, and outlet and inlet temperatures of the fluid, respectively. Also, C, G_T and A are the concentration ratio, the solar irradiance, and the collector area. It should be noted that G_T is spectrally calculated from the results of equation (51). The interested reader can find more details on this model (developed by colleagues) in references (Tyagi, 2008) and (Otanicar, 2009).

Once the general model is developed it is simply a matter of conducting a parametric study to see which solar concentration ratios, nanoparticle volume fractions, receiver geometries, fluid flow rates, etc., show comparable results to conventional systems. The next section - which deals with the experimental works of this research - will present these results. This is done because these results are better shown in context - i.e. in comparison to experimental results.

3.5. Commercial Finite Element Analysis Software

In addition to the user developed code described in the last section, it is useful to compare experimental and modeling results with analysis in commercial software. To accomplish this goal, Simens NX 7.5 product life-cycle management software is used. This software package is very general and versatile for engineering applications. To name a few of its capabilities, NX provides 3-dimensional CAD modeling, relatively user-friendly finite element meshing, and mechanical simulation - specifically, coupled thermal/flow analysis. With some experience, this software can solve complicated heat transfer problems in a relatively short time - i.e. a few hours. The only disadvantage of using this software package is that it may be too general for solving unique/uncommon problems. To address this disadvantage, a simplified version of experimental conditions is modeled with NX 7.5. That is, simple cuboids, cylinders, and combinations of those are modeled and analyzed in this process. Figure 19 shows describes the thermal/flow simulation capabilities of the software and some sample graphics generated in the software including a cuboid which approximates the cuvettes used in experimental testing of next chapter. Notice the second Cartesian ordinate axis found near the middle of the cuvette model (right side of Figure 19). This second Cartesian ordinate axis is required to define a spatially varying heat load at this location. The spatially varying heat load approximates

volumetric absorption of collimated light energy - a feature of the experiments discussed in the next chapter.

Figure 19. Relevant Siemens 7.5 CAD/FEA capabilities (left) and a sample image of a 2mm x 2mm x 35 mn open-top cuvette used in this analysis (right)

There are several steps necessary to achieve a valid modeling simulation in this software. These can be roughly broken down into the following: building

the model, meshing the model, defining simulation parameters, and finally post-processing the results.

Building a simple model (for this analysis) is done in the same manner as other 3-D modeling software (AutoCAD, SolidWorks, ANSYS, etc.) with which most people with an engineering background are familiar. In particular, one starts with sketch a two dimensional drawing of the part. In the case of the part shown in Figure 19, this is simply a 2mm X 2mm square. This sketch can then be built to a three dimensional cuboid by using the 'extrude' command and specifying a direction and distance for the extrusion. To make a toroid or a cylinder a circle or square can be 'revolved' around an axis - if direction and total angle of rotation is specified. If one needs more complicated geometries these three-dimensional bodies can be added to or subtracted from each other. For this design, a cylinder is subtracted from the center of the cuboid. This subtractive cylinder (or hole) is started at the secondary Cartesian ordinate axis. This allows our model to avoid modeling nanofluid radiative properties.

Once the model is defined satisfactory, one can move on to the finite element meshing component of the software. This is done by choosing 'new fem' from the drop-down menu. In older software programs, meshing three dimensional objects was a challenge. In NX it is relatively fast and easy to make complicated spatially varying three dimensional tetrahedral (used in this research) or higher order mesh elements throughout the solid body. For this

research, a very tight mesh is used around small features and a relatively large mesh gradually achieved through the bulk of the solid body. Thus, there are ten times as many nodes around the heated region as there are far away in the surrounding fluid. Note: when running the simulation one must iteratively change the mesh size until the same results are achieved with significantly smaller mesh elements. For the conditions used in this model, mesh convergence is reached when the small features have elements on the order of 0.01 mm. For the bulk elements the mesh size is on the order of 0.1 mm.

After the mesh is determined, the next step is to input boundary and initial conditions. For this simulation a uniform initial temperature of 20oC inside the model is defined in the 'initial conditions' tab. For this model, the upper-top of the cuvette is defined as a free surface. This allows fluid to evaporate (or boil) out of the test cell when that solver feature is turned on. To match with the experimental environment, a forced convection boundary condition were placed on the outside of the part. To set this boundary condition, the velocity in the surrounding fluid (in this case 7.8m/s air at 80^{o}C) is input. Most importantly the heat load input needs to be defined at this stage. In addition to the convective boundary, Figure 20 shows an exponentially varying heat flux input. This was chosen to approximate exponentially varying light absorption in the volume of the fluid.

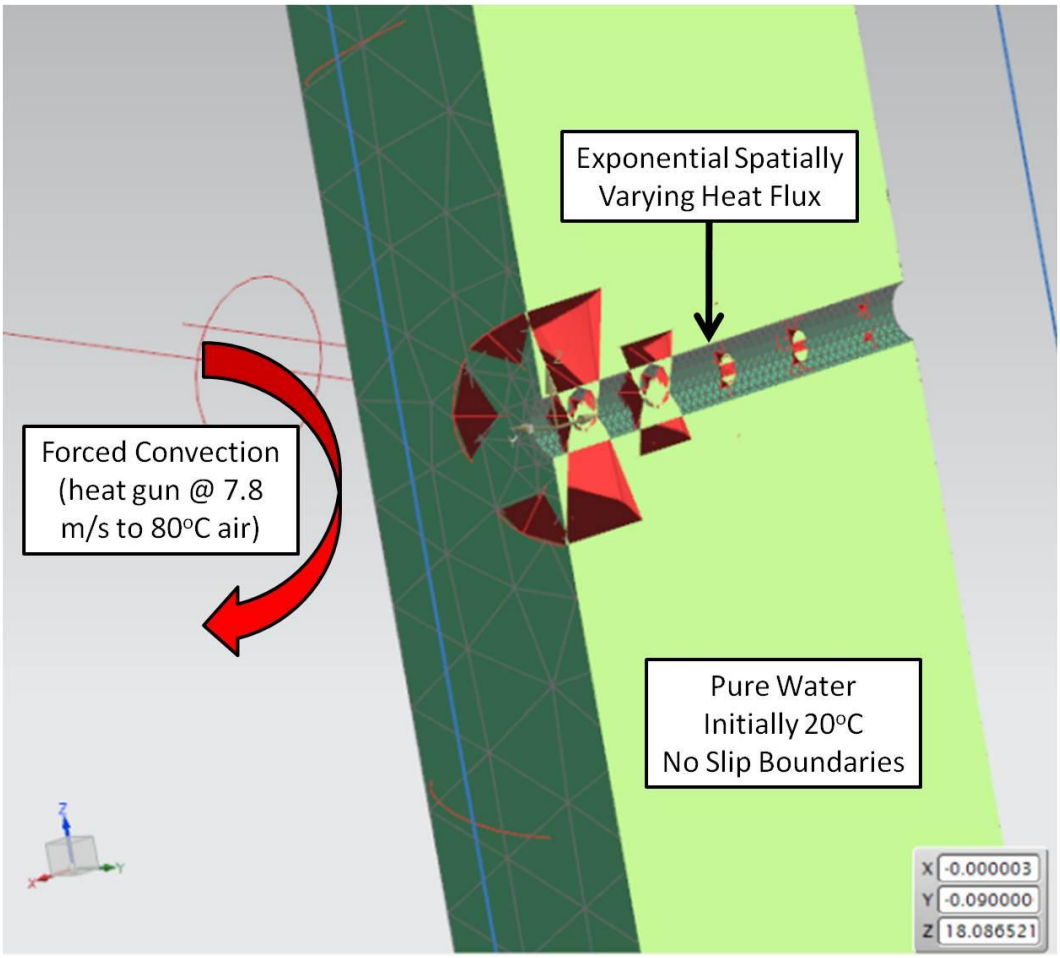

Figure 20. Sectioned, zoomed in view of an exponentially decreasing heating.

Once all the properties, initial conditions, and boundary conditions are assigned, we are ready to run the simulation. Since there are many parameters available - even in selected thermal/flow solver module - one should carefully check to make sure that all the desired information is correctly input. These dialogue windows are shown in Figure 21. Also, shown in Figure 21 is the convergence graphs which can be displayed while the simulation is running. The

real-time level of convergence is indicated by the value of the residuals. These are essentially a measure how much one iteration differs from the next across all the nodes of the solid mesh. When running the simulation the first few times, a relatively large tolerance for the residuals (≥ 0.001) is prudent because it will solve quickly - as is shown in Figure 21. When final results are desired tighter convergence criteria might be desired.

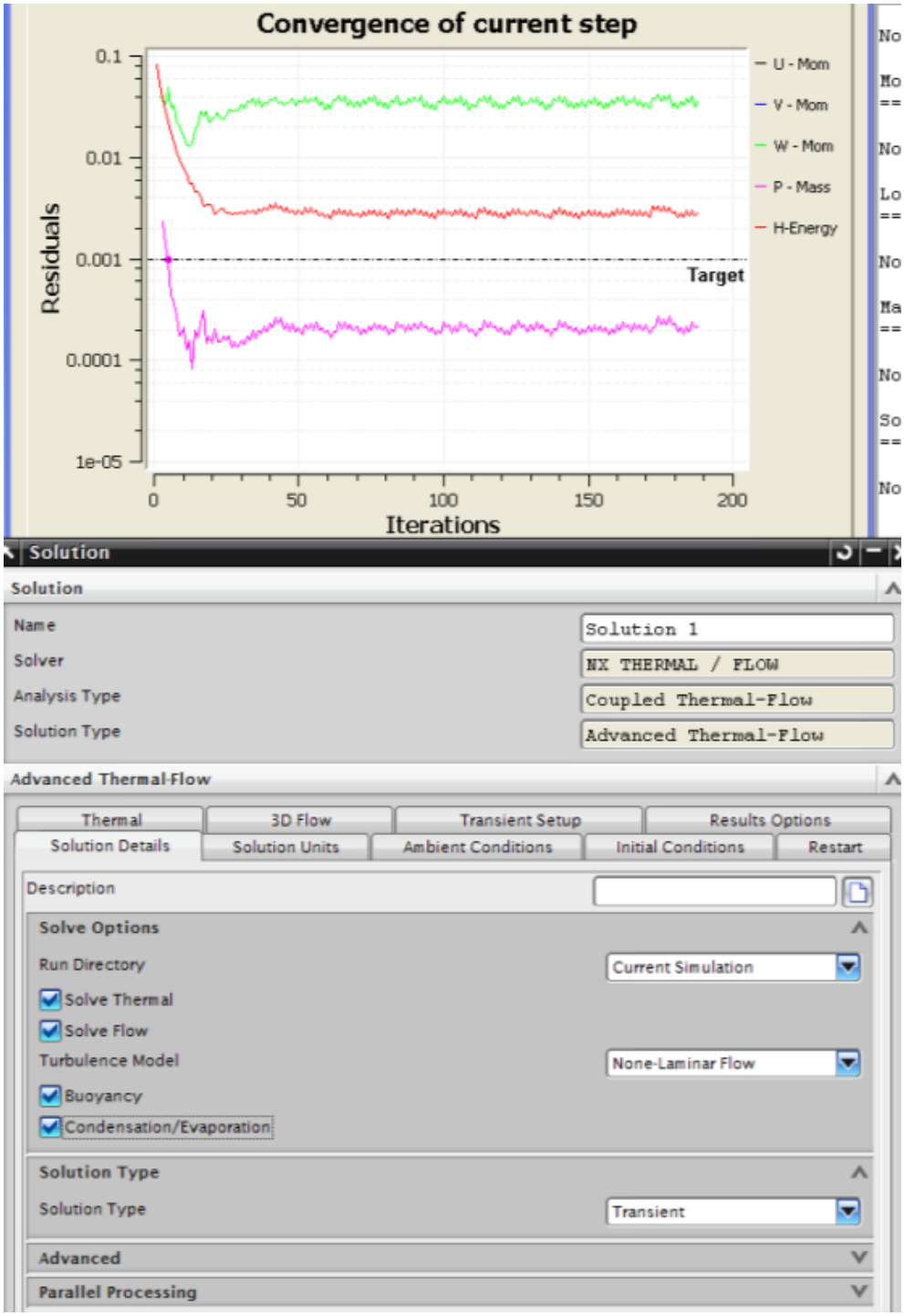

Figure 21. Dialogue boxes to control solution parameters.

After convergence and mesh size are deemed acceptable, one can run the full solution. Depending on the complexity of the model, this can take anywhere from 15 minutes to days to run. For this analysis, due to its relative simplicity, the transient solution (300 seconds) takes 2-3 hours. Figure 22 shows these results for the resulting fluid temperatures which vary from 417oC to 20oC. These temperatures are actually relatively close to what is seen in Figure 16 and in the experimental testing of the next chapter.

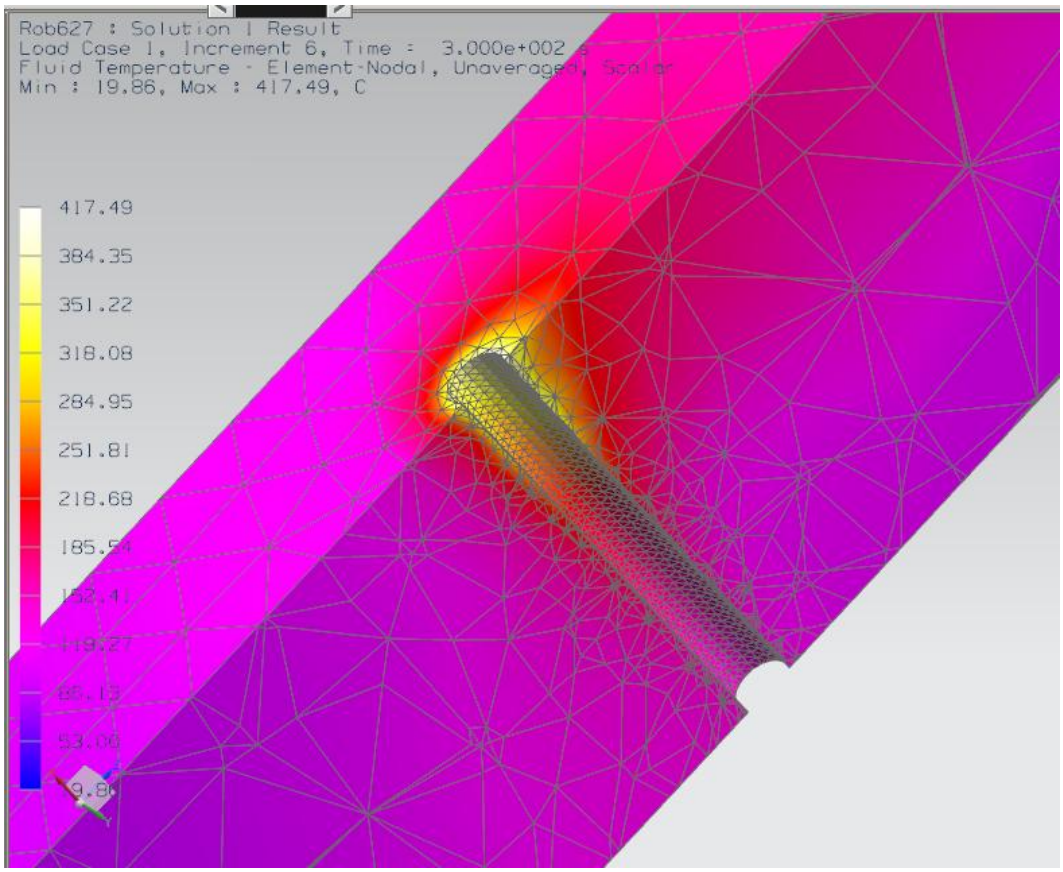

Figure 22. Temperature solution for the part modeled in this research.

Velocities are also important in this analysis. The Z-direction (axially with gravity) are shown in Figure 23. Since the model calculates them from buoyancy forces, large velocities indicate high temperature gradients and heat transfer rates. In Figure 23 we can see that above the highest heat flux portion of the sample (the side where light is incident) there are large positive velocities - up to 5mm per second. This is slow enough to still be in the laminar regime, but pretty high shear rates are present since on the right side of Figure 23 the fluid is falling back down at almost the same rate. This indicates that cooler surrounding fluid from above (and below) is being drawn towards the hot region. This is logical, and this type of motion is seen in videos taken during the experiments.

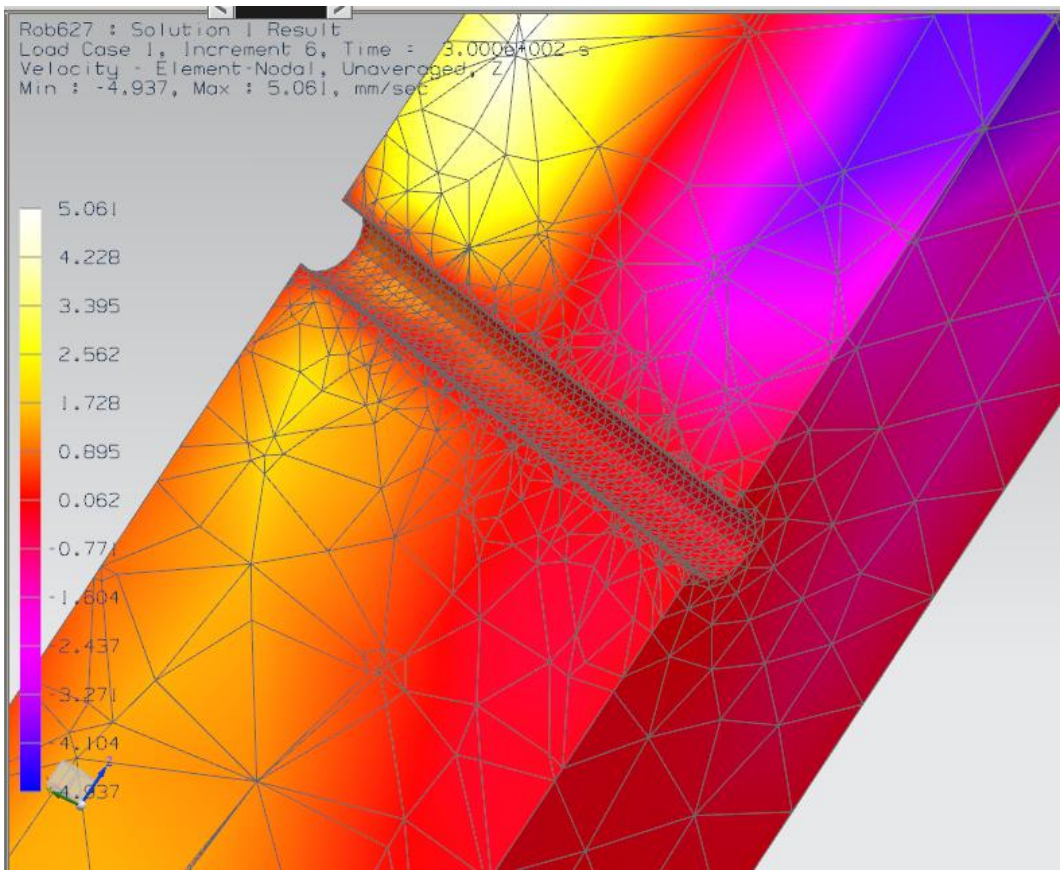

Figure 23. Z-Direction modeled velocity field (zoomed-in view).

As mentioned above, it is very important to achieve good converged solution. For this simple geometry this is not hard to reach as is indicated in Figure 24 which shows residuals on the order of 10^{-10}.

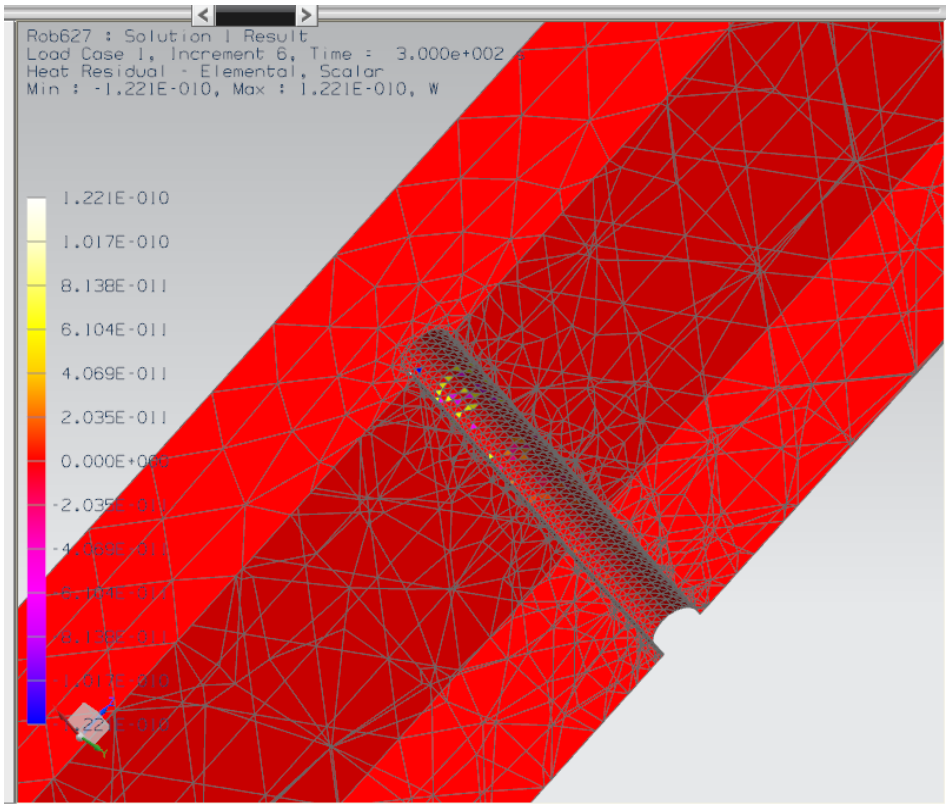

Figure 24. Sample residuals of the energy equation for this modeling simulation

According to all the modeling results, we expect to see relatively high temperatures and velocities near the heated region of these highly-absorbing samples when exposed to high intensity light. In addition, the modeling results indicate that we should see significant differences between volumetrically absorbing fluids and surface based photothermal conversion of energy. To discuss this in more detail, these simulation results will be compared against the experimental results which are presented in the next chapter.

CHAPTER 4: NANOFLUID LAB EXPERIMENTATION

This chapter will discuss laboratory testing conducted during this research effort. This experimentation can be roughly broken down into three basic categories: 1) nanofluid characterization and property measurements, 2) hot-wire boiling experiments, and 3) laser-induced boiling. In each of these cases, the results will be compared to the pure base-fluid and other 'baseline' fluids including black dyes, surfactant mixtures, and India ink.

4.1. Nanofluid Preparation Method

Creating a stable nanofluid is a must for any real application and for measuring optical properties. Without careful preparation, nanoparticles will agglomerate and settle out of the base fluid in a very short time. Although there are many methods of nanofluid preparation, they can be roughly categorized into one-step and two-step processes. One-step processes synthesize the nanofluid to the desired volume fraction and particle size inside the base fluid. Thus, the final product is a specific nanofluid which is ready for use (possibly after dilution). The two-step method is accomplished by first synthesizing the dry nanoparticles to a preferred size and shape. In the second step, these particles are carefully mixed into the desired base fluid at the desired volume fraction, usually with some additives for stability.

Several researchers have had success fabricating and testing nanofluids using these preparation methods (Chang & Chang, 2008; Eastman, S. et al., 2001; Hwang et al., 2008; Kumar, S.A., et al., 2009; Zhu et al., 2004). Based on these results, one-step methods may produce the best results if they can be scaled up and manufactured inexpensively. However, due to its straightforward nature and its controllability, we will only use the two-step method in this research.

A variety of dry powders are available 'off-the-shelf' (MTI, 2011; NanoAmor, 2010; Sigma-Aldrich, 2010). These particles are very versatile and can be mixed into many different liquids at the preferred concentration. Depending on the stability and quality required, this process can take anywhere from a few minutes to several hours. For the test fluids of this article, the particles and up to 1% sodium dodecyl sulfate (aka SDS, a surfactant) were dispersed into the base fluid using a sonicator - a UP200 from (Hielscher, 2011). From our experience, probe-type sonicators break particle agglomerates faster and much more thoroughly than bath-type sonicators. Since it is relatively quick, requires very little 'high tech' equipment, and produces any number of nanofluids, this process is our method of choice. Unfortunately, surfactant-stabilized nanofluids are known to break down at elevated temperature (Y. Jeong, W. Chang, & S. Chang, 2008). For longer-term stability in a solar application, one can re-sonicate continuously *or* attempt more exotic preparation methods - e.g. chemical surface treatment, pH control, optimum micelle additions, etc.

Our nanofluids were prepared by mixing the powder particles with de-ionized water and surfactant - added at up to 1% volume fraction to increase stability. Figure 25 shows some images of dry powder obtained from a transmission electron microscope at Arizona State University's LeRoy Eyring Center for Solid State Science. These images show that in powder form the particles are indeed very small and match well with the manufacture specified size (shown in the title boxes).

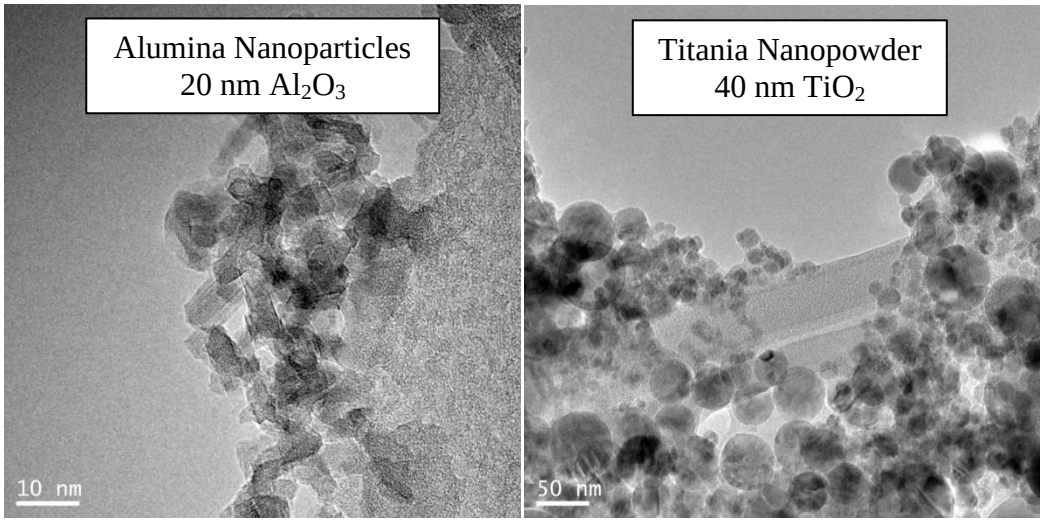

Figure 25. TEM images of dry nanoparticle powders

After combining the ingredients, the samples are then placed in an ultrasonic processor (Hielscher UP200S) for 20-30 minutes. We investigated volume fractions of 1% or less, since much of the literature found significant property changes in this range. In fact, in most cases volume fractions were lower than 0.1% because this is all that is necessary to obtain the optical

properties needed in these tests. As mentioned above, several researchers noticed that at more than 1% particle loading, a decrease in thermal properties is possible.

To test nanofluid stability and particle size in solution, a dynamic light scattering machine was used. In this machine a small, slightly turbid sample is exposed to a calibrated beam of light. A correlation analysis is run on the measured (scattered) signal which gives an indication of the particle size distribution. The equipment used to do these measurements was a Nicomp 380 Dynamic Light Scattering (DLS) instrument. The average aggregate size is found to be relatively consistent for our preparation method, at 150-160 nm with a standard deviation of about 70-75 nm. This indicates that agglomeration is somewhat insensitive to particle concentration and particle type. Figure 26 shows some characteristic DLS results of a variety of particle-laden mixtures. DLS testing also revealed that 24 hours later the samples heavily clumped into 10-15 μm aggregates, showing that these fluids are unstable on long time-scales. Further, if the sample was boiled and then sized 24 hours later, the average particle diameter was found to be 18-28 μm. Thus, the rate of agglomeration seems to be influenced by temperature as well as time. It should be noted that these results are given on a volume-weighted average, which yields particle sizes that lie between number and intensity-weighted averages.

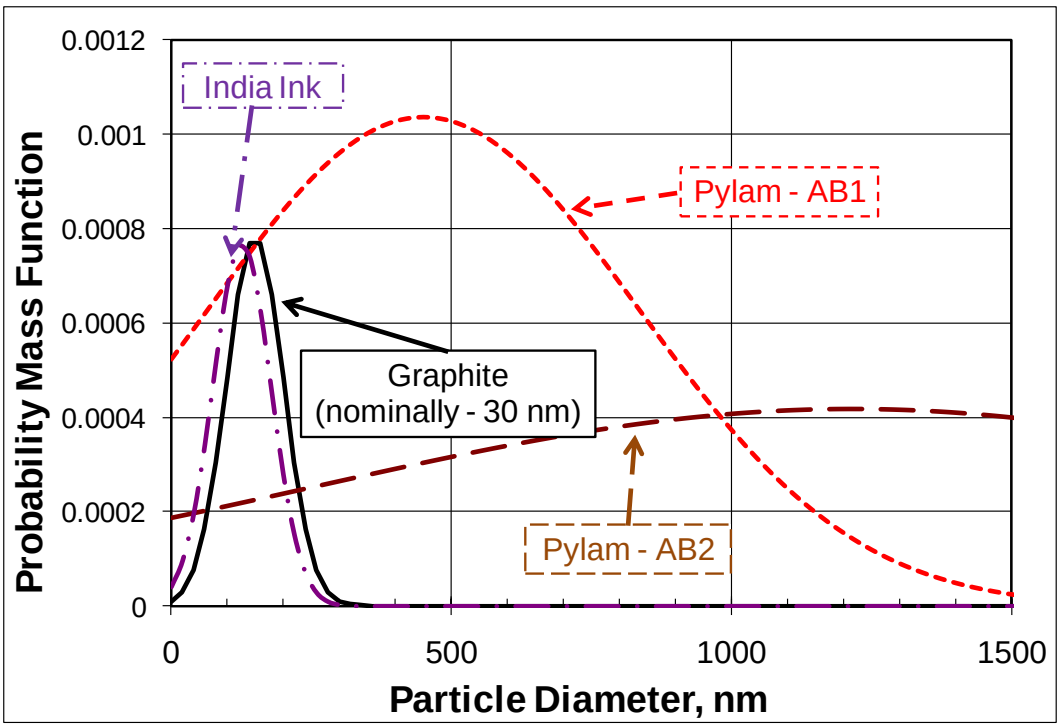

Figure 26. Dynamic light scattering results for freshly prepared nanoparticle mixtures (volume-weighted average)

4.2. Nanofluid Optical Property Measurement

All of the following experimental work deals with radiation in some form, but most of it investigates photothermal conversion. Consequently, for any well-characterized tests, we need to know the optical properties of these nanofluid. We are also very interested to see how well the Rayleigh scattering assumptions of the last chapter match with real fluids.

To measuring the optical properties we use a spectrophotometer. This is a device that sends a light beam of variable wavelength through a sample and then detects the transmitted beam. Spectrophotometers come in several configurations

and are good for a variety of wavelengths. For our purposes we need measurements over the solar spectrum, i.e. between 0.20-3 µm. As such, we mostly use a Jasco V-670 (Jasco, 2011), which can take transmission measurements in the range of 0.19-2.7 µm. It should be noted that other spectrophotometers with different ranges and specifications have also been used for comparison in our testing.

Regardless of the spectrophotometer used, some further calculations are necessary to obtain extinction coefficients for nanofluids. Since a cuvette contains the liquid sample in the system, resulting measurements actually take place in a three-slab system. This adds complexity since there can be multiple reflections at each element interface which needs to be accounted for in the measurements. Figure 27 shows the details of this multi-component system.

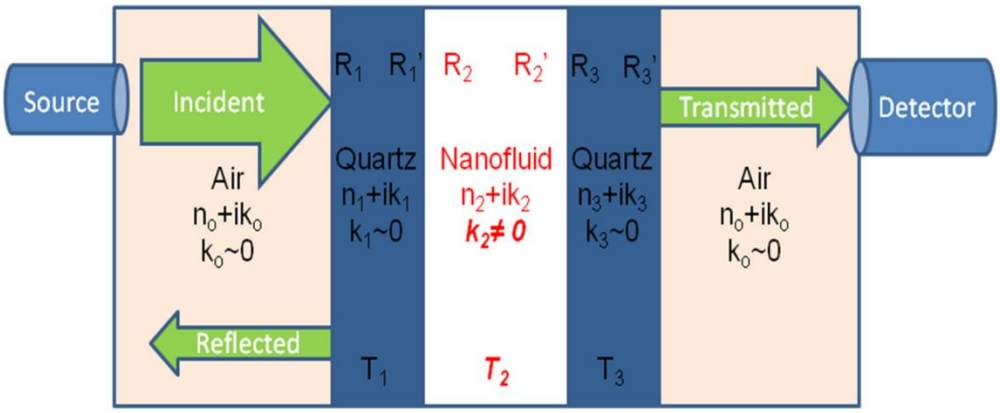

Figure 27. Diagram of a three-slab system representation of spectrometry measurements used with a quartz cuvette

In the figure n, k, $\Re$, and T represent the real part of the refractive index, the imaginary part of the refractive index, reflection at the interfaces, and transmission through each component, respectively. As can be seen in figure 21, some of the signal going through the three-slab system is lost to reflections at the interfaces. With known refractive indices of quartz and air, it is possible to determine the nanofluid optical properties. As a first step, we calculate values of reflection, $\Re$, and transmission T shown in Figure 27 in accordance with the approach of (Large, 1996):

$$\Re_i = \frac{(n_j - n_i)^2 + (k_j - k_i)^2}{(n_j + n_i)^2 + (k_j + k_i)^2} \tag{60}$$

$$T_i = \frac{(1 - \Re_i \Re'_i) e^{-4\pi k_i L_i / \lambda}}{1 - \Re_i \Re'_i e^{-8\pi k_i L_i / \lambda}} \tag{61}$$

The variables n_i and k_i in the previous equations represent the ith spectral real and imaginary components of the refractive index. Likewise, L represents the length of the ith element. To combine these equations for a two-element system the following equations can be used (Large, 1996):

$$\Re = \Re_1 + \frac{T_1^2 \Re_2}{1 - \Re_2 \Re'_1} \tag{62}$$

$$\Re' = \Re'_2 + \frac{T_2^2 \Re'_1}{1 - \Re_2 \Re'_1} \tag{63}$$

$$T = T_1 T_2 + \frac{\Re_1 \Re_2 T_1 T_2}{1 - \Re_2 \Re'_1} \tag{64}$$

Following the same process, a further combination for three elements can be done by using the following formula (Large, 1996):

$$\left[\Re_T \quad \Re'_T \quad T_T\right] = \left[\Re_1 \quad \Re'_1 \quad T_1\right] \oplus \left[\Re_2 \quad \Re'_2 \quad T_2\right] \oplus \left[\Re_3 \quad \Re'_3 \quad T_3\right] \tag{65}$$

With these defined, an iterative calculation of the complex index of refraction is possible. Using the imaginary part of the nanofluid index of refraction, k_{EXP}, a simple calculation can be performed to obtain the extinction coefficient, σ_{exp}. The following equation describes this final step (Modest, 2003):

$$\sigma_{EXP} \approx \frac{4\pi k_{EXP}}{\lambda} \tag{66}$$

Accordingly, σ_{EXP} should be directly comparable to the modeled quantity of last chapter, σ_{total}.

To compare the experimental approach and modeling approaches discussed above, Figure 28. Modeled and experimental extinction coefficients for several concentrations of aqueous graphite nanofluids. Note: Experimental results for pure water and water with 5 % surfactant are also plotted for comparison. Figure 22 also presents results for several concentrations of water-based graphite nanofluids - nominally 30 nm diameter, spherical particles. Note: The curve labeled 'Water_MOD' is essentially data from the reference book by (Palik, 1997). That is, equation 64 is used to manipulate reference text data from the complex refractive index, k_{EXP}, to the extinction coefficients shown in the plot. Also, experimental results for pure water and water with 5% surfactant are also plotted

for comparison. The high volume fraction surfactant was used to exaggerate the absorption of surfactant, which it turns out is very small. Experimental (labeled 'EXP') and modeling (labeled 'MOD') results are plotted together. Due to the large amount of data points the measured/experimental results are shown as lines while the modeling results are shown as marker curves.

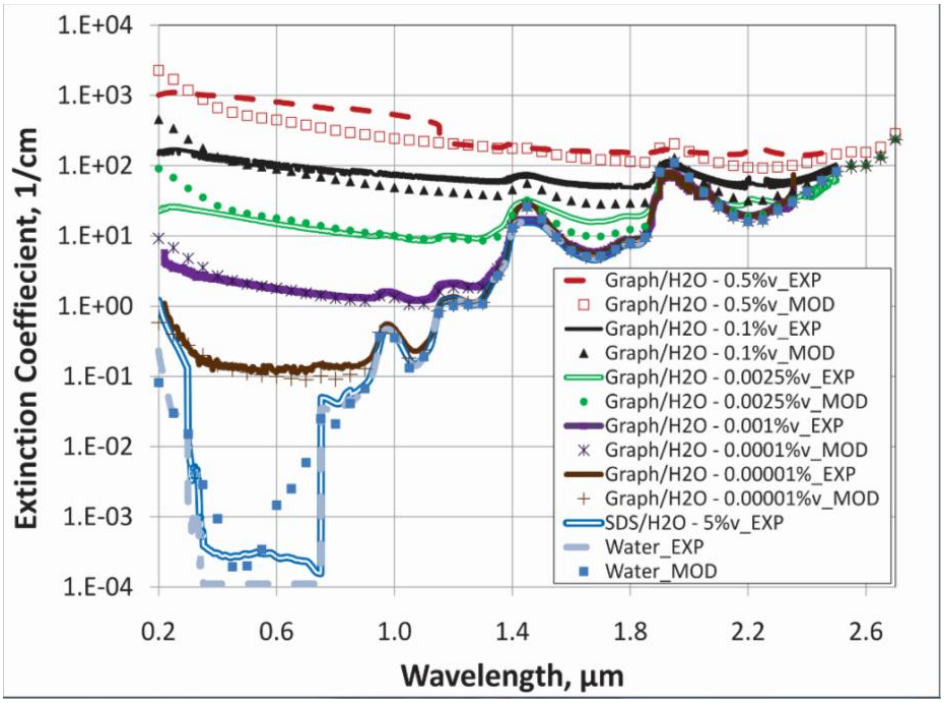

Figure 28. Modeled and experimental extinction coefficients for several concentrations of aqueous graphite nanofluids. Note: Experimental results for pure water and water with 5 % surfactant are also plotted for comparison.

The concentrations shown in Figure 28 represent a very wide range which could accommodate almost any solar receiver geometry. Overall, there is very good agreement between model and experimental results. Depending on volume fraction, the nanoparticles appear to be the absorbing material for shorter

wavelengths (up to ~ 1 μm for 1 x 10^{-5} %v and up to ~2 μm for 0.1 %v), whereas at longer wavelengths water becomes dominant and the curves coalesce. These results indicate that our Rayleigh approximation approach (from last chapter) agrees well with experimental data.

Conventional solar receivers have fluid depths on the order of 10 cm. Thus, a real nanofluid solar receiver would likely have a similar geometry. Figure 29 shows some characteristic results for several water-based nanofluids which were chosen to absorb >95% of incoming solar radiation over this fluid depth. Direct normal solar irradiance is also shown over the same wavelengths for comparison in Figure 29. Again, one can see the characteristic high extinction coefficients for the nanoparticles at short wavelength and that of water at longer wavelengths, ≥ 1.1 μm. For this fluid thickness the nanoparticles will be absorbing ~ 65-70% of the incoming solar energy, with the base fluid, water, absorbing ~30%.

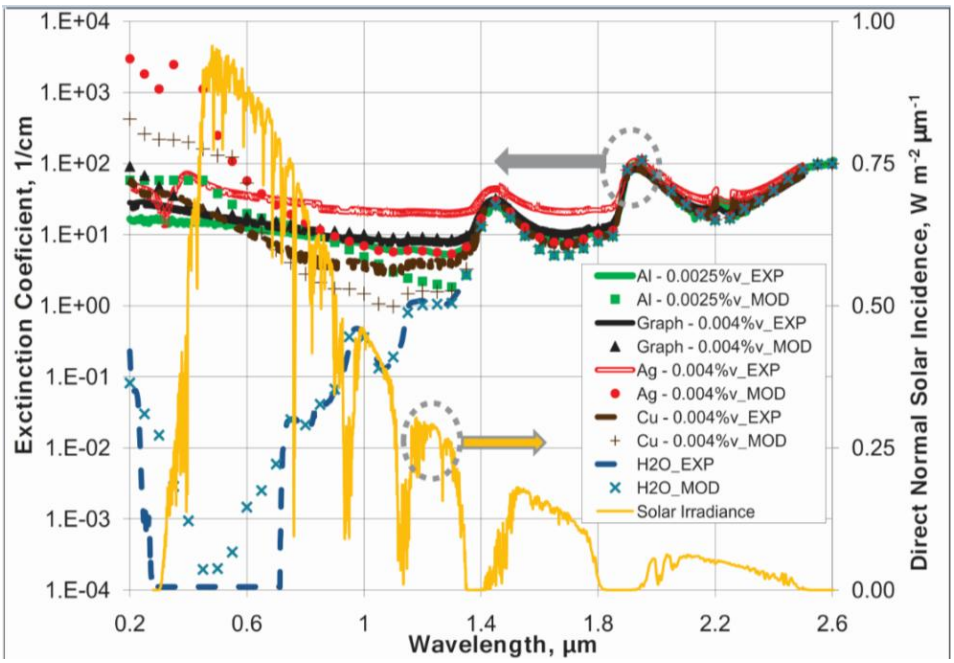

Figure 29. Extinction coefficients - measurements versus modeling for promising water-based 'solar nanofluids'

Figure 29 also shows less agreement between the model results and the experimental results for metals than was seen for graphite. Most noticeably in silver, we expected to see a large peak in the extinction coefficient. This peak, referred to as the plasmon peak, is a built-in natural frequency where electrons will absorb and oscillate strongly in a metal. It is usually found in the range of 300-500 nm for 30 nm particles (Zou, Janel, & Schatz, 2004). However, our experimental results for metal-based nanofluid were rather constant and did not show a large, pronounced plasmon peak as expected. In general, our model for metal nanofluids appears to over-predict from very short wavelengths until around 600-700 nm where it then begins to under-predict the extinction coefficient.

Figure 30 shows similar plots for various nanofluids which have Therminol VP-1 as a base fluid. Therminol VP-1 is a type of heat transfer fluid which is commonly used in many solar collectors. It is a colorless liquid which is only slightly more viscous than water and has a much higher boiling point, ~ 257^{o}C. This ability to work at higher temperature makes it good for medium-temperature solar collectors. It is composed of ~26.5% biphenyl and 73.5% diphenyl oxide. At present, there is very little information on the optical properties of these materials. Thus, the experimentally determined properties for the base fluid are used in the modeled extinction coefficients in Figure 30. Very similar trends are present to those seen in Figure 29, except that the absorption of the base fluid is less dominant at longer wavelengths.

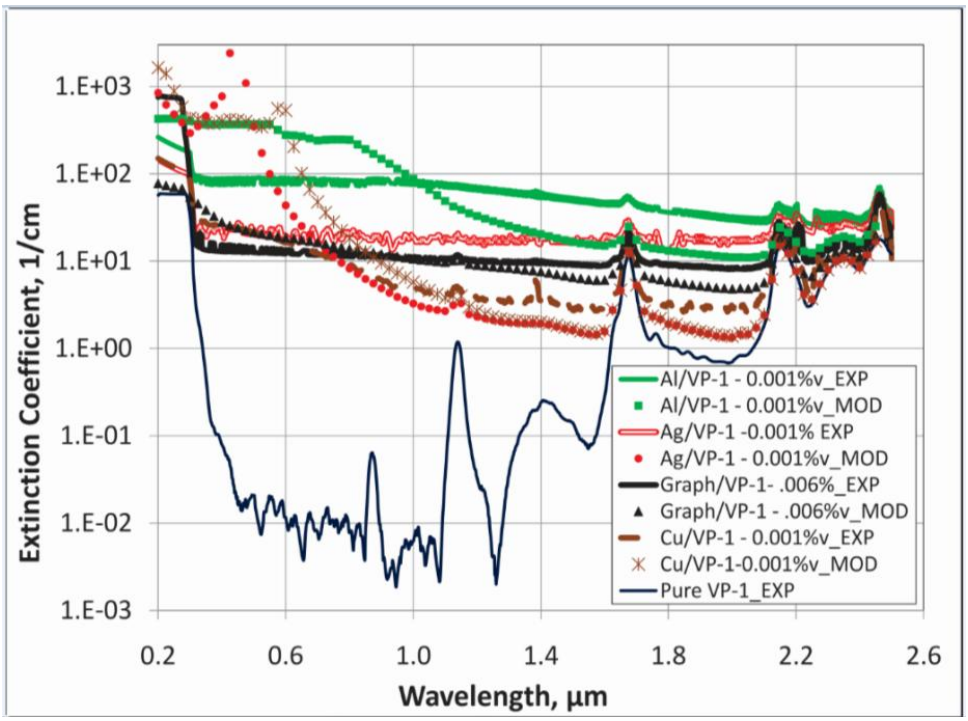

Figure 30. Extinction coefficients for Therminol VP-1-based 'solar nanofluids' - Note: Bottom curve shows experimental results for the pure base fluid, Therminol VP-1

The accuracy of this system is better than ± 0.3 %T. Thus, if we get a result of 90% transmission reading, it could actually be 89.7% or 90.3% transmission. However, the poor match in results in Figure 29 and Figure 30 cannot be explained by this error. One possible reason for the discrepancy, however, is that particle agglomerates are in the measurement beam path and absorb or scatter an anomalously large amount of light. That is, the real particle *shape* or *size* might deviate from the nominal manufacturer-stated nanoparticle specifications. Furthermore, the model assumes a monatomic particle distribution. That is, all the particles of a given sample are assumed to be the same size - thus, the average

particle diameter quoted by the manufacturer. Another possible explanation for the poor agreement is that an oxide layer or other chemical deviation may occur in the metal nanoparticles giving different properties than that assumed in the bulk metal.

To explore scattering and particle size, we can simply change these parameters in the model. This will at a minimum indicate the likelihood of these being the possible root of the problem. Since silver nanofluid shows the most deviation between model and experimental findings, we should look into the effect of varying particle size in silver nanofluids. Extinction coefficients of several 0.004% volume fraction silver nanofluids with a variety of nominal particle diameters are plotted in Figure 31. The experimental result for this volume fraction of particles with a manufacturer quoted average particle size of 40nm is also shown for comparison to the various model plots. Further, curves for σ_{total} and $\sigma_{particles}$ are plotted together to demonstrate the effect of absorption by the base fluid. This shows the importance of adding in the extinction of the base fluid into the total result. Overall, Figure 31 shows that size effects, while very important, do not seem to explain the difference between the rather flat trend of the experimental results and the large peak in the theoretical model.

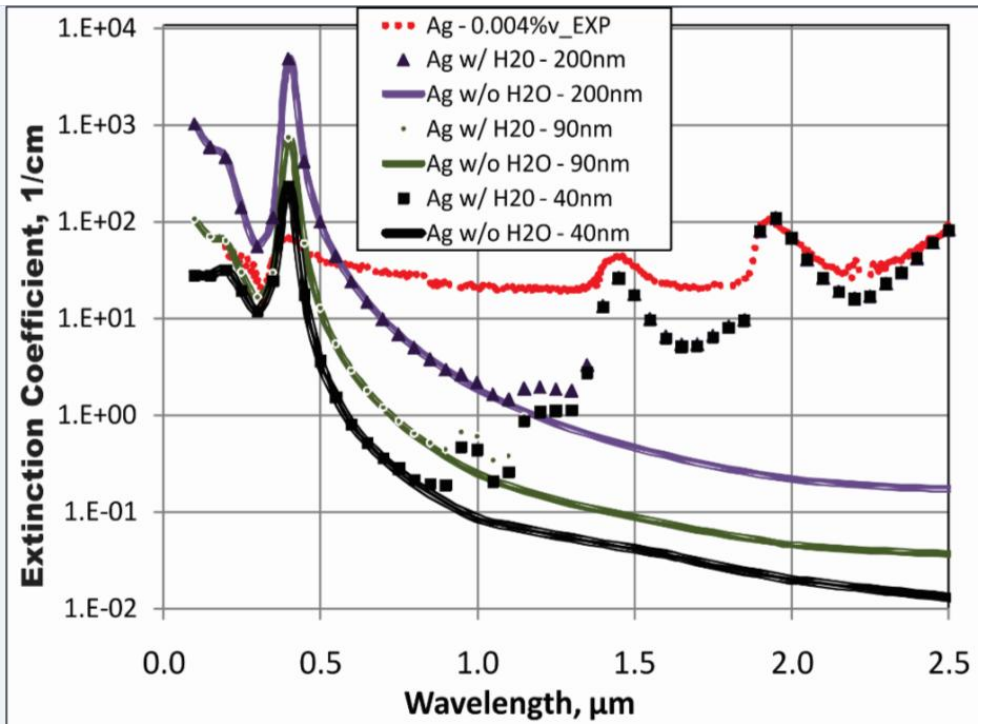

Figure 31. Extinction for different particle diameters and the absorption of water in a 0.004 %v silver nanofluid. Note: Experimental result for silver with manufacturer quoted 40 nm average particle size

As mentioned above scattering can also come into play, especially important at short wavelengths. Taking the results of Figure 31 and a nominal particle size of 100 nm, up to 5% of the incident light can be scattered in a solar nanofluid. In a 10 cm fluid depth this translates to an average extinction coefficient of $0.05cm^{-1}$. Overall, these results show a measurable amount of light can be scattered if large particles or particle agglomerates are present. If the particle size is < 50 nm, however, scattering is negligible - so care must be taken to make sure that the particles in a nanofluid stay 'nano'.

In order to investigate this assumption, however, we tested various optical depth 'nanosolids' (i.e. silver nanoparticles set in polydimethylsiloxane - also known as PDMS). The 'nanosolids' were chosen to control particle migration and ensure agglomeration does not occur over time. Thus, PDMS/nanoparticle composites are considered to be a snapshot of a nanofluid sample.

These samples were placed in the path of a green, 532nm, laser beam. A target was placed approximately 1m from the back of the sample. After the beam passed through the sample it was scattered and diverged. The resulting beam diameter was measured on the target and compared to the unimpeded beam diameter. The angle of divergence can be computed from these diameters and the known distance between the sample and the target. (Note: since the distance between the sample and the target is much larger than the sample thickness, the angle calculation is independent of where scattering starts inside the sample). During the experiment light energy in and the light energy transmitted were measured by a laser power meter (a Coherent Field-Max II with 0.1% accuracy). Figure 32 plots the angle of scattering as a function of the optical depth of the sample (as calculated by the power meter).

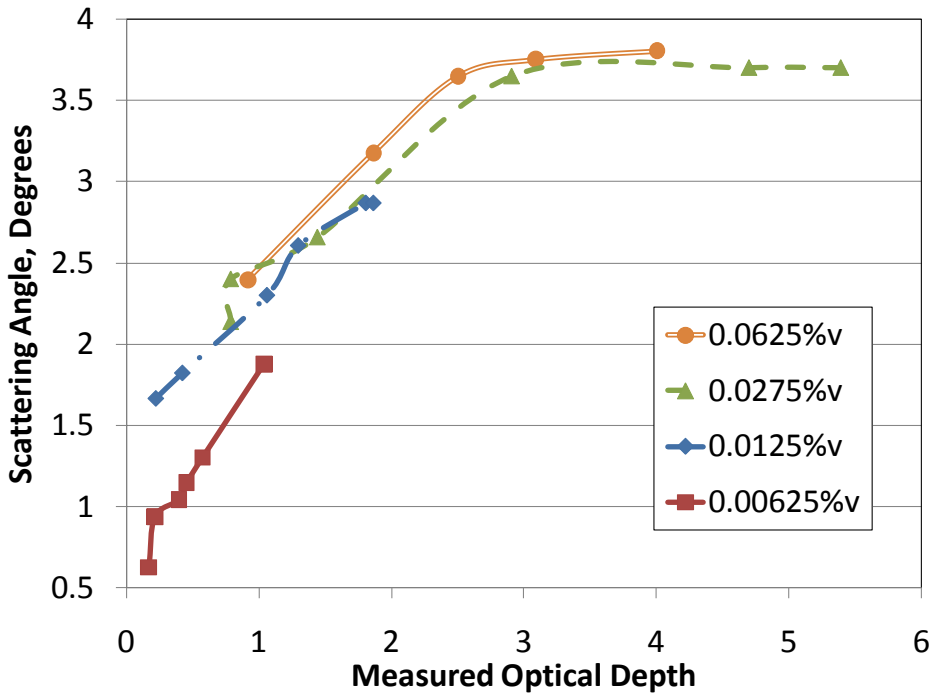

Figure 32. Scattering angle as a function of optical depth - silver nanoparticles dispersed in PDMS.

Figure 32 shows a range where the scattering angle increases linearly with optical depth. The slope of this regions for these curves is about 0.8. Since optical depth is directly related to the amount of particles encountered by the incident beam, we should see a linear increase in the amount of scattered light.

Without error and if the samples were oriented exactly normal to the incident beam, the curves in Figure 32 would line up for independent scattering. This seems to be approximately the case for the three upper curves. However, the low concentration sample, 0.00625%v, appears to have a different slope at low optical depths. The leveling off seen in the upper curves is due to high levels of

absorption where not enough light is transmitted to be accurately measured. In other words, if light is scattered in a medium which is *very* dense and absorbing it will not emerge. Thus, saturation occurred and the linear trend breaks down. Overall, these results show that a measurable amount of light can be scattered. Taking the results of Figure 32 and a nominal particle size of 100nm, up to 5% of the incident light can be scattered in a solar nanofluid. If the particle size is < 50nm, however, scattering is negligible - so care must be taken to make sure that the particles in a nanofluid stay as small.

The experimental results did not match well with the model predictions for some metals tested, particularly those with large predicted plasmon peaks (e.g. silver). Particle size was discredited as the root of poor model predictions for metals. Scattering is expected to be negligible if care is taken to keep particles in solution near their manufacturer-listed diameters - so this is also unlikely to lead to significant errors. One possible explanation is the purity of the materials. For instance oxidization or other impurities on the particle surface might be responsible for the poor agreement with the model.

Overall, these optical property experiments have shown that laboratory test data and modeling techniques ***are*** in very good agreement for graphite nanofluids. They also correspond well in the case of aluminum. This is fortuitous because these materials are the most likely choice for applications due to their low cost.

Now that we have some confidence in our model (for these materials), we can move on to other experiments - namely boiling experiments. The next section, 4.3, will describe the fundamental difference in boiling between nanofluids and their base fluids. It is important to understand these subtle differences before moving on to volumetric, light-induced boiling in section 4.4.

4.3 Hot Wire -Induced Boiling

In order to quantify the effect of nanoparticles on boiling incipience and nucleate boiling, nanofluids were prepared using Al_2O_3 nanoparticles and water. The method of preparation is described in section 4.1. Alumina was chosen because it is the most widely used material in pool boiling literature and it is of low cost. Al_2O_3 nanoparticles with a reported nominal average diameter of 20nm were purchased from NanoAmor. The hot-wire method was used to conduct a simple pool boiling experiment. Figure 33 shows a schematic of the boiling test cell. Current from a (BK Precision 1621A) DC power supply is passed through a known resistor ($0.1\Omega \pm 1\%$ - from Mouser Electronics) and then through the heater wire (294R – donated by MWS Industries) back to the power supply. The voltage is measured over both of the resistors with a (Keithley 2001) multi-meter.

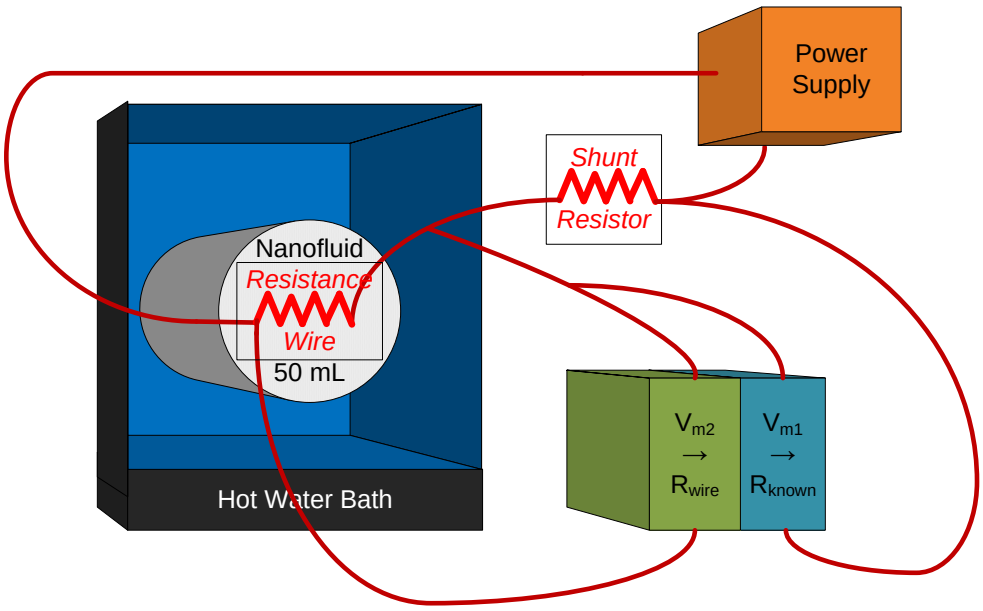

Figure 33. Boiling cell diagram for the experiment – the test section is kept at saturated conditions using a hot water bath (VWR - Model 1209)

The heating wire is submerged in a 50 ml beaker containing the test nanofluid. The beaker is surrounded by an isothermal water bath (VWR 1209) which is held constant at ~100^{o}C. Unfortunately, due to heat transfer losses it was difficult to maintain 100^{o}C in the nanofluid at the beginning of testing. This was assumed to be acceptable since standard texts on pool boiling (such as (Carey, 2007)) state that a small amount of sub-cooling should not influence the boiling curve significantly – especially at higher heat fluxes.

The wire is composed of 29% Ni, 17% Co, and 54% Fe. This wire was chosen because it had more than an order-of-magnitude higher temperature coefficient of resistance (3.3 x 10^{-3} $\Omega/^{o}$C) as compared to conventional NiCr wire

(1.03 x 10^{-4} Ω/^{o}C). The wire used in this study had a diameter of ~0.255 mm and a length of ~ 5cm. A fresh wire was used for each test.

A standard thermometer (-20 to 150^{o}C range) is placed in the beaker to measure the bulk fluid temperature. The power supply is run under current-controlled conditions with discrete increases of 0.25 Amps every 2-3 minutes from 0 to 5 Amps (the upper limit of the power supply). This is done slowly in order to try to realize near steady-state conditions at each step. The voltage over our known resistor is measured to determine the current in the system. The wire temperature can then be back-calculated using the following equations:

$$\frac{V_{m1}}{R_{known}} = I_{PS} \tag{67}$$

$$\frac{V_{m2}}{I_{PS}} = R_w \tag{68}$$

$$\frac{R_w}{R_{ref.}} = 1 + \alpha\left(T - T_{ref}\right) \tag{69}$$

where V_{m1}, R_{known}, and I_{PS} are voltage across the shunt resistor, shunt resistance, and current in the system, V_{m2} and R_w are voltage drop across the hot wire and wire resistance, and $R_{ref.}$, T_{ref}, α, T are the reference resistance and temperature, thermal coefficient of resistance, and wire temperature, respectively.

In equation (67), α is the temperature coefficient of resistance mentioned above. In order to plot the boiling curve, the heat flux is also needed. This is found by the following equation:

$$q'' = \frac{I_{PS} V_{m2}}{\pi D l} \quad (70)$$

where *q''*, *D*, and *l* are the heat flux, wire diameter, and wire length, respectively. An error propagation analysis gives 2-3^{o}C error in the calculated temperature and 3-5% error in the calculated heat flux for this set-up. Sample uncertainties are shown in the following figures.

The experiments covered a wide range of phenomena: boiling incipience, nucleate boiling, sub-cooled boiling, and critical heat flux (CHF). CHF, however, is not presented due to limited data. Scanning electron microscopy (SEM) / X-ray dispersive scattering (XDS) analyses were performed - before and after heating - to investigate particle deposition.

4.3.1 Boiling Incipience

In pool boiling tests, the first point of interest is boiling incipience. This point marks the transition from the natural convection to the nucleate boiling regime. It can be noticed by a change in slope on a heat flux versus superheat curve. Figure 34 shows the experimental results for nanofluids as compared to

pure de-ionized water. A trend is indicated, in that boiling incipience occurs at lower superheat temperatures for the nanofluids compared to that for pure water. Furthermore, less superheat is required to initiate boiling with increasing nanoparticle volume fraction. This finding is presumably related to the deposition of nanoparticles on the heater surface, with the deposition density increasing with increasing nanoparticle volume fraction. An examination of the heater wire surface is described below.

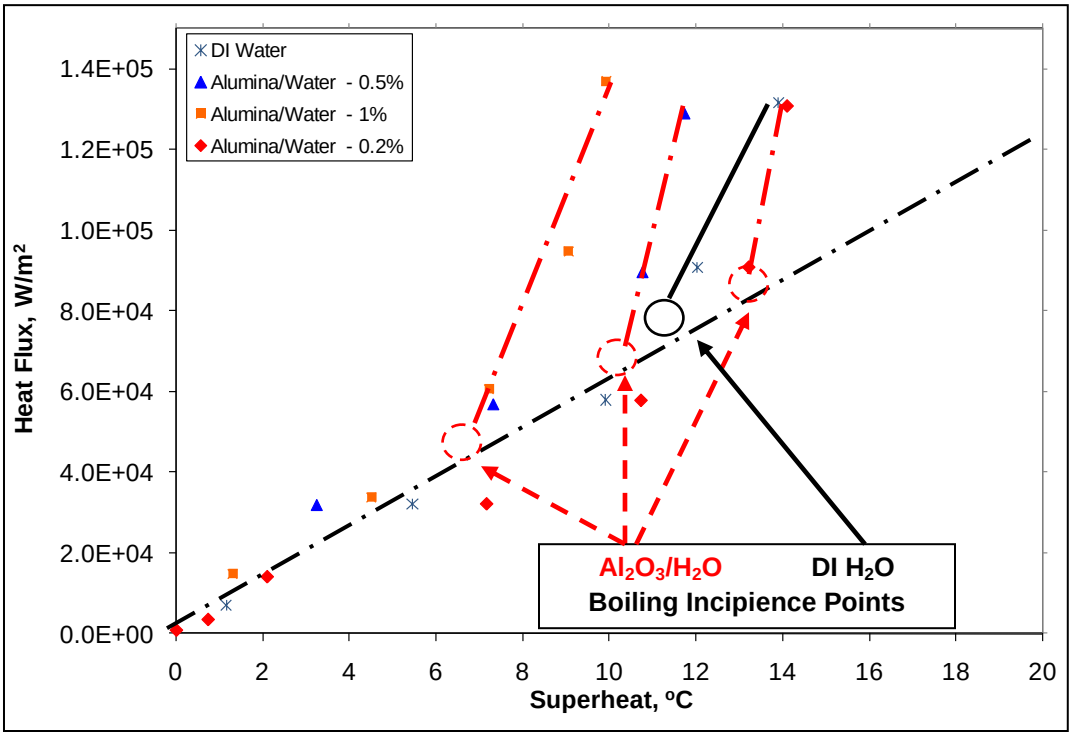

Figure 34. Experimental results, from the current study, for Al_2O_3/H_2O nanofluids and DI water (circles and lines highlight changes in slope for these data)

4.3.2 Sub-cooled Boiling

The higher slope region to the right in Figure 35 is referred to as the nucleate boiling regime. It is this part of the curve where researchers look for significant changes in the heat transfer rate since this is the operating range for many phase change applications. Our results show significant enhancement, 25-40% over that for pure water, for the higher nanoparticle loadings. Figure 35 shows little enhancement for the 0.2% Al_2O_3 concentration, but a considerable shift to the left (i.e., enhancement) for the 0.5% and 1% concentrations. Thus, less of a temperature difference between the wire and the surrounding bulk fluid is necessary to dissipate the input heat flux for the higher concentrations.

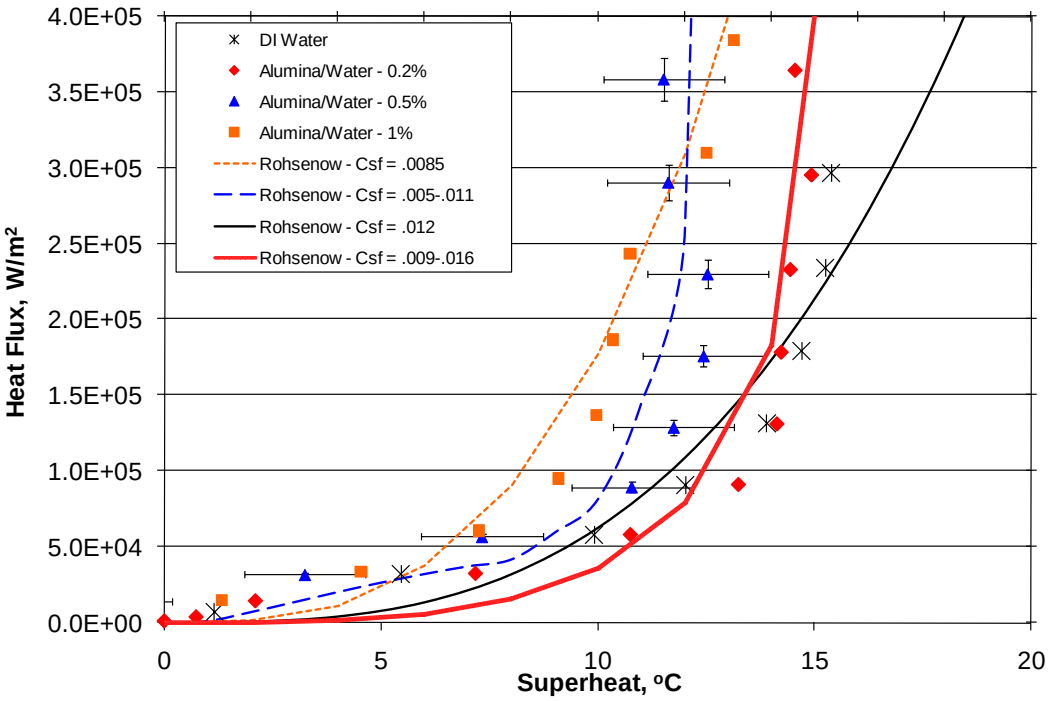

Figure 35. Experimental results, from the current study, for Al_2O_3/H_2O nanofluids and Rohsenow's model.

Also, curves of Rohsenow's (Rosenhow, 1952) model with variable C_{sf} are plotted against these data. As mentioned above, a changing C_{sf} is justifiable since nanoparticles interact with the heated surface increasingly during the test. Using this approach, the correlation fits most data points.

The bulk temperature of the test fluid starts at 95-99^{o}C. Thus, the first few data points in each test do not line up perfectly with Rohsenow's model. As noted above, according to conventional reasoning, a small amount of sub-cooling should have limited influence and will diminish at higher heat fluxes (Carey, 2007).

Figure 36 presents the same data from this study, but also provides a direct comparison to the alumina nanofluid data found in the literature. It can be seen that the 0.5% and 1% data curves fall towards the left half of the literature data. This makes sense because only a portion of the literature demonstrated enhancement. Note that the present results, in general, extend to higher values of heat flux than do most of the existing data in the literature.

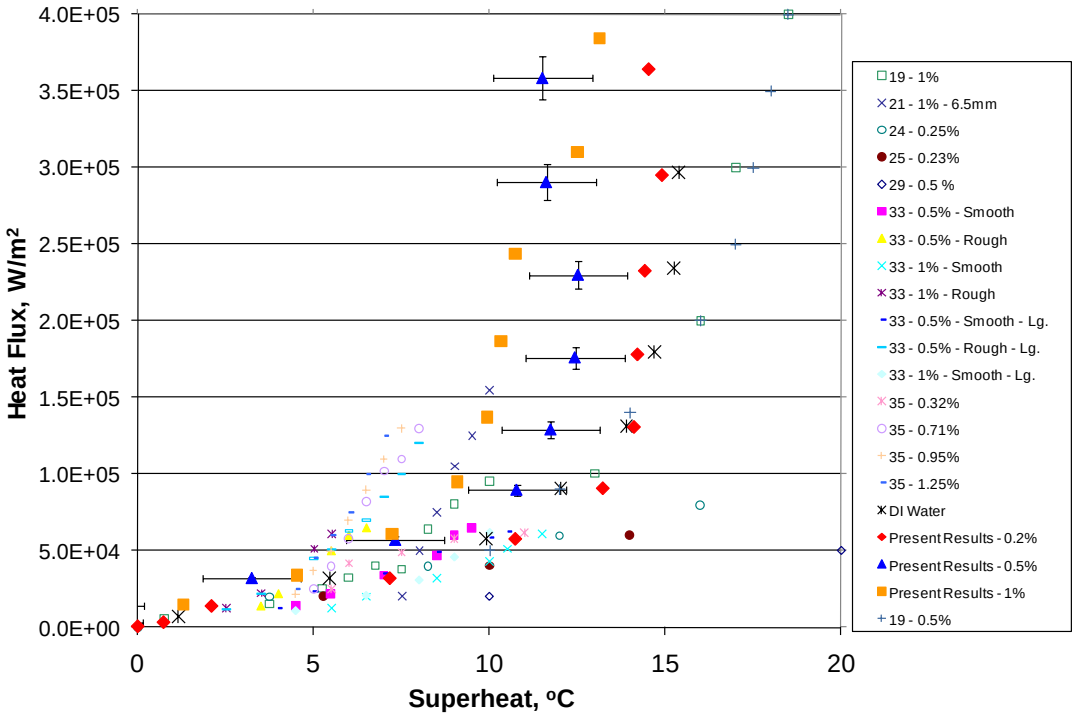

Figure 36. Present nanofluid experimental results plotted against comparable alumina nanofluid pool boiling data from the literature - references indicated in the legend.

4.3.3 Saturated Nucleate Boiling

Since the isothermal bath used in this study had difficulty reaching 100°C, a few tests were conducted at lower bulk fluid temperatures – that is, sub-cooled pool boiling. Out of the surveyed pool boiling literature, only two articles examined the effect of sub-cooling on nanofluid boiling (Z. Liu et al., 2007), (D. Zhou, 2004). Li et al. studied bubble interactions in sub-cooled nanofluid boiling and noticed that bubbles were more likely to cluster and/or overlap (Z. Liu et al., 2007). Unfortunately, Li et al. did not generate boiling curves for comparison. Zhou concluded that the addition of nanoparticles does not change

sub-cooled boiling (D. Zhou, 2004). Zhou also used Cu/Acetone nanofluids which are not comparable to this work (D. Zhou, 2004).

Figure 37 shows boiling heat transfer is actually degraded during sub-cooled boiling of nanofluids, for this study. This was not expected since sub-cooling was assumed to have little impact on the boiling characteristics. A possible reason for this result is that when the fluid is sub-cooled, nanoparticles may be less likely to deposit on, and subsequently change, the boiling surface. This hypothesis is supported by the first few (slightly sub-cooled) data points in Figure 34 which show that the nanofluids initially decrease heat transfer. Further, little particle deposition was seen in samples that were not taken above the boiling incipience point. Since bubbles are not seen until higher heat fluxes, sub-cooled boiling essentially extends the natural convection regime to higher heat fluxes.

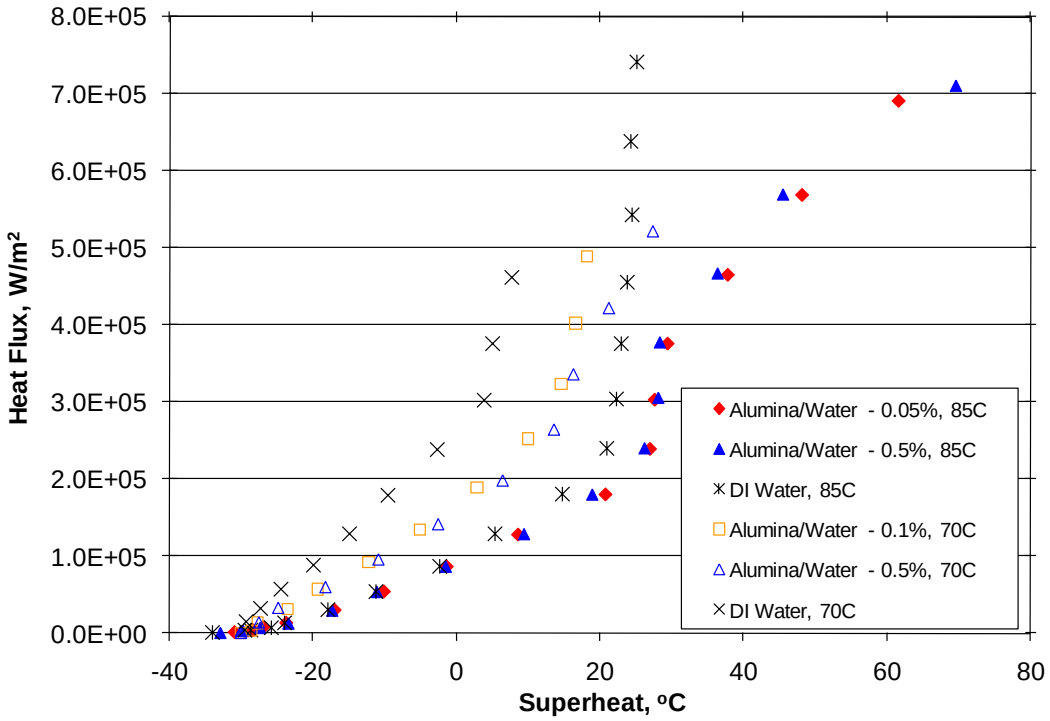

Figure 37. Sub-cooled pool boiling tests from this study, for Al_2O_3/water nanofluids. The temperatures in the legend are the initial solution temperatures.

One rationalization for degraded sub-cooled boiling in this study is that nanoparticle deposition may *only* occur during nucleate boiling. This could be explained by a high temperature gradient between the wire and the *liquid* fluid. Thermophoretic motion is expected to be important in nanofluids as it is dependent on the temperature gradient (S. Kim, I. Bang, J Buongiorno, & L. Hu, 2007). Thermophoresis would cause particles to migrate away from the high temperature wire.

4.3.4 Critical Heat Flux

Another important part of pool boiling is the CHF. All of the pool boiling literature that studied CHF showed an increase with the addition of nanofluids – from 30 to 300% (I. C. Bang & S. H. Chang, 2005; Coursey & Jungho Kim, 2008; Sarit Kumar Das et al., 2006; Gerardi, Jacopo Buongiorno, L.-wen Hu, & McKrell, 2011; Jackson, 2007; D. K. Kim & M. H. Kim, 2007; H. Kim, J Kim, & M. Kim, 2007; H. D. Kim & M. H. Kim, 2007; J.H. Kim & K. H. Kim, 2004; S. Kim et al., 2007; Milanova & R. Kumar, 2005; D Wen, 2008; S M You & J H Kim, 2003; S. M. You, J. H. Kim, & K. H. Kim, 2003; S. M. U. N. You, Bar-cohen, & Simon, 1990). CHF marks the point where a vapor blanket forms on the heated surface, causing a sharp increase in temperature for little additional increase in heat flux. In the hot wire method, the wire will glow and/or burnout. The above works agree (for the most part) that nanoparticles modify the heater surface to either help keep it exposed to liquid or increase the heat transfer from the surface. These mechanisms allow a nanofluid to delay the onset of burnout.

Although this study was not designed to characterize CHF, a few of the experimental tests done for this research were extended until the wire actually burned out. These tests revealed a marginal ~20% increase in CHF for 0.5% Al_2O_3 by volume. This is on the low side compared to the literature. It does, however, show that there are fundamental differences in boiling when

nanoparticles are involved. We believe that much of this comes from the fact that particles deposit on the surface as is discussed in the next section.

4.3.5 Analysis of the Heater Wire Surface

The last part of this study is dedicated to analyzing the wire surface. This is done by using a SEM fitted with XDS capabilities. Figure 38 shows a heater wire after boiling in a nanofluid. Notice that the coating crumbles off when it is dry. This indicates most of the coating is weakly bound. The large chunks in Figure 38 also illustrate that after boiling and drying the nanoparticles are highly agglomerated.

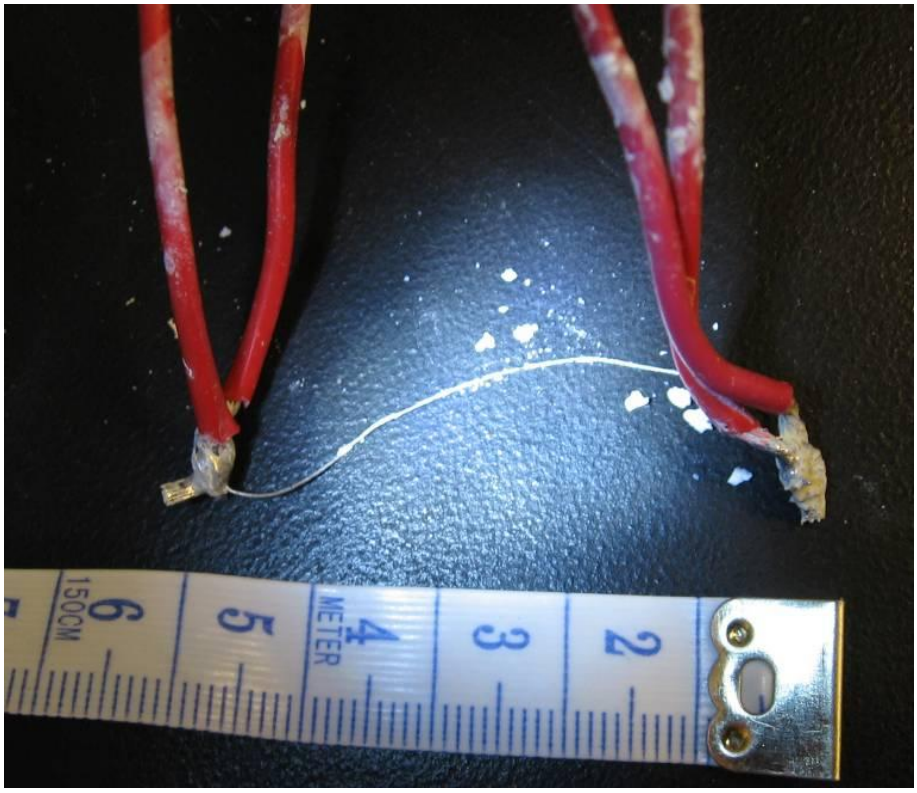

Figure 38. A dry sample of heater wire (MWS294R – 17% Co, 29% Ni, 44% Fe) after boiling

For surface analysis, the samples are lightly agitated in the nanofluid after boiling. This is done in order to remove the majority of the thick, loose coating. It is assumed that nanoparticles close to the surface would be most strongly bonded. The representative heater wires are then analyzed using the SEM/XDS machine. Figure 39 shows a comparison of two wires after boiling - DI H_2O (A) and 0.5% Al_2O_3/H_2O nanofluid (B). In Figure 39(B) some nanoparticles can be observed on the surface. This is confirmed by an Al peak in the XDS results. In both boiling cases there is a large oxygen peak. This peak was not seen in a

fresh wire, which indicates that boiling oxidizes the wire surface. Regrettably, due to the high iron (magnetic) content of the wire, clear SEM images were limited to a magnification of about 20,000X, or a 1-2 μm field of view. This is due to the fact that magnetic wires charge under high electron excitation, giving poor resolution.

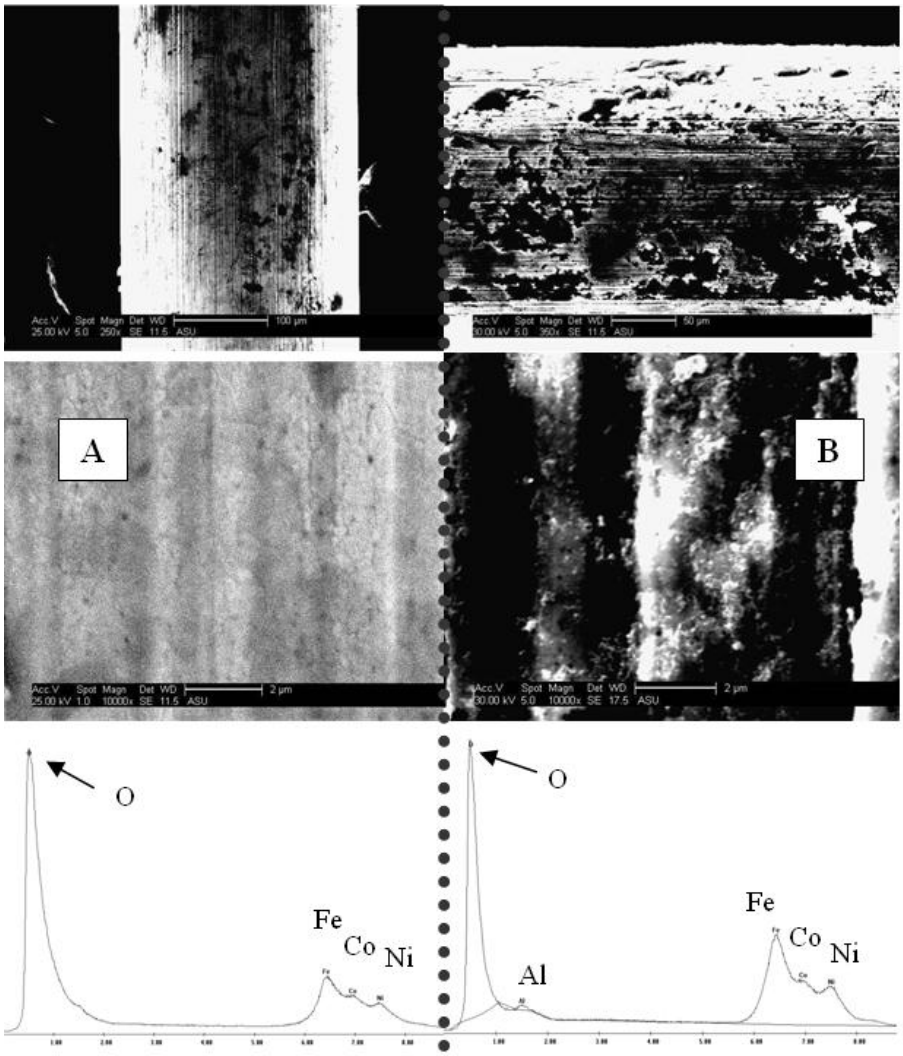

Figure 39. SEM / XDS analysis of heater wires: A) Boiled in H_2O B) Boiled in 0.5%v Al_2O_3/H_2O nanofluid.

SEM analysis also shows that surface defects (from extrusion) are approximately 1-2 μm wide. That is, the grooves running axially along the wire are approximately 10 times wider than the average particle diameter, or ~ 160 nm as measured by a dynamic light scattering system. This gives an estimated surface-interaction parameter as discussed in (Narayan et al., 2007) of ~ 10. If the width of these grooves is roughly equivalent to their depth, then nanoparticle deposition would cause an increase in nucleation site density and lead to a more active boiling surface. In other words, nanoparticles smaller than the existing surface roughness could make the surface rougher - on the nano-scale - which would theoretically enhance nucleate boiling heat transfer. Many of the studies reviewed for this paper also suggest that nanofluids cause a significant change in surface roughness which can considerably shift the boiling (S. Kim et al., 2007; Vassallo, 2004; Witharana, 2003). Unfortunately, wires in this study were too small (with too high a curvature) to take direct surface roughness measurements.

4.4. Laser -Induced Boiling

Nanoparticles have the ability to modify solid surfaces by deposition. It seems that this ability, if designed properly, can lead to slightly better boiling performance and a significantly higher critical heat flux. Since the goal of this research is to employ nanofluids as solar thermal collectors, we are also interested

in how boiling / phase change happens if the thermal input is light. For a real solar collector, the particles *and* the base fluid must be chosen carefully to get a nanofluid which is highly absorptive over the solar spectrum and cost effective - as was seen in chapter 3. Recall: Common solar base liquids are water, oils, and molten salt. For this study we will only use *water* since we want to generate steam directly in the receiver and because it is cheap and has good thermal properties.

Overall, this section will explore the following questions: How do black dyes, black painted surfaces, and nanofluids compare as direct steam generators? For the same photothermal input, what temperatures and vapor generation rates are seen for each scheme? What leads to these differences between them?

Keeping these questions in mind, the absorbing samples compared in this study are black backed surfaces, black dyes, and nanofluids – with de-ionized water as a base fluid in each. We expect each of these samples to convert light energy to heat in a localized region where the laser input hits the sample. This region is monitored simultaneously with a digital camera and an infrared camera. The resulting observed temperature profile and bubble dynamics are compared. Particular interest is placed on the difference between surface-based and volumetric-based nucleation and boiling.

4.4.1 Experimental Configuration

The experiment can be broken down into four basic components: the laser input system, the test cell, the testing fluid, and the monitoring cameras. In testing our samples we use two configurations - an axial and a perpendicular configuration. That is, our monitoring cameras can be oriented axially or perpendicular with respect to the laser beam. These two configurations are shown in Figure 40.

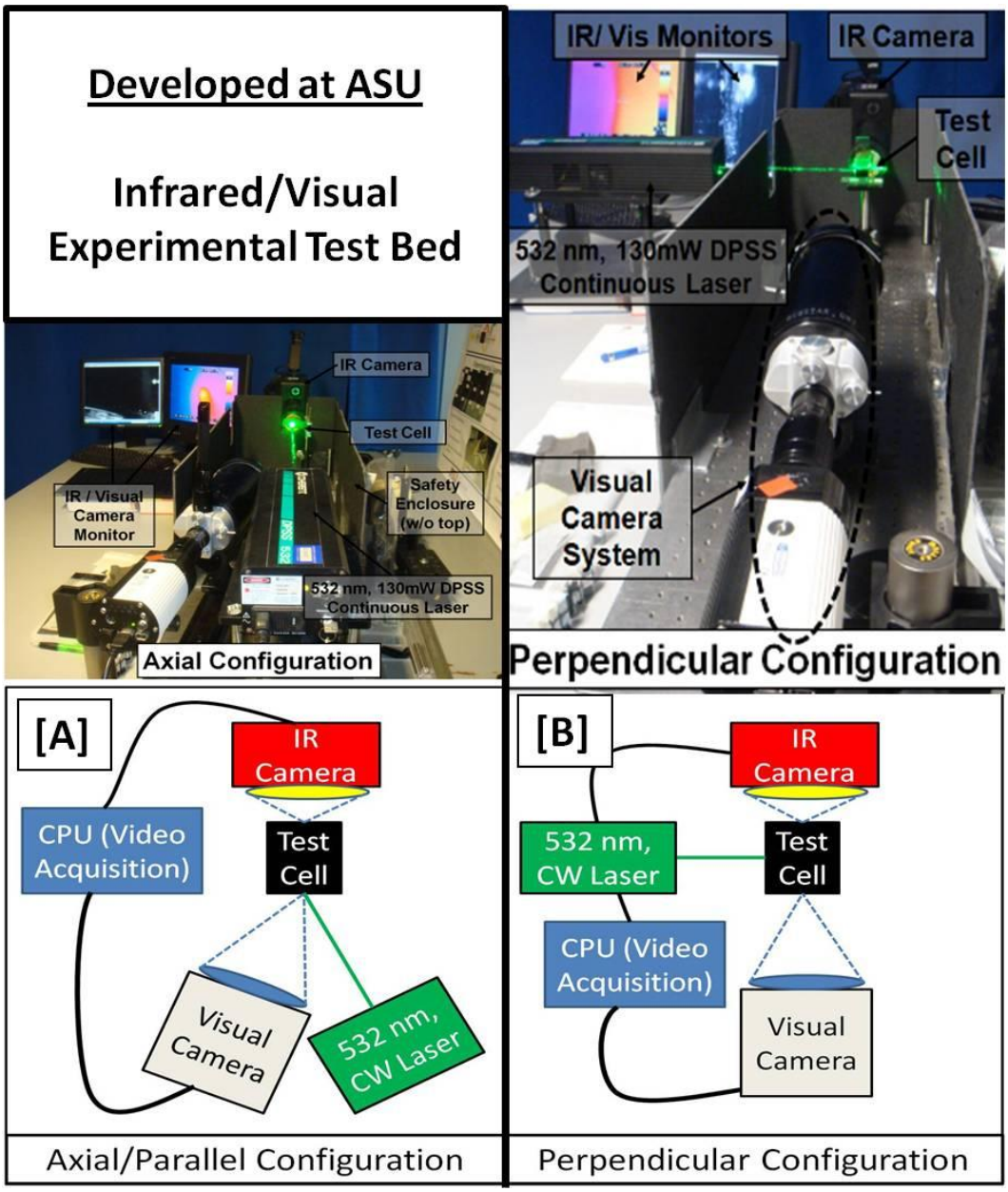

Figure 40. Experimental set-up in [A] the axial configuration and [B] the perpendicular configuration.

The input laser is a Coherent diode pumped solid state (DPSS), 532 nm (green), continuous laser. To achieve high enough irradiance the laser is focused

through a lens (with a 150 mm focal length). The extent to which a laser beam can be focused through this type of lens can be determined analytically. With some simplifications, the diameter of a Gaussian laser beam at its focal point can be approximated by (Hecht, 2001):

$$D_{waist} \approx \frac{4\lambda}{\pi}\left(\frac{f}{D_{initial}}\right) \quad (71)$$

where D_{waist} and $D_{initial}$ are the focused and unfocused beam diameters, respectively. Also, f and λ are the lens's focal length and the nominal laser wavelength, respectively. Through this calculation, we can find the beam waist (diameter) at the focal length of the beam to be 0.231 mm. Figure 41 gives a description of this process.

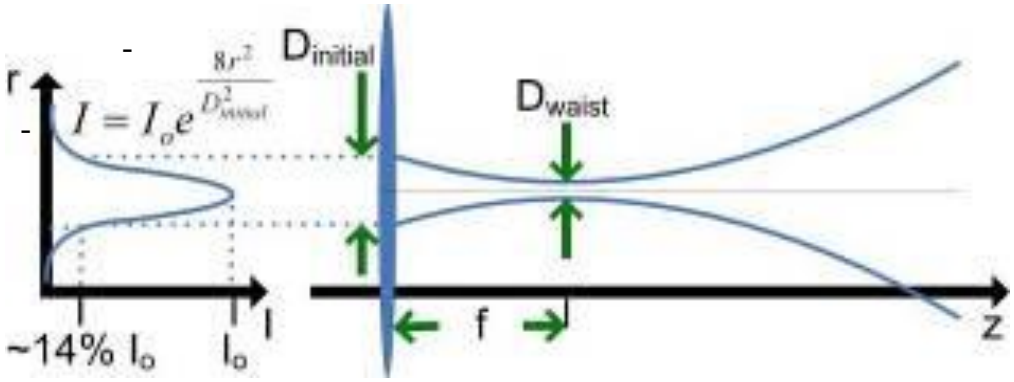

Figure 41. Parameters involved in Gaussian focusing a laser beam.

Diameters of the beams were also checked by exposing a piece of ZAP-IT™ burn paper to the focused and unfocused beams (Zap-It, 2011). Figure 42 shows

pictures of the unfocussed and focused beams, respectively, captured by a calibrated microscope.

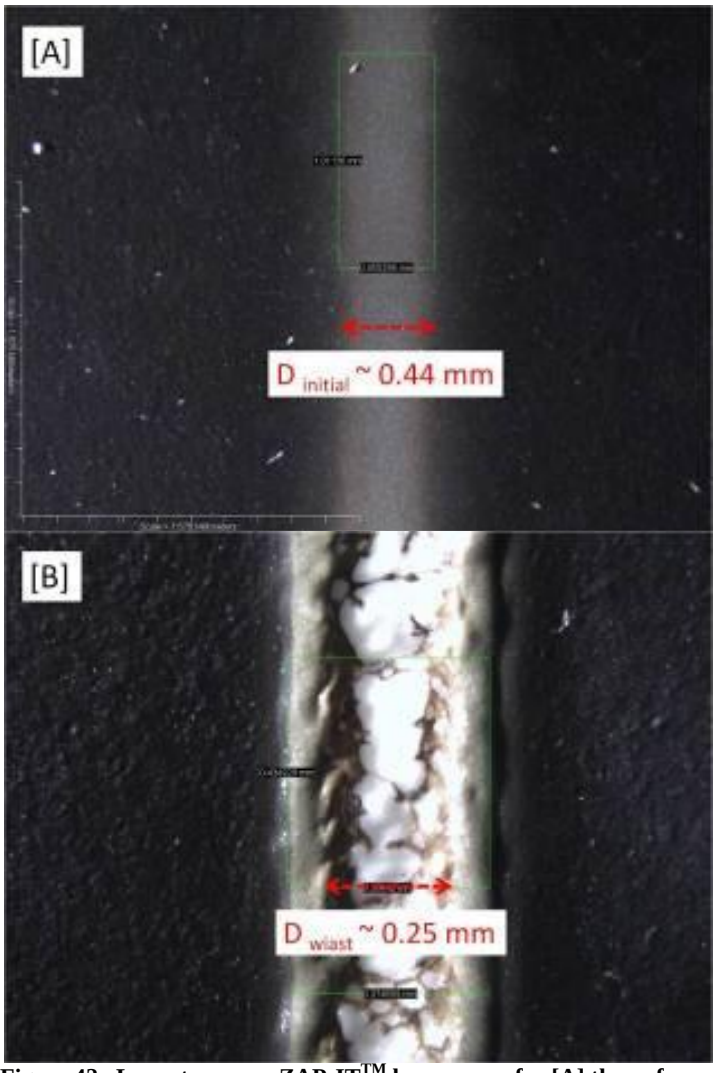

Figure 42. Laser traces on ZAP-IT™ burn paper for [A] the unfocused beam and [B] the focused beam.

Thus, in practice the focused beam diameter is very near its predicted value. To control input power further neutral density filters can be placed in the system

to block 10-100% of the beam. Thus, the input irradiance can be in the range of 0-77 W/cm^2. However, the results presented below will all be at full power.

4.4.2 The Photothermal Test Cell

Test cells were constructed from pieces of microscope slide glass. The basic goals of the test cell are to allow pictures to be taken with the monitoring cameras and to transmit the input laser for the two configurations. Thus, we want the test cell to be reasonably transparent on all sides. Also, we wish to expose a known thickness of test fluid to a controlled amount of light energy in the test cell. This is done by placing a combination microscope slides to obtain a controlled channel thickness. In the perpendicular configuration this is 1-2 mm. In the axial configuration we use 0.1 mm channel thickness. Note that the sample will be exposed to the entire laser for both configurations. Lastly, the cell needs to be made of a material which can be painted with our Thurmalox 250 selective black solar coating (for the black backing comparison). Thus, microscope slide glass is the best way to achieve a low cost, versatile test cell design. Figure 43 shows a picture of the test cell.

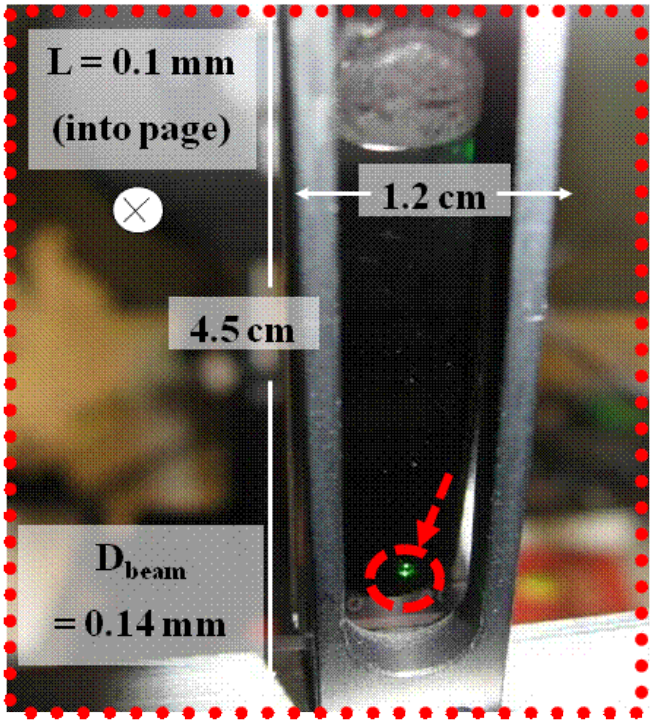

Figure 43. Test cell configuration

Another important consideration of the test cell is reflection. That is, how much of the laser light actually reaches the sample? This can be estimated with the following Fresnel equation - a simplified version of equation (58) (Hecht, 2001):

$$\Re = \frac{\left(n_{glass} - n_{air}\right)^2}{\left(n_{glass} + n_{air}\right)^2} \tag{72}$$

In this expression, *n* is the refractive index and $\Re$ is used to represent reflectance – not to be confused with thermal resistance. Also, the subscripts

glass and *air* denote the test cell material and air, respectively. In our experiments (at 532 nm) the refractive index of fused quartz glass is 1.46 and air is ~1.0. Thus, ~3.5% of the light is reflected off the front surface of the test cell. Note: there is also a reflection from the glass / fluid interface and some 're-reflections', but they are assumed to be negligible at < 0.25%. Also, any variations due to temperature are neglected in these calculations.

Lastly, the test cell needs to transmit infrared (IR) light to the IR camera. Since glass absorbs IR light, we need the glass wall to be thin. A 1mm glass cover will transmit about half of the IR signal from inside the sample. Whenever possible we tried to use microscope slide covers because at 0.2 mm thickness they transmit ~ 88% of the IR signal.

The volume fraction of nanoparticles in the base fluid must be chosen carefully to achieve effective absorption. If the nanoparticle concentration is too high, all the sunlight will be absorbed in a thin layer near the surface of the receiver – i.e. not volumetrically. For this case high temperatures will be present on the surface where heat can easily be lost to the environment. If the concentration is too low, a portion of the light will not be absorbed in the fluid. This can be stopped in the limiting case where a black backing (such as a Thurmalox 250 selective coating) is present, however.

For this study we will simply use 1% by volume of sodium dodecyl sulfate (SDS), which has proven to work well to stabilize nanofluids in our previous

work. The size and type of nanoparticles is also an important choice. For this study we have chosen to use spherical 20 nm silver particles – provided in powder form from Nanomaterials, Inc (Nanomaterials, 2011).

The black dye used in this study was a generously donated sample of 'Acid Black 1' from Pylam Products (Pylam, 2011). This dye is composed of several benzene rings with a molecular formula of roughly $C_{48}H_{35}N_9$. The molecular structure of the dye molecule has eight benzene rings. Thus, taking an average ring to ring distance of 0.3 nm, the dye molecule is ~2.4 nm long. Of course, this dye molecule can flex and rotate in three dimensions. Thus, the individual dye molecules are expected to be (in their largest dimension) about an order of magnitude smaller than the nanoparticles, and much less rigid.

In these experiments we are using two types of cameras - a visual and an infrared camera. Both cameras can be moved to view from various angles, but (as mentioned above) we will only use perpendicular and axial configurations.

In order to track what is happening in the test cell and to obtain information about bubble formation we use a Retiga (EXi Fast) 1.4 megapixel CCD camera. This camera is mounted on a Questar QM-1 long range microscope to obtain images with a variable magnification in the range of 2 - 4.5 at the image plane. Figure 44 shows a schematic of this system.

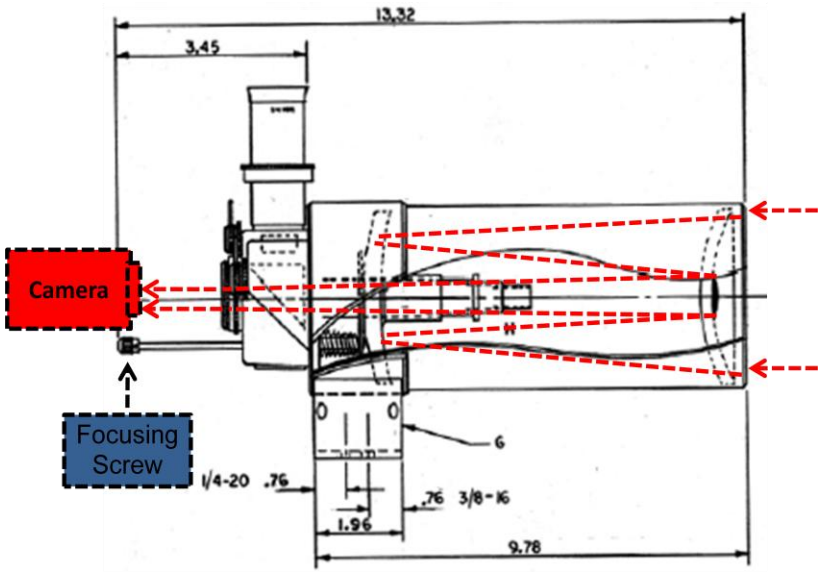

Figure 44. Ray trace of the Questar - QM-1 camera system - units are in centimeters - adapted from Questar.

The maximum frame rate of the visual charge coupled device (CCD) camera is 165 frames per second. Thus, under ideal conditions this camera can capture ~6 μm spatial resolution (for diffraction limited images) with a temporal resolution of ~6.1 milliseconds. Of course, we do not get perfect diffraction limited images looking through vibrating, imperfect optics at moving fluids - thus, in practice the smallest resolvable objects are closer to 20 μm.

The second camera is used to obtain temperature field measurements in the test cell. For this we use a FLIR Systems, Inc. (Prism DS) 0.77 megapixel infrared (IR) camera. The platinum silicide CCD in the camera is sensitive to wavelengths between 3.6 and 5 μm. This camera has a lens mounted on it which gives a magnification of ~2. Also, this IR camera can take video at 60 frames per

second. Thus, the resolution limits of the IR camera are ~25 μm (for diffraction limited images) and 16.7 milliseconds. Again, in practice we do not resolve perfect images, so the smallest resolvable objects are in the neighborhood of 50-60 μm. One additional specification for doing temperature measurement is the radiometric accuracy. According to the manufacturer, our IR camera is accurate to the greater of ± 2 ^{0}C or ± 2 %. Of course, this assumes that the user has set all of the other parameters correctly. That is, IR images can be corrected based on the emissivity, background temperature, optics temperature, relative humidity of the air, distance to the object, the effect of windows, etc. All of these corrections are accounted for in the software in the camera. These variables can also be accounted for by post-processing the images via commercial software or user-defined code. In our experiment these variables are kept constant as much as possible. Therefore, in general, we expect errors of less than ±5 ^{0}C.

4.4.3 Experimental Calibration Procedure

Before conducting the experiment, the IR camera needs to be calibrated against targets with known temperatures over the range needed in the experiment. In the test cell we want to obtain temperature measurements in water-based fluids through microscope slide glass. Thus, one simple calibration is to take IR images of our test cell where the temperature is controlled with a hot plate. This was done in 5^{0}C increments from room temperature to boiling - as measured by a T-

type thermocouple. Figure 45 shows some sample images of from this calibration. The boxed temperature values in the bottom-center of each image represent the thermocouple reading. Also, in each IR image a 'scratch' appears in the bottom-left corner. This is a flaw in either the optics or the CCD chip. Hence, it is simply an artifact that appears in every image and should be ignored.

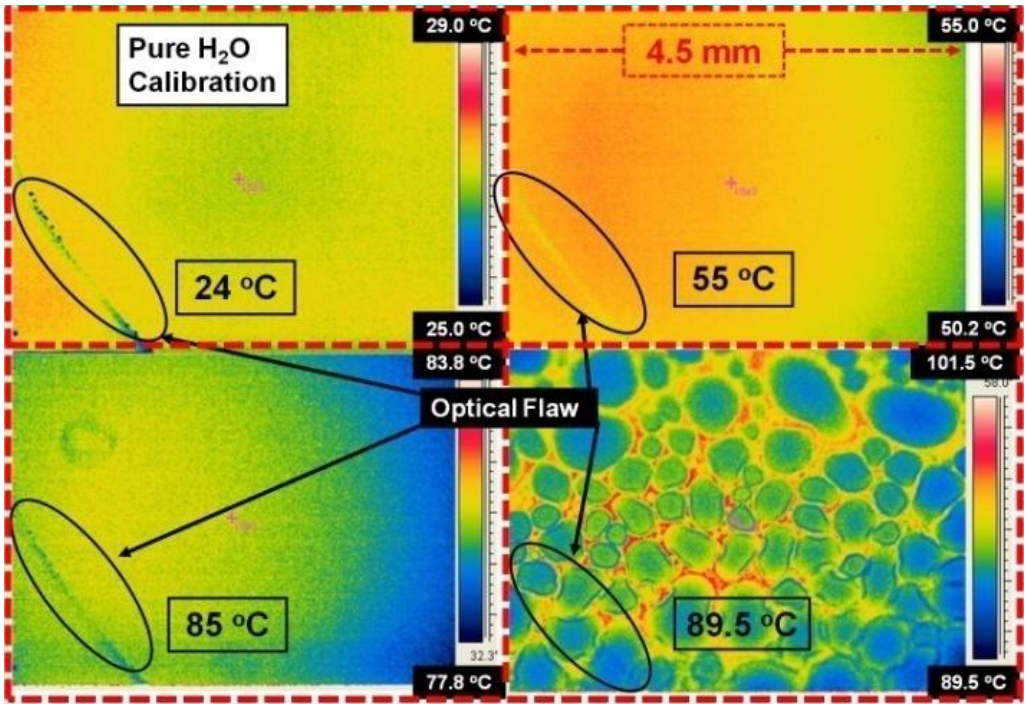

Figure 45. Sample IR images of the fluid inside our test cell heated with a hot plate.

To understand the effect of adding particles to the water, this calibration is repeated with the highest concentration nanofluid used in this study - 1%v Ag/H_2O - shown in Figure 46.

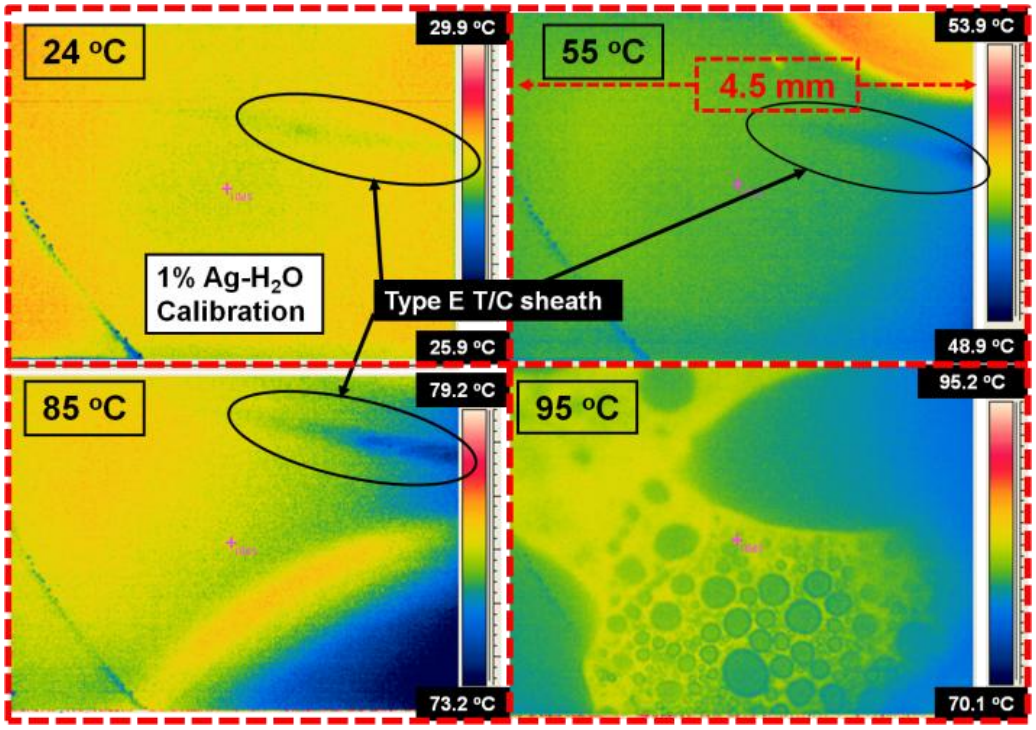

Figure 46. Sample IR image of a fluid with a controlled temperature viewed inside our test cell.

These calibration results indicate that the error involved in taking IR temperature measurements through the test cell can be expressed in the form:

$$Error = \frac{T_{IR} - T_{T/C}}{T_{T/C}} = ALog\left(T_{IR}\right) - B \qquad (73)$$

where the subscripts IR and T/C represent the infrared reading and the thermocouple reading, respectively. A and B are constants which are determined through the calibration procedure. This error can then be subtracted from the IR reading to improve the accuracy of measure temperatures through the test cell. The coefficient used in this analysis are given in Table 5.

Table 5. Coefficients used to correct the IR measurement - i.e. curve fit of calibration data.

Eqn. (3) Constants	A	B
DI H2O	*-0.138*	*0.556*
Black Dye	*-0.128*	*0.482*
Ag Nanofluid	*-0.118*	*0.408*

Figure 45 and Figure 46 show that above certain temperatures (say 90^0C) this calibration does not work. Therefore, further calibration can be done at higher temperatures using a hot wire. This is appropriate since a hot wire represents a heater geometry very similar to that of the laser input. However, in order to do this the wire must have a known size, temperature coefficient of resistance, and emissivity. The wire used in these experiments is 30 AWG (D = 0.255 mm), MWS 294R which is composed of 54% iron, 29% nickel, and 17% cobalt. The emissivity of this polished wire is assumed to be constant at $\varepsilon \sim 0.35$. Of course at high temperatures - e.g. the Curie point of cobalt (~1,100 ^{0}C) - there will a change in emissivity. However, constant wire emissivity is considered to be a good approximation for the range of temperatures used in this study.

Note: water has an emissivity of 0.95-1.0 whereas for thin layers of steam, emissivity is < 0.1. This is because if we are looking from a normal direction (with our IR camera) at a steam water interface, thin layers of steam are nearly

transparent. The emissivity of steam is estimated using Hottel's equation for effective emissivity (Hottel & Sarofim, 1967):

$$\varepsilon' = \left(\frac{1}{\varepsilon_w} + \frac{1}{\alpha_g} - 1 \right)^{-1} \quad (74)$$

where ε', ε_w, and α_g represent the steam emissivity, the water emissivity, and the absorptivity of steam, respectively.

In general, the temperature of a hot wire can be determined by calculating the resistance of the wire, R_{wire}. A voltage measurement over the heating wire, V_{wire}, and a separate voltage measurement over a shunt resistor, V_{shunt}, are needed. The shunt resistor used in this test is 0.1 Ω ± 1% from Mouser Electronics - (Electronics, 2011). Thus, the wire temperature can be calculated by plugging these measured voltages into the following equations:

$$I_{wire} = \frac{V_{shunt}}{R_{shunt}} \quad (65)$$

$$R_{wire} = \frac{V_{wire}}{I_{wire}} \quad (66)$$

$$\frac{R_{wire}}{R_{ref}} = 1 + \alpha \left(T - T_{ref} \right) \quad (67)$$

where R_{ref} and T_{ref} are the resistance and temperature at normal room conditions. The temperature coefficient of resistance for the MWS 294R wire is 3.3 x 10^{-3}

$\Omega/^0$C (MWS Industries, 2011). This wire was chosen specifically because of its extremely high temperature coefficient of resistance. It also has reasonably high resistivity (294 Ω / Circular Mil Foot or 4.89 x 10^{-5} Ω-cm (MWS Industries, 2011)). Thus, in water the wire can be heated to the critical heat flux (or burn-out point). An error propagation analysis gives 2–3 ^{0}C error in the calculated wire temperature for this set-up.

Figure 47 shows some sample IR and visual images from this experiment. We can see that boiling was achieved in a sub-cooled fluid - which is also expected with laser heating.

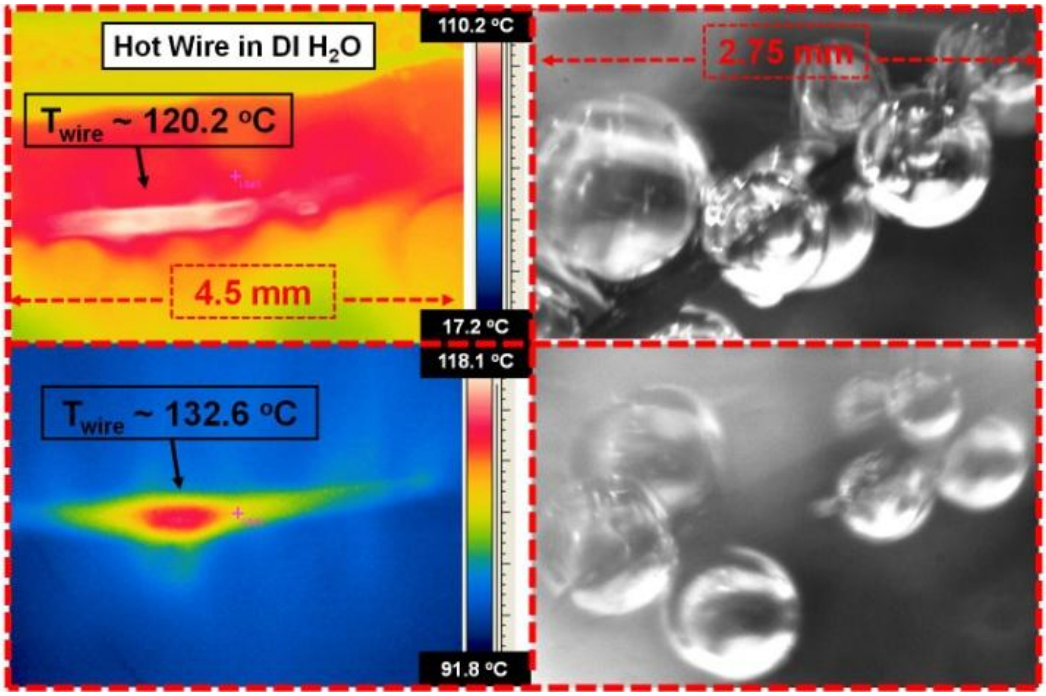

Figure 47. Hot wire in water IR calibration in test cell - calibrated using eqn. (3).

It turns out that the IR measurements tend to under estimate the wire temperature at higher temperatures. Also, the error stays very near the trend

found in the hot plate calibration. Thus, in the proceeding analysis we will simply extend the correction presented in equation 3. (Note: The highest achievable temperatures in this calibration were ~ 120 ^{0}C. For temperatures much above 100 ^{0}C, however, the temperature coefficient of resistance is not necessarily constant.)

As mentioned above, this experiment is basically a comparison study of water with a black backing, black dyes, and nanofluids. As such, we have collected a multitude of IR and visual images for each of these with laser heating. Tests were conducted for each fluid in both the perpendicular and the axial configuration. Also, for each of the absorbing fluids we tested several volume fractions - ranging from 0.125 to 1.0 % volume fraction. In the following section, due to space limitations, we will only present a cross-section of these results.

4.4.4 Perpendicular Configuration Results

In order to get good results with this configuration, the heated region must be within the first 100 μm of the fluid. This is because the average absorption coefficient for water between 3.6 - 5 μm (the IR sensitive range of the CCD chip) is ~288 cm^{-1}. Thus, >95% of IR emission signal in this spectral range is absorbed in a 100 μm thickness of water. This makes it very difficult to obtain IR images simultaneously with the visual images. Therefore, most of the following visual and IR images do not directly correspond to one another in time or space. Rather,

they present the same test sample and test conditions viewed from slightly different points of view.

The first test in this configuration is water with a black backing. This is considered to be the 'baseline' case because it simulates a conventional surface-based light absorber. Figure 48 shows some characteristic IR and visual image results for this test. In the IR images we can see that pretty high temperatures are reached. Also, small bubbles are seen in the visual image. (Note: the laser is coming into the IR and visual images from the opposite direction - as is noted in the figure.)

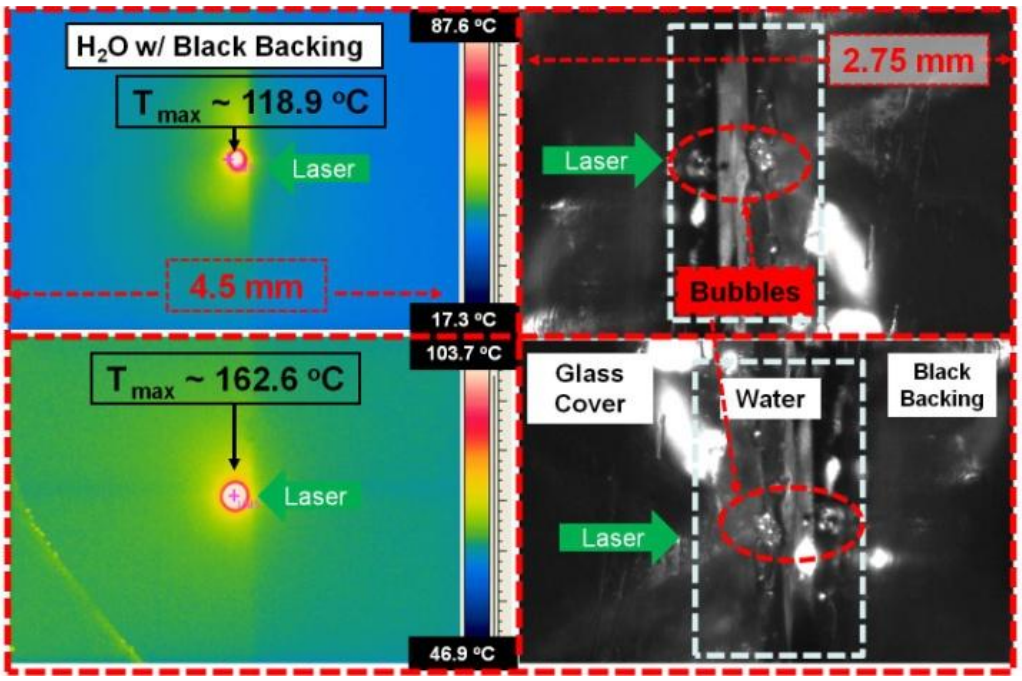

Figure 48. IR and visual images of de-ionized H_2O with a black backing exposed to ~75 W/cm^2 laser irradiance in the perpendicular configuration - temperatures calibrated using eqn. (3).

One goal of the experiment is to find vapor generation rates. This will most likely be done with the visual images, but bubbles can also be seen in the IR images. Figure 48 shows some micro-bubbles (diameters of 30-50 μm) being formed at the laser input site. The pressure inside these small bubbles is expected to be slightly higher than the surrounding fluid (0.05-0.08 atmospheres above according to the Young-Laplace equation), so the saturation temperature of water is correspondingly elevated - around 101 ^{0}C to 102 ^{0}C. That is, small vapor bubbles indicate high pressure and temperature inside the bubble.

Unfortunately, bubbles are much harder to see in black absorbing fluids. Figure 49 and Figure 50 show characteristic IR and visual images of a black dye and a nanofluid heated by the same laser irradiance. In the visual images we do see some bubbles, but they are too small and inconclusive to find vapor generation rates at this time. It is possible that these are steam bubbles, but it is unlikely since they are not condensing in the surrounding sub-cooled fluid.

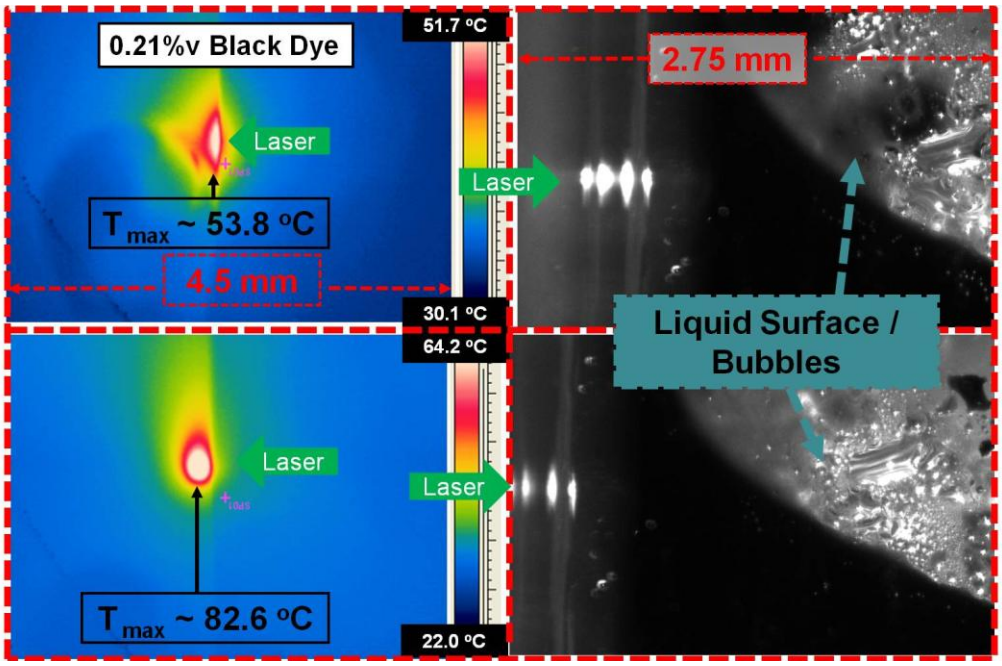

Figure 49. Visual images of a 0.21%v Pylam 'Acid Black 1' dye exposed to ~75 W/cm^2 laser irradiance in the perpendicular configuration - temperatures calibrated using eqn. (3).

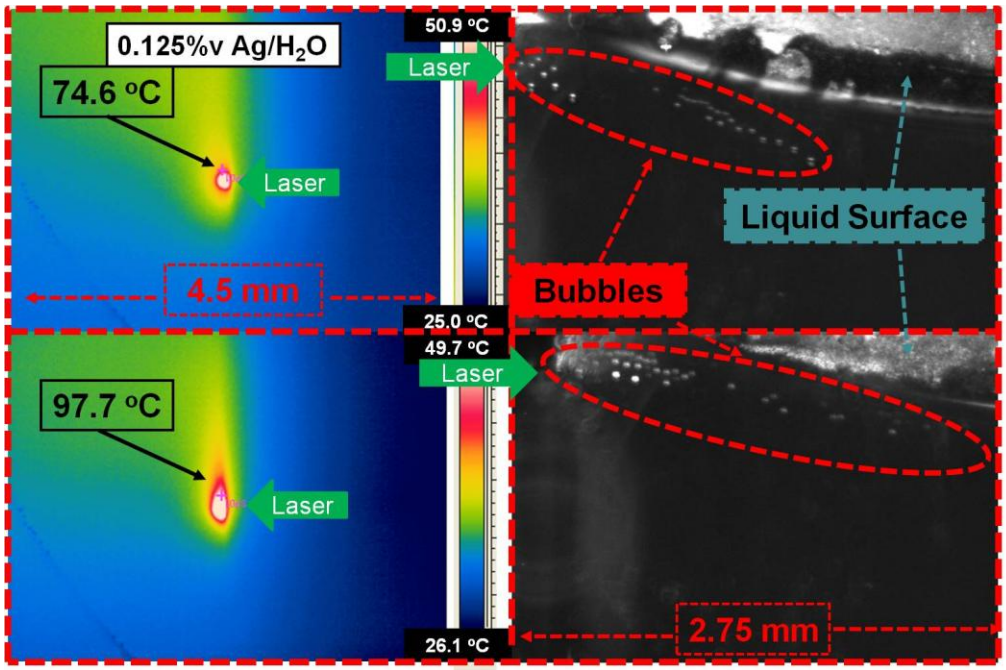

Figure 50. IR images of a 0.125%v Ag nanofluid exposed to ~75 W/cm^2 laser irradiance in the perpendicular configuration - temperatures calibrated using eqn. (3).

One of the main advantages of the perpendicular configuration is that it may be possible to generate boiling curves from **one** image. That is, one image can potentially provide heat flux inputs (y-axis) and the fluid superheat temperature (x-axis) required for a boiling curve. With known fluid absorption (read: known fluid properties), one can calculate exponentially varying heat flux values in the direction of beam propagation. Of course this is only possible for an absorbing (i.e. participating) fluid.

A simple approximation of this can be found assuming that scattering and emission by the fluid are negligible relative to the intense laser input. Thus, by

finding the light absorbed in a differential slice of fluid (from Beer's law), we can approximate the heat flux at that 'slice' as:

$$q'' = \frac{D_{waist}}{4} \frac{I_o \left(e^{-\alpha x_1} - e^{-\alpha x_2} \right)}{x_2 - x_1} \quad (75)$$

where D_{waist} is the focused laser beam diameter, I_o is the incident light intensity, α is the absorption coefficient, while x_1 and x_2 are penetration distances along the beam path. Note: this approximation is only good for small changes in x (i.e. only a few % change in light intensity), and for isotropic, highly absorbing (non-scattering) samples.

If we assume that the outer edge of the beam cylinder is the effective 'wall' temperature, then at each 'slice', we can theoretically calculate the superheat temperature difference from the IR images. Unfortunately, it can be seen in

Figure 49 and Figure 50 that our IR spatial resolution will only yield a very rough estimate of these values. Also, if fluid motion is large this approach may not be directly comparable to conventional boiling curves. Figure 51 shows some boiling curves obtained for black dye and nanofluid images obtained in this work. As a comparison, boiling curves for pure water (using the 294R wire of this study) and bounding condition for a rough and smooth heater surface in Rohsenow's correlation are also shown (Mikic & Rohsenow, 1969). Again the wire is thought to be a good comparison because it has a very similar geometry to the focused laser beam.

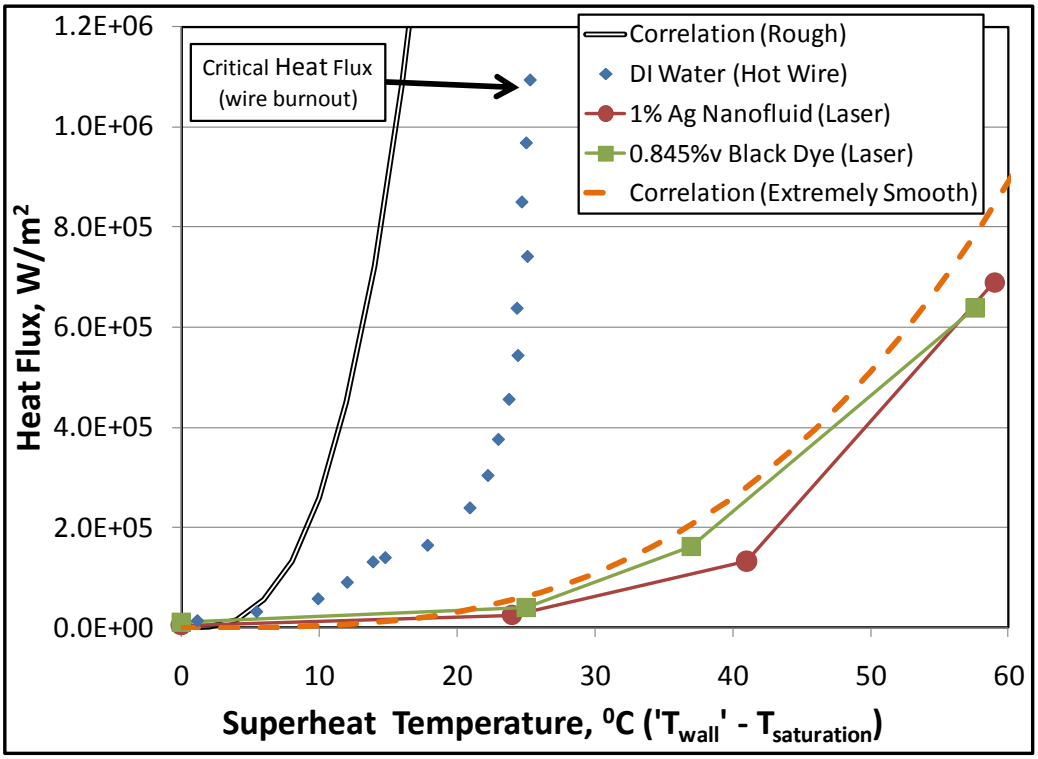

Figure 51. Estimation of the nucleate boiling curves for a .845%v black dye and a 1.0 %v Ag nanofluid. Also, boiling curves of a hot wire in DI water and Rohsenow's boiling heat transfer correlation.

The boiling curves for a laser heated sample appear to have much higher superheat values for the same heat flux as compared to conventional surface boiling. This is analogous to boiling on an extremely smooth heater. This also implies that the boiling heat transfer coefficient for volumetric heating is very low compared to surface heating - a factor of 10-20 lower. Also, the nanofluid appears to have a lower 'laser boiling heat transfer coefficient' than a black dye. One possible explanation of these phenomena is that there are relatively few nucleation sites - i.e. not as many places for bubbles to form in these fluids. Another possible explanation is that heating is happening in such a small, localized region that it has a hard time transferring out. Future work in this area is needed.

4.4.5 Parallel Configuration Results

The main advantage of the parallel configuration is that we can accurately control the fluid thickness which we are monitoring. That is, we look at very thin slices of fluid, which usually results in better images. It is also easier to align the cameras with the part of the sample exposed to the beam in this configuration. As in the previous configuration, we started by testing pure water with a black backing. Figure 52 shows characteristic images from this test. In the IR images we see very high temperatures - over 300 ^{0}C. This is logical since all the heat is

absorbed on the surface which has very little volume. It must then transfer to the rest of the fluid via convection or out of the sample via conduction through the test cell - as described in figure 1. We expect that in a real application, having such high temperatures near the outer surface would indicate high heat losses.

On the other hand, these high temperatures were higher than any observed in the perpendicular configuration - indicating that one measurement is not accurate. This is most likely due to the fact that some of the signal is absorbed in the perpendicular configuration.

We were also able to observe bubble growth on the back surface as indicated by the consecutive visual images in Figure 52. It appears that the diameter of the bubble nearly triples in these images which were taken a couple seconds apart.

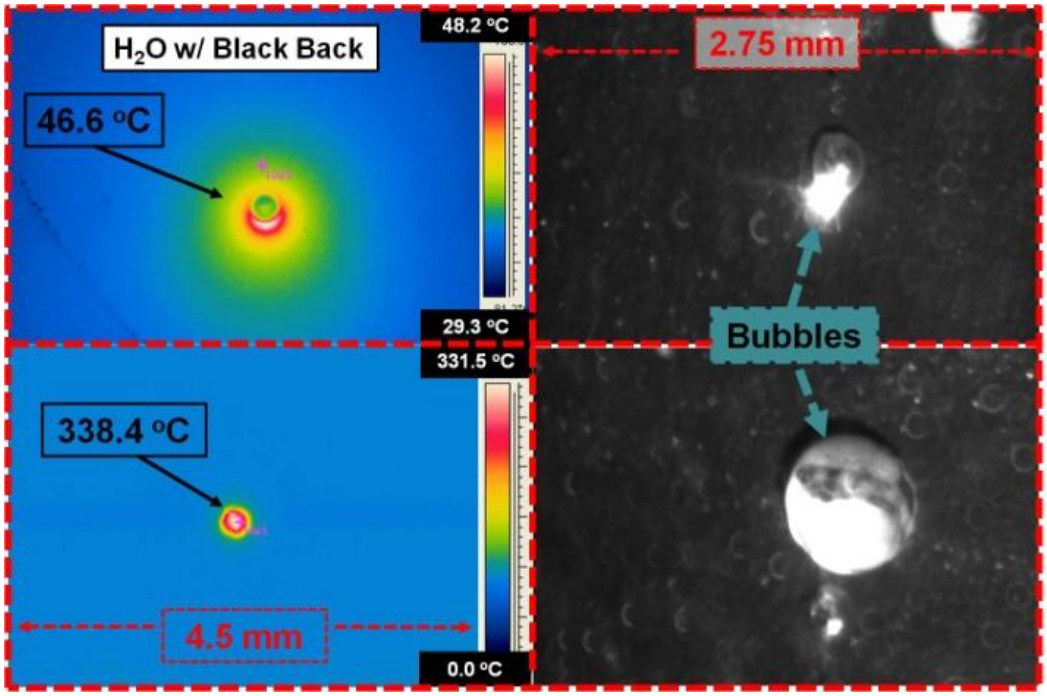

Figure 52. Visual images of de-ionized water with a black backing exposed to ~75 W/cm^2 laser irradiance in the perpendicular configuration - temperatures calibrated using eqn. (3).

For the black dye tests, we again see higher than what was seen in the perpendicular configuration. Figure 53 shows tests with 0.845% volume fraction Pylam 'Acid Black 1' dye. A high volume fraction was chosen to make sure bubbles are produced. In the visual image we can see many small micro-bubbles surrounding a central vapor hole. Again, however, it is hard to quantify vapor generation rates with the resolution available in our visual camera system.

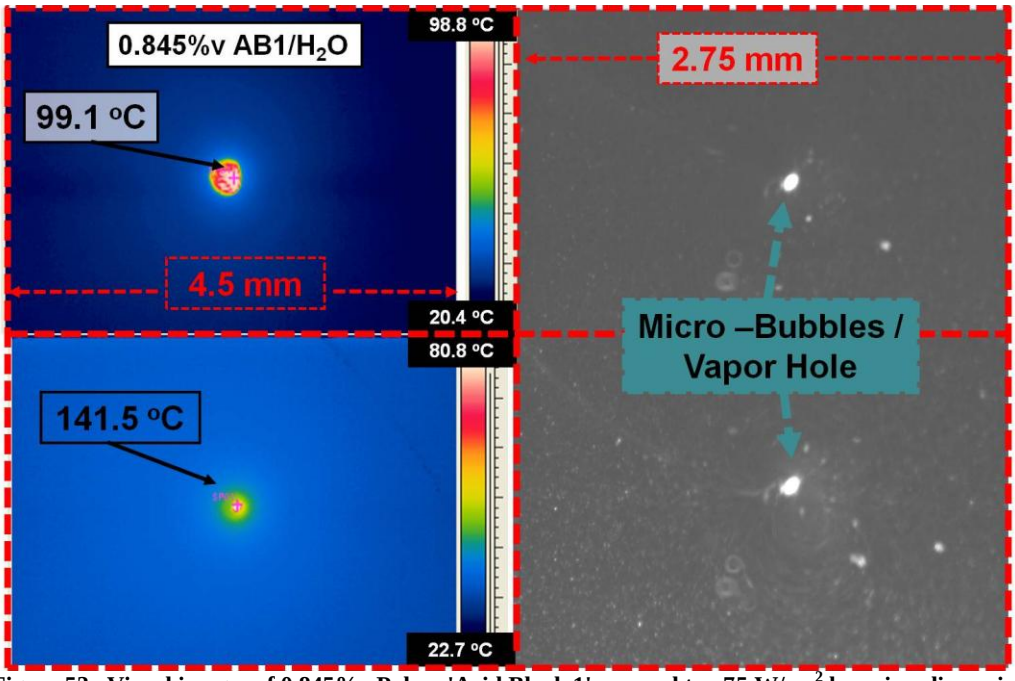

Figure 53. Visual images of 0.845%v Pylam 'Acid Black 1' exposed to ~75 W/cm^2 laser irradiance in the perpendicular configuration - temperatures calibrated using eqn. (3).

To compare / contrast with the higher volume fraction black dye, Figure 53 shows some characteristic images of 1%v silver nanofluid. A similar 'hole' is seen in the center of the beam spot. The big difference, however is that much higher temperatures were seen in the nanofluid sample. It is possible that this is because of high absorption due to particles clumping around the laser spot - as is seen in the visual images in Figure 54. This could also be due to the somewhat larger vapor bubbles that form, which can hinder heat transfer out of the local region.

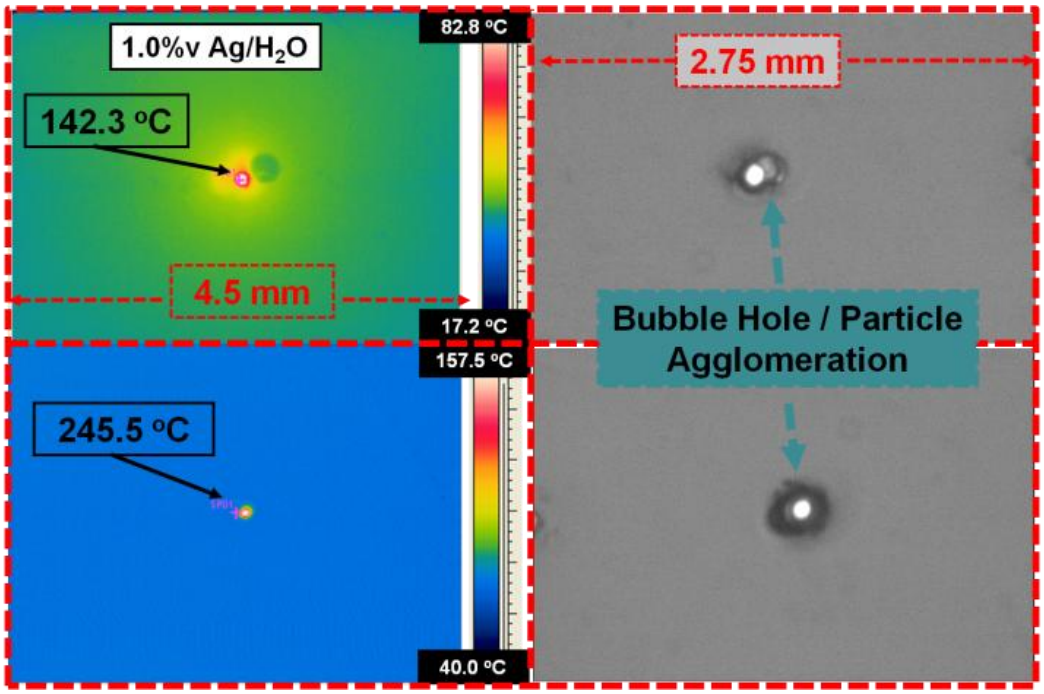

Figure 54. Visual images of a 1 %v Ag nanofluid exposed to ~75 W/cm^2 laser irradiance in the perpendicular configuration - temperatures calibrated using eqn. (3).

One key thing that was learned in these experiments is that there are fundamental differences in volumetric absorption versus solid surface absorption. At this time we cannot conclude if these differences are advantageous or disadvantageous. We see high localized temperatures due laser heating in absorbing fluids. It may be possible to take advantage of the high temperature gradients that are generated - in many cases > 1,000 ^{0}C per mm. Along these lines, silver nanofluids tested in this study appear to be more efficient absorbers (for the same volume fraction) as compared to black dyes. Recall: silver has a large plasmon resonance absorption peak near the laser wavelength, so this was

expected. On the other hand, the 'laser boiling heat transfer coefficient' is reduced by a factor of 10-20 from surface boiling of pure water. Thus, it is unclear from these results if a direct volumetric absorber / steam generator will be an appropriate application. Further optimization, study of other materials / geometries, and work with larger scale samples will be needed to answer this question.

4.5 Volumetric vs. Surface Boiling

There are several fundamental reasons that nanofluids might prove advantageous to solar thermal advantageous to solar thermal energy harvesting. First, only very small amounts of nanoparticles are of nanoparticles are needed to make an efficient absorber (< 1% by volume). Second, the extremely Second, the extremely small size of the particles allows them to pass through conventional pumps and conventional pumps and plumbing without adverse effects. Third, as is discussed above, significant above, significant enhancement in a wide range of thermal, optical, and catalytic properties over bulk properties over bulk properties are possible for 'solar nanofluids'. Finally, the absorption process is absorption process is fundamentally different - it is a volumetric rather than surface-based surface-based phenomena.

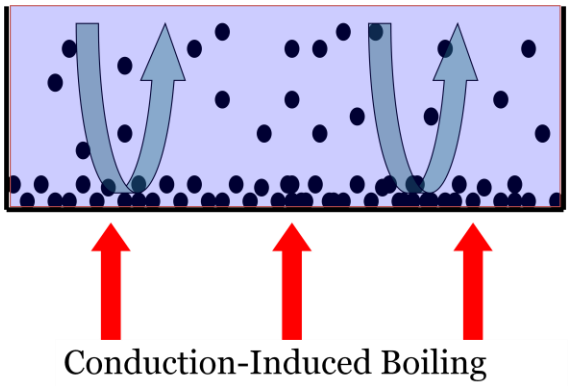

Conduction-Induced Boiling

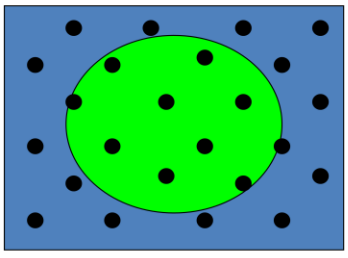

Light -Induced Boiling

Figure 55Figure 55 gives general description of this difference for two nanofluids

To compare the previous two sections and examine this fundamental difference further, this section is devoted to discussing this issue in detail.

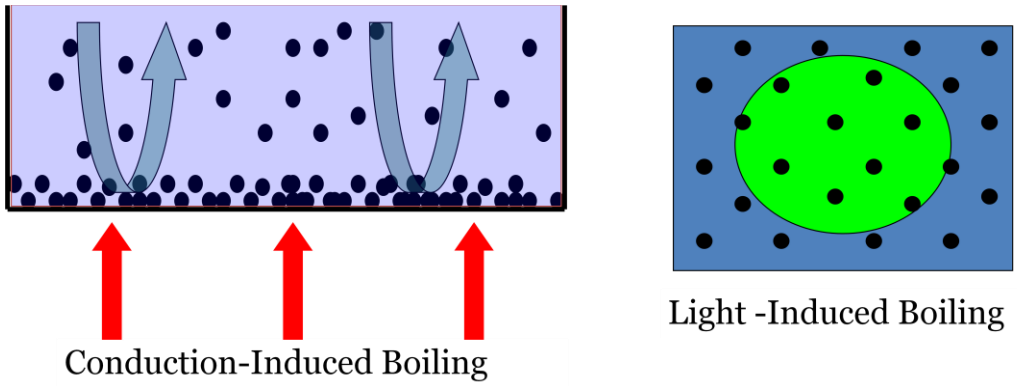

Figure 55. Surface versus Volumetric - heat addition in nanofluids. Left - Surface-based heating; Right - Volumetric-based heating.

4.5.1 Volumetric vs. Surface Light Harvesting

The most commonly built (and designed) solar thermal power plants are based on parabolic trough or power tower solar collection technology (Towers, Gonzalez-aguilar, & R, 2007). In these systems sunlight must be efficiently concentrated and absorbed (i.e. converted to heat) on a solid surface. The heat must then be transferred to the working fluid of the thermal cycle - this may take multiple steps. In hopes to improve upon this concept, this article will discuss the feasibility of absorbing light *directly* in the working fluid - skipping any

intermediate heat transfer steps. This was described in Figure 5, which compares this type of system to a conventional one in terms of a thermal resistance network - shown again here for convenience.

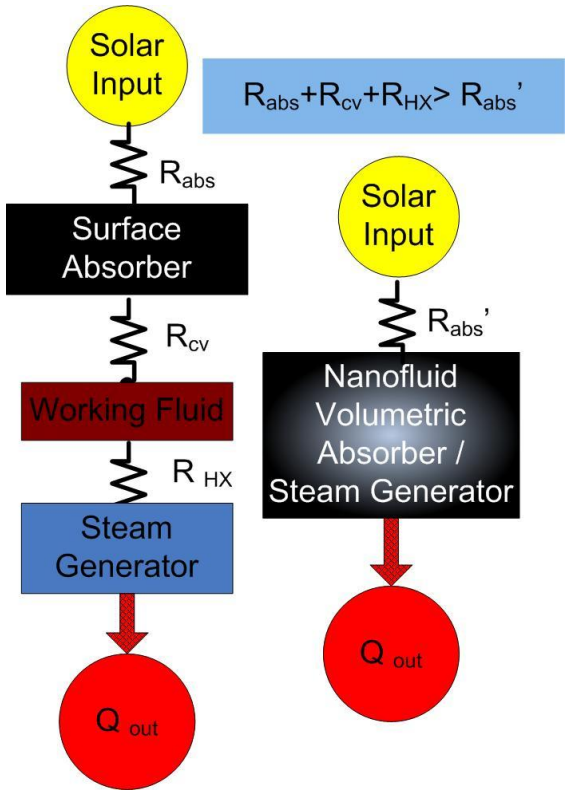

Figure 56. Thermal resistance network - comparison between a conventional solar thermal plant and a nanofluid solar thermal plant. R_{abs}, R_{cv}, R_{HX}, and $R_{abs'}$ refer to thermal resistances present during the solar solid surface absorption, conduction/convection from a solid surface, and solar direct absorption/steam generation heat transfer steps, respectively.

Large scale thermal cycles almost always use steam as the working fluid, but some solar thermal power plants also use organic working fluids. Regardless of the fluid choice, electricity is produced by expanding a hot, gas-phase fluid through a turbine which then turns a generator. Thus, the working fluid must undergo phase change to reach the turbine inlet state. This step is usually done

inside a boiler - which requires another heat transfer step. In an effort to cut out this step, we will discuss the feasibility of simultaneously absorbing light and causing phase change directly in the working fluid - which is also incorporated in Figure 5. Specifically, the following experiments will present experiments with a simple stagnant volumetric (water-based) solar absorber / steam generator.

4.5.2 Volumetric vs. Surface Boiling Observations

The fluids used in these experiment have comparable optical properties, but different particle sizes - or no particles in the case of water with a black backing. The test were conducted with water-based fluids of both large (> 1μm) and small (< 1nm) sized particles comparison. The smaller particles are represented by molecular fluids - pure water and water with dissolved iodine. The larger particles consist of the black dyes mentioned above, which were donated by Pylam Products, Inc. – Tempe, AZ. The dye – when dispersed in DI water – is composed of particles with an average size of 1.2μm, but with a large standard deviation. The mixture presumably has many different sized particles which absorb various parts of the optical spectrum.

For this experiment we wish to control the irradiance that is put into the sample. This is done using a neutral density filter. The resultant laser beam irradiance is measured by a laser power meter. The power meter is also used to

measure the fraction (if any) of laser light which is transmitted through the sample. Figure 57 shows this experimental set-up.

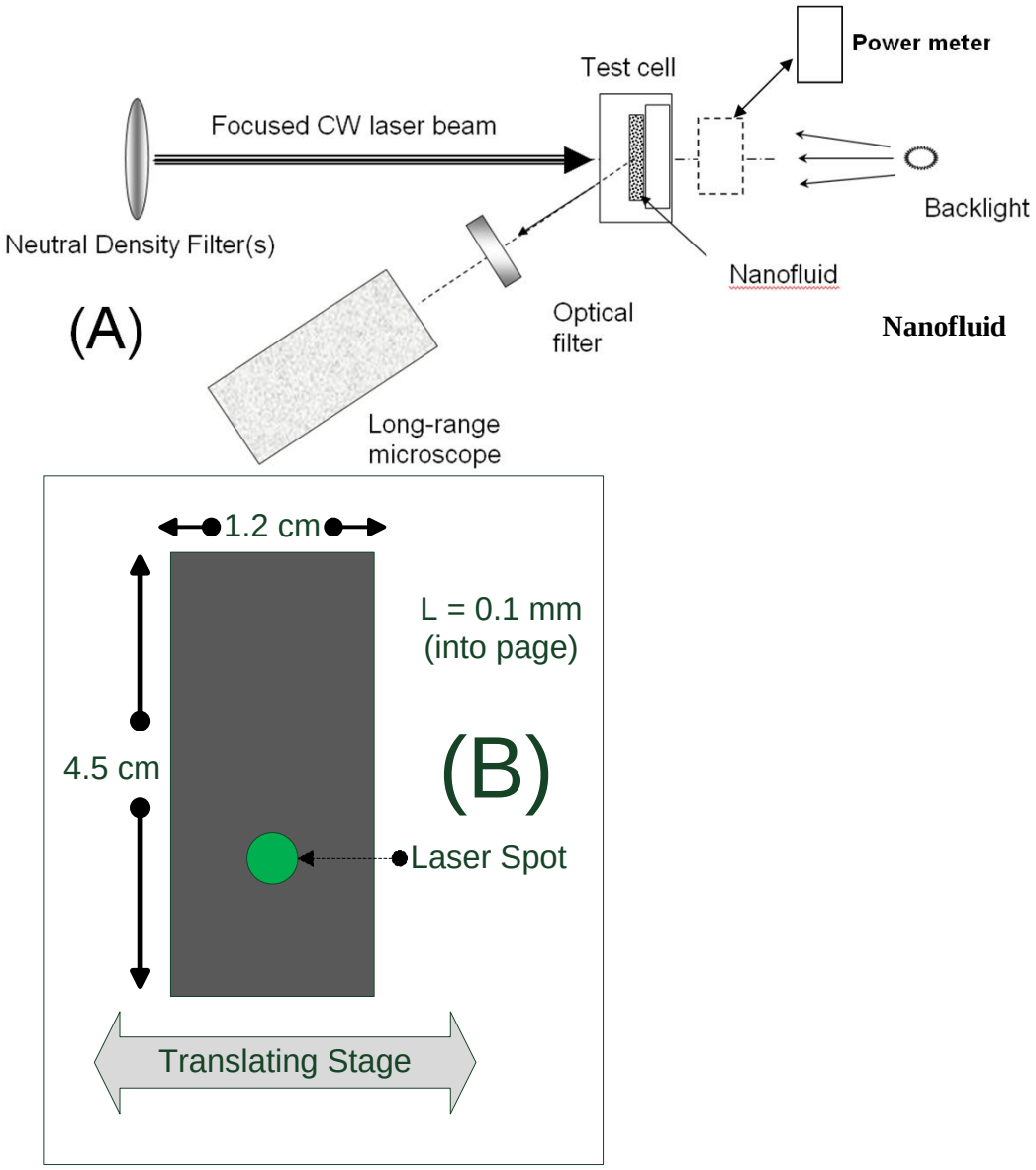

Figure 57. Experimental system: (A) overall test set-up, (B) test cell close-up (laser beam is into page).

As a first step in this experiment, and to prove the optical property data from this chapter and the previous chapter, pure water is exposed to the laser beam inside a cuvette. Characteristic images of pure water with a transparent backing and with a black backing are shown in Figure 58.

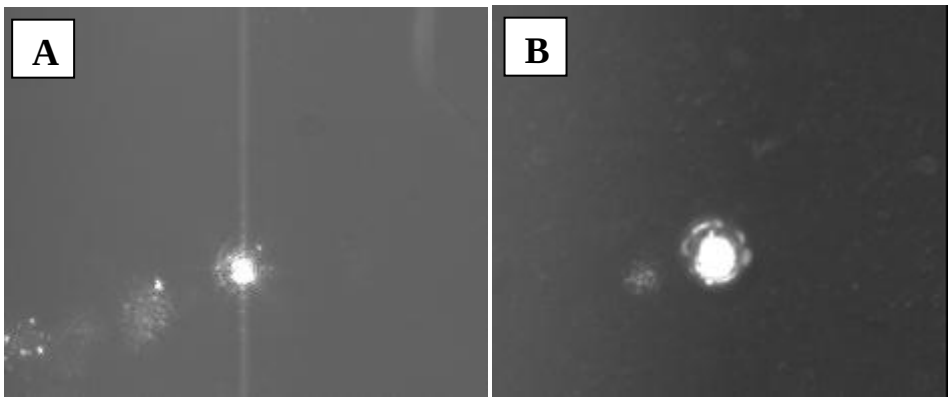

Figure 58. Water exposed to ~770 W/cm^2, 532 nm laser light: A) in a clear cuvette, and B) in a cuvette with a black backing.

The tested nanofluids were copper, graphite, silver and multi-walled carbon nanotubes (nominal diameters of 2-40 nm at 1%, 0.75%, 0.5%, 0.25%, 0.1%, and 0.05% by volume) in a clear cuvette with the same DI water/surfactant base fluids. Figure 59 shows a series of typical images during a stationary laser heating experiment. The lighter areas occur due to transmission of the back-lighting through a region containing a lower concentration (than average) of nanoparticles. The buoyant plume that occurs above the laser column wavers and shows vertical flow in it. The buoyancy that drives this flow may come from laser heating or from micro-bubbles emerging from the heated region. Temperatures in the plume are not likely to be high enough to affect the optical

density of the nanofluid, so the partial transmission associated with the buoyant plume must be due to micro-bubbles and/or particle depletion in the hot region of the laser column. The brightest regions toward the bottom of the laser beam are probably light transmitted through a vapor bubble. Thus, in this series of images, a vapor bubble forms and grows in the heated region. It leaves after the laser is turned off at ~130 s. The last image shows the bubble separated from an area where the nanoparticles are heavily concentrated.

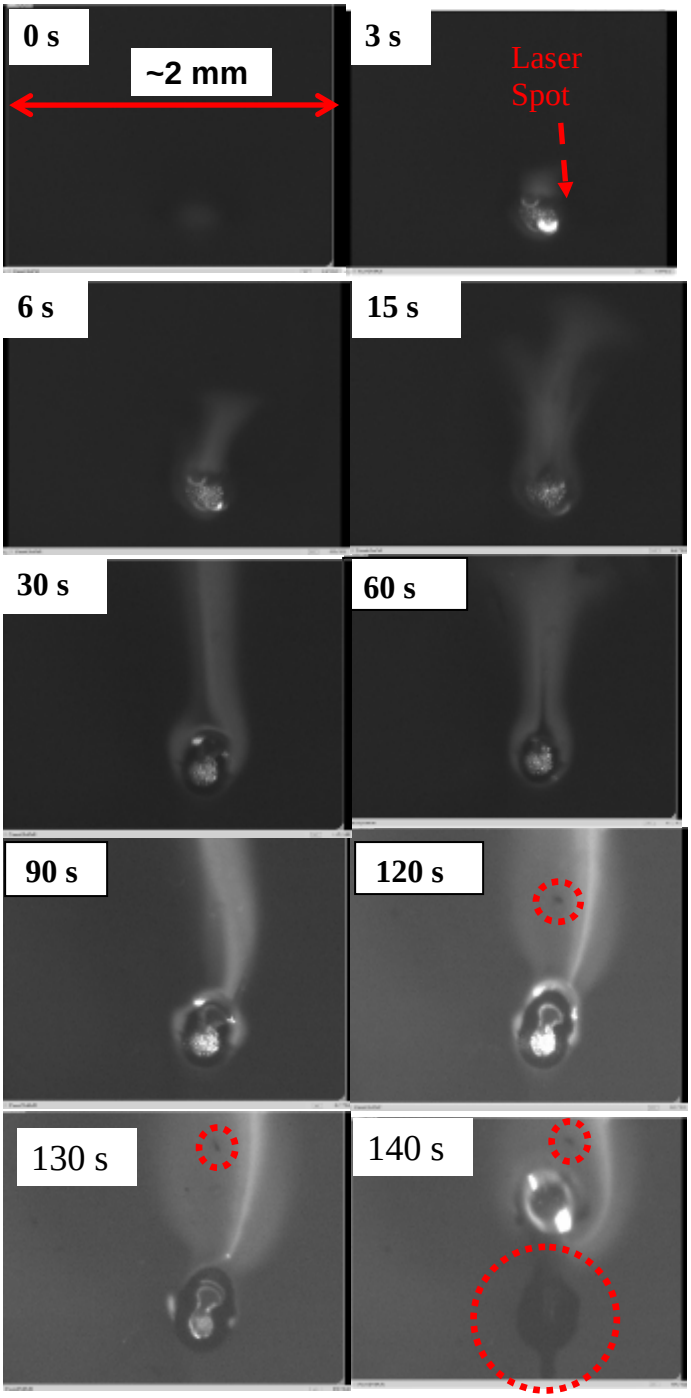

Figure 59. Bubble generation in a laser-heated 0.1% by volume graphite/water nanofluid – dashed circles indicate high concentrations of graphite nanoparticles.

4.5.3 Volumetric vs. Surface Boiling Incipience

Local bubble generation in a sub-cooled (~ 25^{o}C) fluid is only possible if the laser irradiance is high. The minimum irradiance (in W/cm^2) necessary to cause phase change in these nanofluids was found by varying laser intensity entering the fluid using neutral density filters to attenuate the beam in steps of ~100 W/cm^2. The nanofluids mentioned above were tested to determine the minimum irradiance necessary to cause phase change as a function of volume fraction. Figure 60 shows trends as compared to the water base fluid with a black backing. Some nanofluids underwent phase change for significantly less irradiance than water with a black backing, or for water containing Pylam black dye. Note: no vapor bubbles were observed in pure water with a clear (e.g. non-absorbing) backing for these laser fluxes – thus, this control fluid is not plotted.

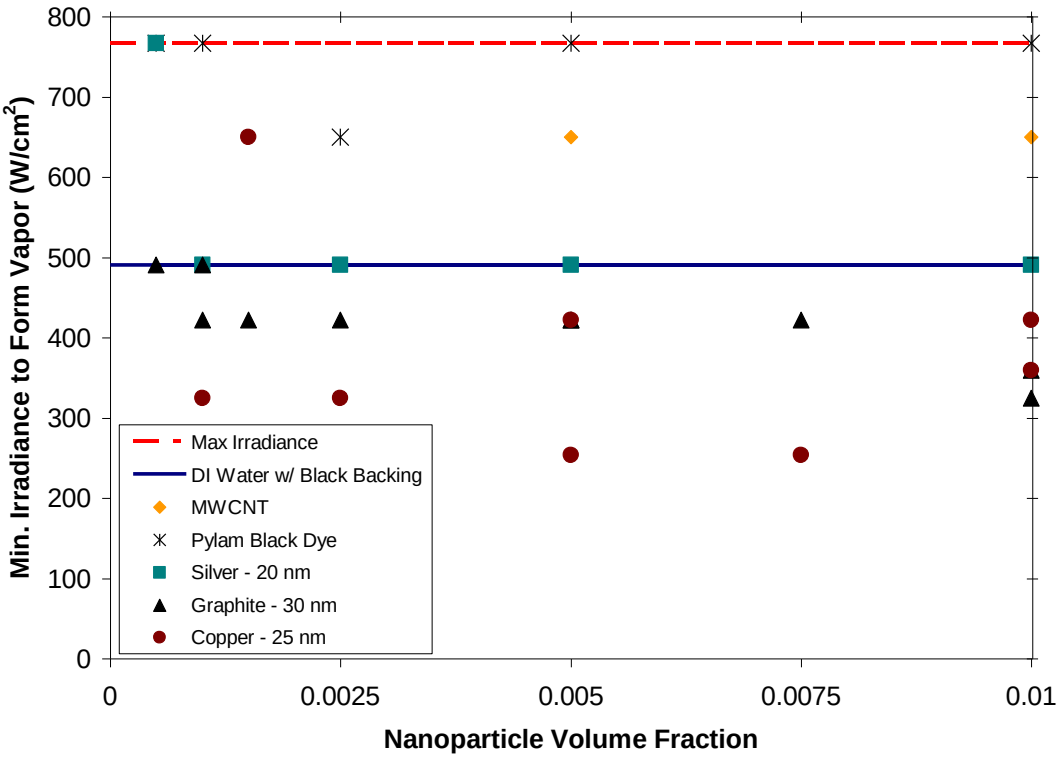

Figure 60. Irradiance needed to locally boil nanofluids with a CW laser as compared to the base fluid and de-ionized water with a black backing.

These experiments indicate that volumetrically heated nanofluids can undergo liquid-vapor phase change more easily than their base fluids exposed to surface heating. In fact, up to ~50% less irradiance is necessary to create vapor in a 0.75%v copper nanofluid. Copper can be calculated (using the independent Rayleigh scattering assumption as given in (Bohren & Huffman, 1998)) to have an order-of-magnitude higher absorption efficiency than graphite at 530 nm. Since copper is the best absorber (of the materials tested), it is reasonable that it will generate vapor at the lowest irradiance. This same logic can be applied to

compare graphite and silver since graphite has double the absorption efficiency of silver.

There may be an optimum volume fraction which minimizes the irradiance necessary to drive phase change for this configuration. This is expected because low particle loadings approach the high transmittance of water and are not effectively heated. Higher particle loadings absorb the light energy close to the wall – approaching area/surface heating which may lose a significant amount of heat through the wall. The data points for copper in Figure 60 appear to follow this trend. Trends as a function of volume fraction for other fluids cannot be inferred from the experiments performed to date.

4.5.4 Volumetric Bubble Formation

The experiment revealed other interesting physics that may be at work. First, phase change in pure liquid boiling commonly begins in small defects (nucleation sites) on a macro-scale *surface*. For light-induced phase change in nanofluids, however, the *particles* become the heating surface. This is an important, and as yet not well-understood, difference.

Second, as indicated in Figure 59 and especially in Figure 61, there are several distinct non-uniform spots in the fluid which have high concentrations of dark fluid that must be regions of concentrated particle mass. Since graphite melts at ~3,850^{o}C and vigorous agitation can break these large regions up, it

seems unlikely that these large clumps are molten and/or re-solidified graphite particles as predicted by (Merabia, et al., 2009). Thus, high concentration regions are thought to be loosely bonded particle agglomerates. It is unclear whether these dark regions lead or lag vapor formation. Dense collections of particles are expected to absorb light over a shorter path length (i.e. in a smaller volume), which could cause a higher local temperature - driving phase change. Conversely, as vapor forms, particles could be left behind forming high concentration regions. There is evidence for the latter in that the dark regions appear to grow with exposure time and all resolvable bubbles appear clear – i.e. lacking particles.

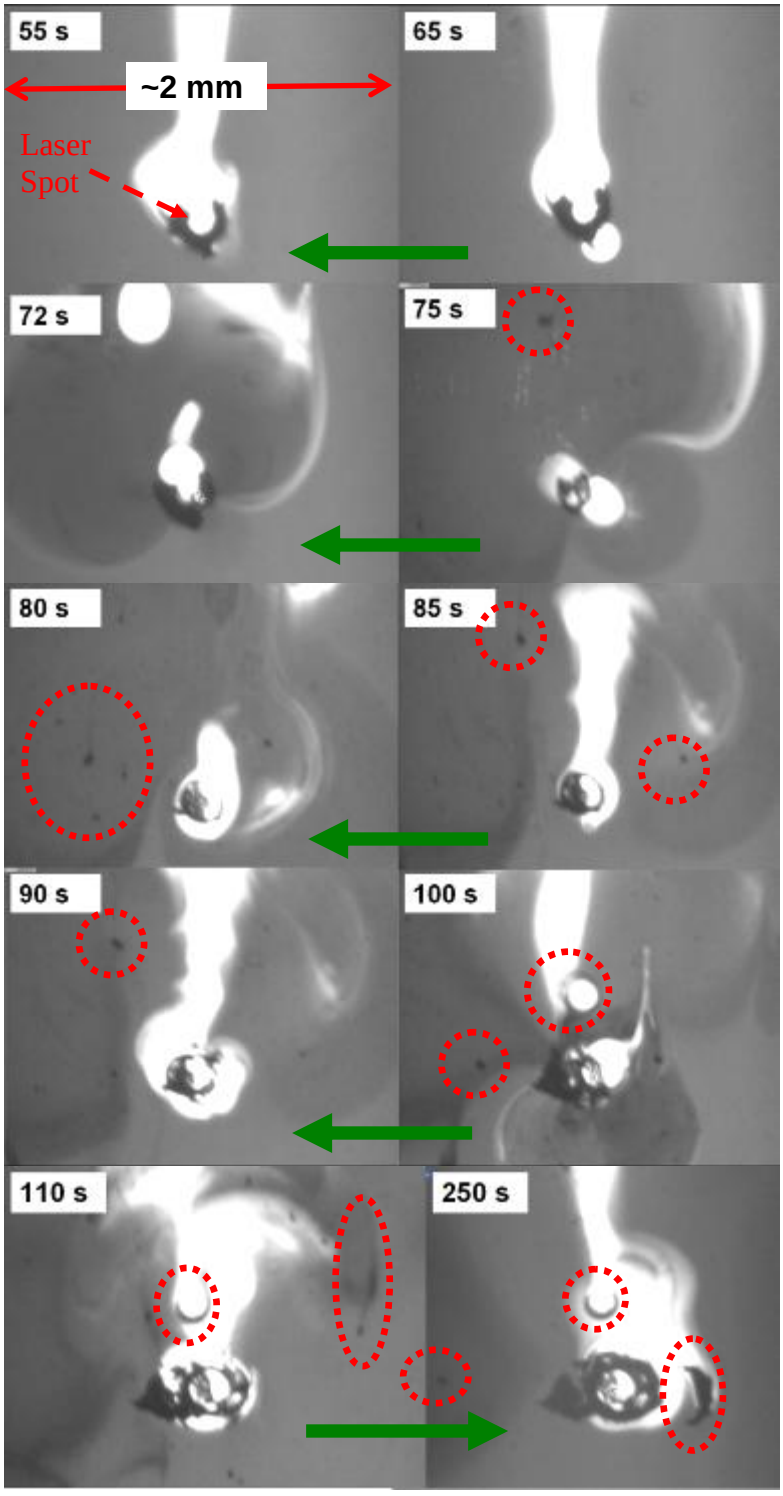
55 s
~2 mm
Laser
Spot
65 s
72 s
75 s
80 s
85 s
90 s
100 s
110 s
250 s

Figure 61. Time-lapse photos of a 0.1%v graphite nanofluid exposed to a laser irradiance of ~770 W/cm^2 –arrows indicate direction of motion via a manual translating stage @ 1-3 mm/s (the laser spot is in the same position in all frames). Dashed circles indicate separated high concentrations of graphite nanoparticles.

Third, it is unclear from the images how much vapor is leaving the heated area. Again, in macro-scale boiling, vapor bubbles form, grow, and leave the surface. In Figure 59 a bubble stays in the same spot even though buoyancy forces (calculated to be ~ 0.12 μN) should cause it to rise. Since the bubble can grow up to 500 μm in diameter in some cases, the 100-μm-thick cuvette could create a restrictive surface tension force on the bubble. Presumably, the vapor would condense in the sub-cooled surrounding liquid after the laser is turned off. At that point, the reduced restricting force would allow the bubble to rise. Alternatively, tiny (irresolvable) bubbles could be continuously leaving the laser spot. If so, the main bubble could be the generation site for a continuous flow of fluid in as liquid and out as micro-bubbles. In either case, we observe a larger final volume of vapor leave just after the laser is turned off. It should be noted that high temperature gradients should also cause particles migration away from hot regions via thermophoresis.

Additional interesting phenomena were seen in the graphite nanofluid when the laser spot was moved through the sample. The series of images in Figure 61 show dynamic bubble expansion and contraction takes place when the sample is translated in a direction orthogonal to the incident laser beam. Since it

takes some time for vapor to form in the nanofluid *and* particle clumps are present, some very chaotic heat and mass transfer is shown. This response was not seen in the control fluids - pure water or the black dye. The next section will discuss how boiling compares between these same fluids.

4.5.5 Volumetric vs. Surface Saturated Boiling

To attempt to compare boiling/vapor generation during high-irradiance photothermal conversion of various fluid, another set of controlled experiments was run. In these experiments, fluid samples were contained inside a this section will describe some experiments directed towards comparing surface and volumetric absorption. To achieve this, a test was run where near-saturation conditions were held for a small 2mm X 2mm x 35mm test cell. This test cell was coated with a black backing for all trials. Therefore, regardless of the fluid sample, any un-reflected light is absorbed either in the fluid or on the backing. Note: these are the same conditions as modeled with Siemens NX 7.5 (as described in section 3.5). Figure 62 shows a magnified view of the test cell for this experiment.

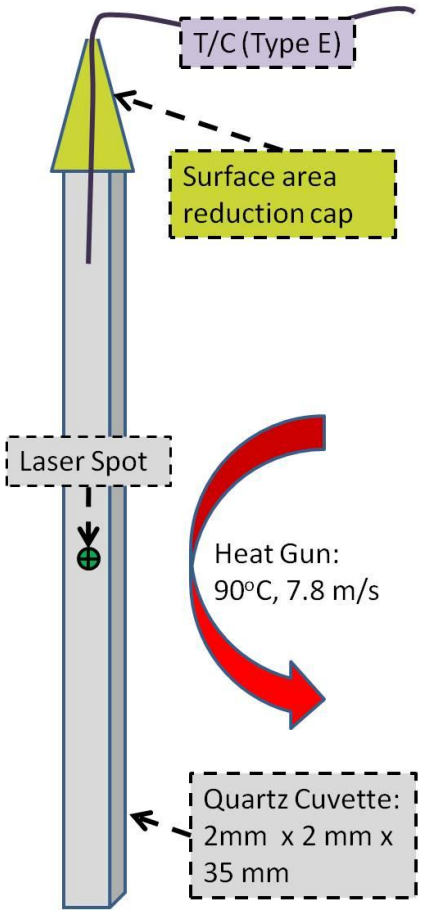

Figure 62. Saturated liquid, quasi-steady state boiling test cell

As can be seen in the figure it consists of several major components. A test sample, an open (to the environment) cap, a heat gun to keep the sample near saturation, a laser input, and a thermocouple inside the same. Exterior to these components, the experiments has the parallel and perpendicular infrared and visual monitoring equipment described in previous sections. Thus, before, during, and after the laser is directed towards the sample, temperatures and motions inside the cuvette can be monitored.

The main goal of this experiment, however, was to run several materials with various samples to see which ones can generate the most vapor. As noted in the first paragraph all the samples are black backed so any un-reflected light is absorbed. Also, the test procedure and test conditions were meticulously controlled to achieve the same conditions every trial. Table 6 describes the proceedure used for each trial.

Table 6. Photothermal saturated boiling test procedure

Time	Action
0 seconds*	Turn ON heat gun
60 seconds*	Turn ON laser
360 seconds*	Turn OFF heat gun and laser
420 seconds*	Weigh Sample on Mettler Toledo AL204

*Note: Thermocouple readings are taken every 30 seconds

Many materials were used in these tests: pure water, Pylam AB1 dye, graphite, silver, copper, multiwalled carbon nanotubes, and nickel. For each material four to six different concentrations were used in these tests. Therefore, a large amount of data covering many orders of magnitude in volume fractional loading was used. In each test the cuvette + sample was weighed before and after to determine the amount of vapor generated from boiling. Figure 63 shows these results as a function of volume fraction. Important note: the numbers in Figure 63 are corrected for evaporation by subtracting the average mass lost if the laser is

not used. That is, several tests with the fan only were used to find the amount of evaporation mass loss. This component is presumed to be constant and is taken out of the following results.

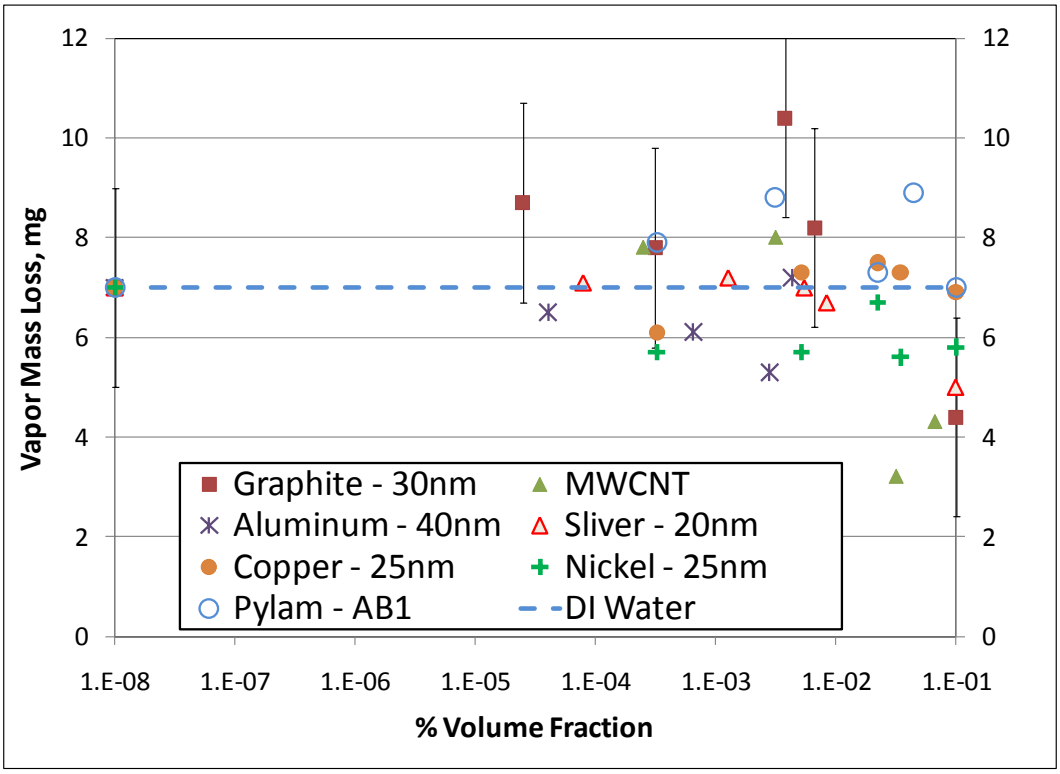

Figure 63. Vapor generated (i.e. boiled off) during the experiment as a function of particle volume fraction for various fluids with a black backing.

Figure 63 shows that there are several 'volumetric' fluids including the Pylam black dye which appear to beat water with a black backing. On the other hand, Figure 63, also shows that there are large errors in this experiment - up to 2 mg. This is denoted by the sample error bars which are shown on the graphite data points. Figure 63 seems to bunch up all the data points towards the higher

volume fractions. However, if we plot these results in terms of percent of incident light transmitted (to the black backing), the results are a lot more evenly distributed. Figure 64 shows these same data points on what is effectively a logarithmic scale via Beer's law.

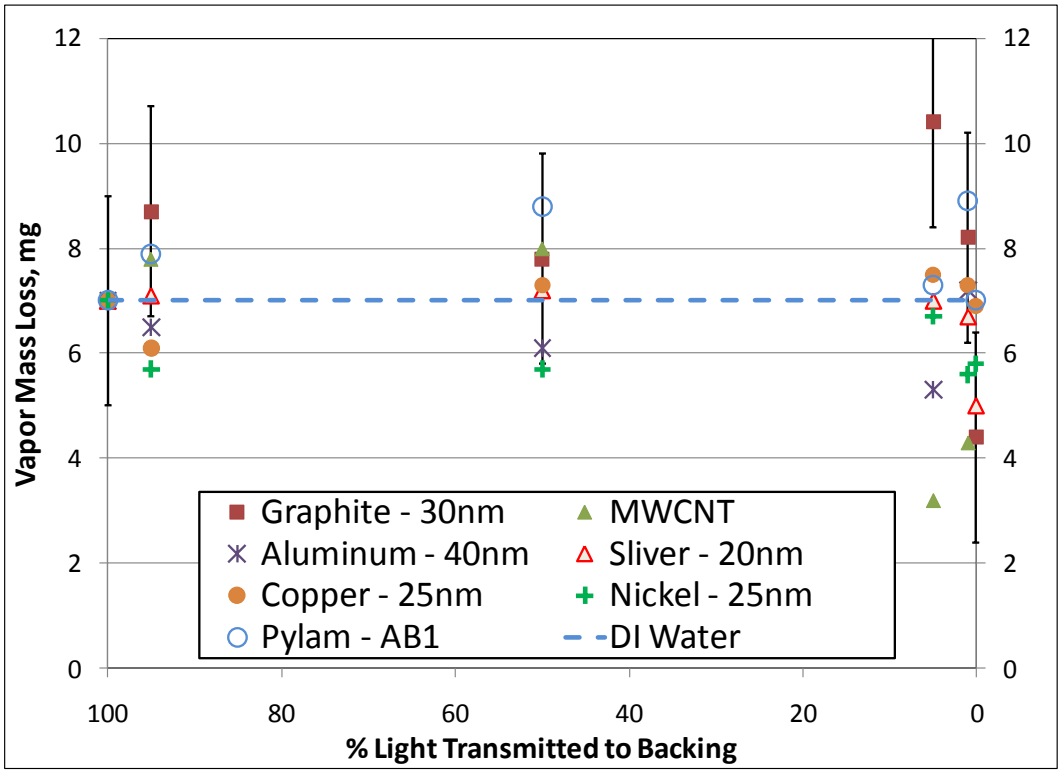

Figure 64. Vapor generated (i.e. boiled off) in the experiment as a function of the percentage of incident light that is transmitted to the black backing.

In Figure 64, we can see that for many materials (excepting DI water which is constant) there is a maximum vapor generation which is between 100% and 0% transmission. For nickel and copper, however, at almost every level of % transmission the results appear to be worse than a simple black backing. It is possible that this negative result is related to scattering. That is, some of the light

is actually being scattered by these metals which decreases the amount of energy that can go into creating vapor. On the whole, for this set of experiments, the large errors makes it difficult to conclude much of anything beyond general trends.

Looking at all of the experiments of this chapter, however, several fascinating thermal/phase change phenomena are demonstrated when nanofluids are exposed to high irradiance continuous-wave laser beams. First, there are several regions of non-uniform nanoparticle concentration in and around the heated area. Second, vapor bubbles form and leave the heated region under sufficient laser light flux. Third, significantly less irradiance is required to cause phase change in some nanofluids as compared to the water base fluid with a black backing or a black dye. Experiments also indicate it may be possible to find an optimal nanofluid that minimizes irradiance necessary to induce phase change. Lastly, fascinating and elaborate fluid dynamics can be produced by translating the test cell.

Our understanding of the complex phenomena that occur (or may occur) in this simple experiment is clearly incomplete, and more research will be needed to fully understand these processes. If possible, measurement of the local temperature and pressure fields will greatly improve our understanding of radiative nanofluid systems. An efficient/optimum nanofluid could be applied to many technologies which require localized heating and/or phase change. In

particular, it may be possible to develop solar collectors which absorb light directly and undergo phase change in a single step. Overall, nanoparticle suspensions are quite versatile and tunable in optical and radiative heat transfer applications. If optimum nanofluids are defined, they could provide some unique and important advantages when exposed to concentrated light energy.

However, it is noticed in Figure 59 that the particles appear to clump/agglomerate as the experiment proceeds. The mechanism for this is unknown, but increased Brownian motion will bring particles into contact more often. Also, as the fluid vaporizes, the graphite particles (with a melting point > 3600 K) are left behind. Thus, the particle density changes pretty dramatically throughout the experiment. For a given laser irradiance (in our case ~770 W/cm^2), the temperature rise can be plotted as a function of particle density. In order to conduct a proof-of-concept test, we use a diode pumped solid state (Coherent - DPSS) laser which produces 130 mW of light energy at a wavelength of 532nm.

CHAPTER 5: APPLICATIONS

The results of the previous chapters imply that a well designed 'solar nanofluid' collectors provides advantages over a surface-based collector and a black dye. Therefore, in this chapter we will apply the findings of chapters 3 and 4 to explore the advantages (if any) of real world solar collectors. In doing this we seek to answer the following questions: Is it possible to achieve the various enhancements mentioned above without adversely affecting capital expense? For a given conceptual design, what improvement is expected compared to a conventional solar thermal collector? These questions are also explored through 'on-sun' (i.e. outdoor) experimentation on a small nanofluid dish collector. Lastly, a simple economic analysis is conducted to illustrate the implications of using a nanofluid collector.

Since there are no commercial nanofluid solar collectors yet, this section will outline our assumptions, reasoning, and choices made in designing one. As mentioned above, nanofluids are a mixture of very small-sized particles and the conventional liquids used in a given application. Therefore, the first design choices to be made are in selecting those two components. Common base liquids in solar collectors are water, heat transfer oil, or molten salt. The choice between these liquids is usually determined by the required operating temperatures. Heat transfer oils are commonly used for medium temperature ranges (100^{o}C-400^{o}C) which are suitable for Rankine thermal cycles, and are our choice for this study.

For efficient solar collection, the particles need to be highly absorptive which limits our study to metallic and graphite particles. We will further limit our options by only selecting particles which are widely available 'off-the-shelf' and are thus made in larger production volumes. For instance, some nanopowders can now be found for around $1,000/kg (Sigma-Aldrich, 2010). Of course gold, platinum, palladium, and other precious metals fit this criterion but are not cost effective. (Note: all $ amounts are given in 2011 US$. Note also, that gold nanopowder is ~$190/g or about five times its bulk price).

As noted above, the volume fraction of nanoparticles in the base fluid must be chosen carefully to get the most out of a nanofluid. If the nanoparticle concentration is too high, all the sunlight will be absorbed in a thin layer near the surface of the receiver – i.e. not volumetrically. If the concentration is too low, a significant portion of the light will be transmitted out of the fluid. Ideally, the least amount of particles needed to effectively absorb light will be used to minimize cost.

5.1. Solar System Efficiency

Looking from a global scale, one can estimate total *system* efficiency in a general concentrating solar thermal collector. This can approximated by taking into all the components in the system which affect efficiency, written as the following:

$$\eta_{overall} = \eta_{optical} \times \eta_{receiver}\left(C, T_{receiver}\right) \times \eta_{tthermal}\left(T_{receiver}, p_T\right) \quad (76)$$

where $\eta_{optical}$ is the optical efficiency, $\eta_{receiver}$ is the receiver efficiency, and $\eta_{thermal}$ is the power block efficiency (including heat exchange losses). As noted in the equation, the optical efficiency is a function of many parameters including the concentration ratio, the receiver efficiency is a function of the concentration ratio and the receiver temperature, the power block efficiency is a function of the receiver temperature and the pressure ratio of the turbine(s). Figure 65 gives a good approximation of the impact that can be made on the overall plant efficiency by increasing operating temperatures. Improving the maximum operating temperature from 870 K (600^{o}C) - the current state of the art - to 1070 K (800^{o}C) means an overall improvement in efficiency of >10%. While this may not sound extremely large, it is significantly more power generation for what is essentially the same power plant. Couple this with the fact that higher temperatures open up the option of using more advanced power cycles, and the impact is dramatic. It is also very probable that higher temperatures make even larger solar thermal power plants possible - i.e. on the order of Gigawatts, with their associated economies of scale. Thus, there is little doubt that high irradiance and solar concentration are very important in a solar thermal power plant. Thus, the remainder of this chapter will discuss only relatively highly concentrated solar energy inputs.

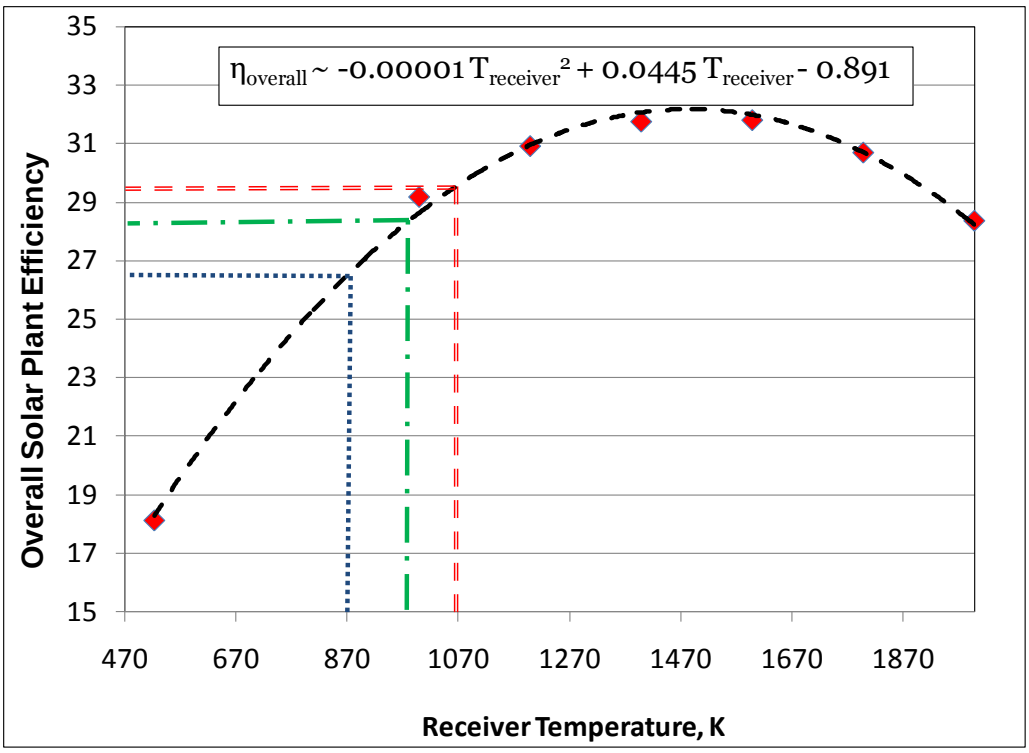

Figure 65. Overall central receiver solar power plant efficiency - based on (Segal and Epstein, 2003).

5.2. Nanofluid Receiver Modeling

To simplify the analysis, though, we only model the effect of nanofluids on the receiver efficiency - since this is the area that will be most affected by the addition of nanofluids. To do so, we will set scale boundaries by considering two plant sizes – 10 MW_e and 100 MW_e. This range is used in order to analyze utility scale power systems, and also to stay in a range where they might feasibly be built, or retrofitted, in the near term. Trough (i.e. linear focus) systems are a poor choice for nanofluids because a relatively large amount of surface area would require modification. This study will consider only relatively high concentration

(i.e. spot focus) schemes of solar thermal electrical generation. This choice was made to ensure that the change from conventional to nanofluid receiver would require only small changes in materials when compared to the entire solar collection system. Figure 66 gives two notional designs of a potential nanofluid receiver - designated A and B. Raw materials needed for this design are steel, high temperature insulation, and possibly glazing (e.g. anti-reflective float glass - see TECHSPEC^{TM} from Edmund Optics (Edmund Optics, 2010)). Receiver A (with glazing) could be oriented vertically or horizontally and operated at pressures well above ambient. Ideally, the cold inlet stream could be directed towards the glazing to improve efficiency and to lance nanoparticles off the glazing to preserve transparency. Receiver B could work in a beam-down concentrator under atmospheric pressure since the fluid is not confined. Receiver B could also be turned on its side where the fluid flow would be a falling film. The advantage of B is that it could avoid the reflective losses of the glazing. Lastly, in Figure 66 C gives a simplified schematic of a conventional power tower solid surface absorber. The conventional power tower receiver is composed of a wire/ceramic mesh used to absorb energy over a finite depth. This type of receiver is sometimes referred to as volumetric absorber, but it must still transfer heat through a solid surface via conduction and convection to the working fluid. That is, the energy must go through at least one intermediate heat transfer step.

All things being equal, a volumetric receiver should provide less resistance in converting sunlight into useful heat.

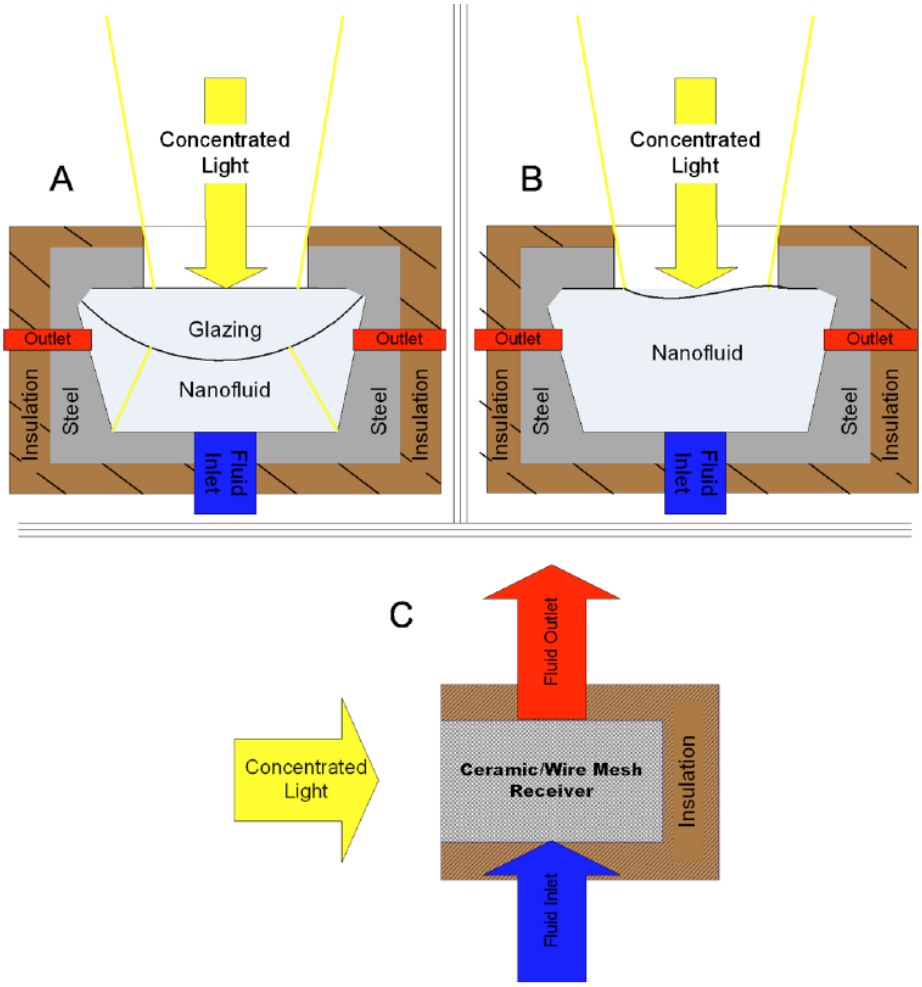

Figure 66. A – Conceptual design of a nanofluid concentrating collector with glazing, B – Conceptual design of a nanofluid concentrating collector without glazing, C – Conceptual drawing of a conventional power tower solid surface absorber.

There are several interesting differences between a conventional receiver and our conceptual nanofluid receiver: 1) The nanofluid receiver may

unavoidably require a transparent glazing to contain high temperature/pressure fluid. However, the glazing material *could* be shaped to employ secondary optics, 2) the nanofluid, by skipping a conduction/convection heat transfer step, could avoid a significant temperature drop and some heat loss, 3) the nanofluid receiver may require more maintenance and/or a somewhat higher capital expenditure, 4) an equivalent solar collector must have more tightly controlled optics, flow conditions, and receiver geometry, 5) thermal/optical properties and thus receiver efficiencies are expected to be different from a surface absorber.

Using the optical properties from previous sections, we can numerically approximate the efficiency of a solar receiver. This is done, as is illustrated in Figure 67, by assuming concentrated light enters from the top of the receiver where it is absorbed/scattered, converted to heat, and carried out by a flowing nanofluid. Some of the light energy is lost to reflection while heat is lost on the boundaries of the receiver due to convection and radiation. A characteristic temperature field inside the receiver is also shown in Figure 67.

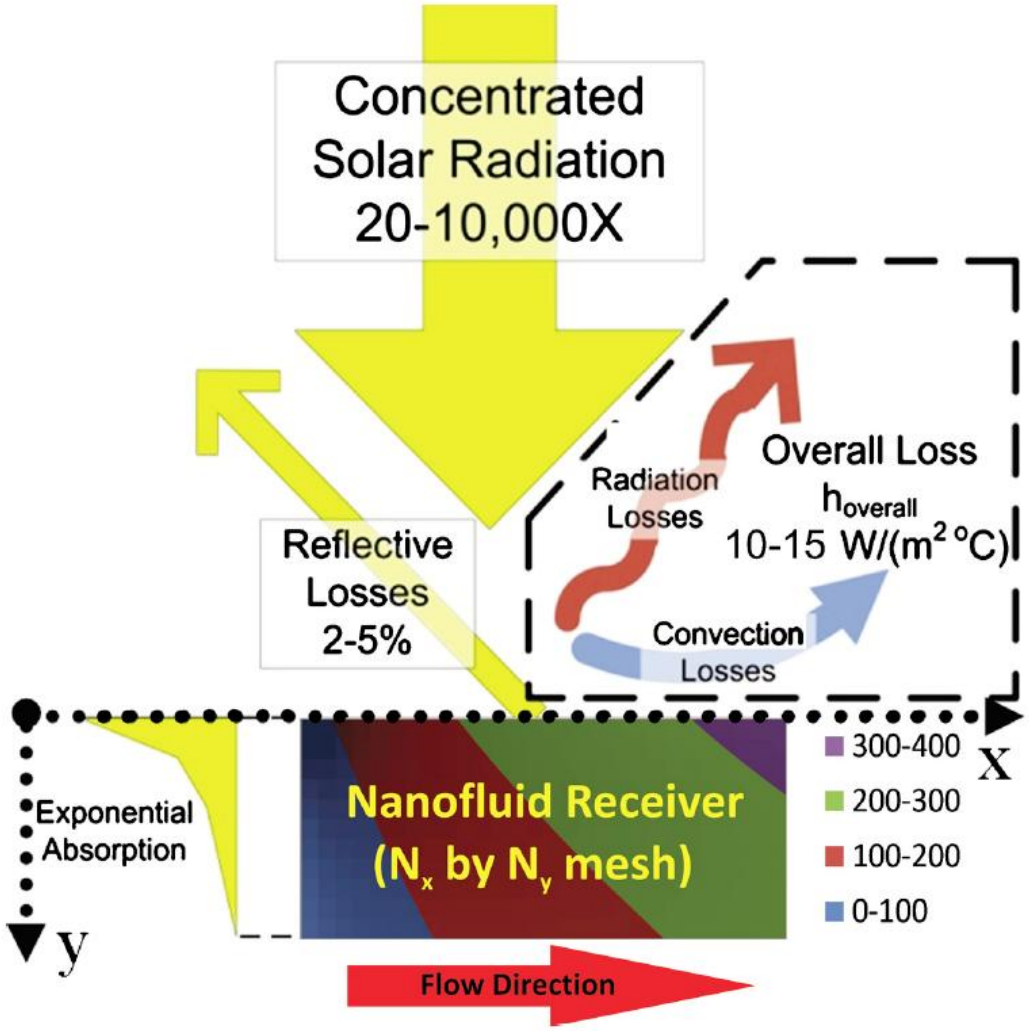

Figure 67. Schematic of conditions used in the numerical model with a characteristic temperature field shown.

With the general model developed, it is simply a matter of conducting a parametric study to examine how the solar receiver and power plant system efficiencies vary. In the following analysis we have chosen to study the following

important independent variables: particle material, particle volume fraction, mass flow rate, and the solar concentration ratio.

We first compare our chosen nanofluids while holding mass flow rate and solar concentration ratio constant - at 180kg/s and 620 suns, respectively. Another important parameter that must be chosen is the reflectivity of the backing material, which in this case was milled aluminum, $\Re_{avg} \sim 0.5$, to match with the experimental work described in the following sections. For these conditions, Figure 68 plots system efficiency versus the percent of transmitted direct normal irradiance - i.e. versus the total percent of solar power left after one pass through the nanofluid.

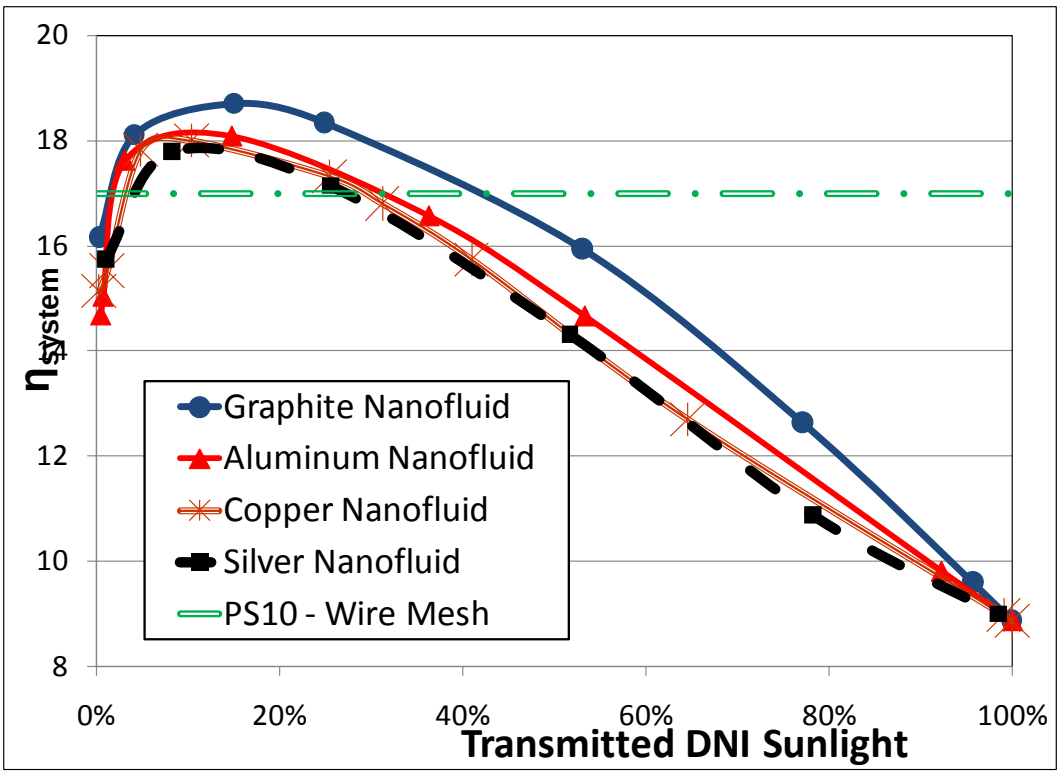

Figure 68. Modeled system efficiencies of graphite, copper, aluminum, and silver nanofluids with the system efficiency of Abengoa's PS10 solar power tower for comparison (Abengoa, 2010).

Figure 68 also shows that minor differences of less than 2 % in system efficiencies are obtained with different nanofluids for comparable sunlight absorption. The differences that are present in system efficiency presumably result from spectral differences in the nanofluid's extinction coefficient and scattering. For example, the extinction coefficient of graphite comes almost entirely from absorption, $\sigma_{a,\lambda} \approx \sigma_{e,\lambda}$. That is, graphite scatters very little incident light and thus it has a slightly higher system efficiency for most conditions. In addition, graphite has a relatively uniform extinction coefficient as a function of

wavelength which also separates it from the metals. Figure 68 shows that there is an optimum nanoparticle volume fraction for each fluid which will achieve maximum system efficiency. In this analysis the optimum point occurs when 85-95% of the incident light is absorbed on the first pass with most of the remainder being absorbed on the semi-absorbing back or as reflected light goes back up through the fluid. In general, absorbing the light **away** from the boundaries - where heat can be lost - provides the best result. The exact nanoparticle volume fraction, however, should be found for individual applications as it depends on parameters such as flow rate, solar irradiance, heat loss conditions, reflectivity of the backing material, receiver geometry, ambient conditions, etc.

As a baseline case, the receiver geometry and approximate operating conditions (i.e. geometry and concentration ratio range) are fixed to be roughly comparable to Abengoa's PS10 power tower in Seville, Spain (Abengoa, 2010). Under normal conditions the PS10 produces about 55 MW thermal power (~11 MWe) with 250 ^{o}C steam at 40 bars (Abengoa, 2010), which is roughly similar to the nanofluid results. To highlight the comparison between our nanofluid model and the PS10 power plant, its system efficiency is plotted as a straight line in figure 6. In the end, the cheapest, stable nanofluid should be the choice for a solar thermal power plant. According to our analysis, in a large-scale system this is likely graphite (at nearly $1/g in bulk) with a volume fraction on the order of

0.001% or less. It should be noted, however, that the price difference between nanoparticles may be negligible with respect to system capital costs.

Now we shall consider the effect of varying the solar concentration ratio and the mass flow rate while holding particle material and volume fraction constant. Figure 69 shows receiver efficiencies as a function of solar concentration ratio. In order to meet 200 ^{o}C, 300 ^{o}C, and 400 ^{o}C outlet temperature constraints, a proper mass flow rate must be found by running the model several times to find each data point. It should be noted that in most cases flow rates end up being in the fully turbulent regime - i.e. Reynolds numbers in the range of 1 x 10^5 to 1 x 10^6. However, pumping power from frictional losses are calculated to be negligible (less than 1% of the power plant's electrical output) since the receiver length is relatively short. Also, an upper limit on temperature was imposed since our base fluid, Therminol VP-1, cannot operate (as a liquid) above 400 ^{o}C. In this analysis 0.001% volume fraction copper nanofluids were chosen based on their approximate optimum point in figure 6. (Note: graphite will be modeled and compared against the experimental results in the next section.)

Figure 69 also shows model results for the pure base fluid (i.e. nearly non-absorbing) with a selective surface 'black backing' under similar receiver operating conditions. The results of Figure 69 illustrate that a nanofluid collector may operate more efficiently than a conventional surface solar collector under optimum conditions - up to 10% higher for solar concentration ratios in the range

of 100 - 1000. As is shown in the figure, the nanofluid and its operating conditions must be chosen carefully or the system may end up operating less efficiently. A nanofluid receiver could also potentially be useful in a direct steam generation system like those described in (Pettit & Sowell, 1976), but phase change was neglected here.

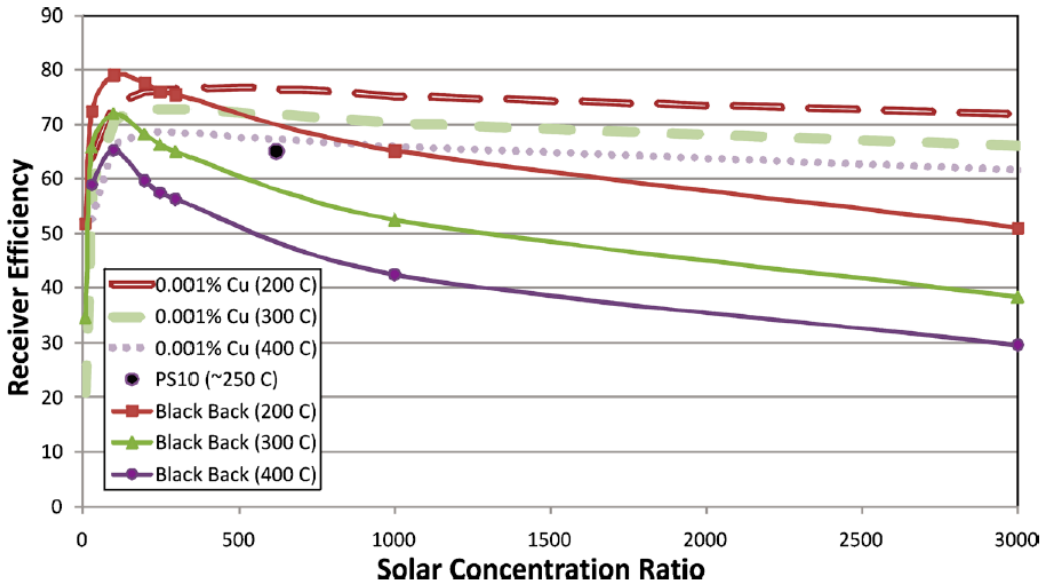

Figure 69. Modeled receiver efficiency as a function of concentration ratio, with f_v = 0.1%, A_R = 264 m^2: Single points - published values (Abengoa, 2010)

Figure 69 also indicates (for a given nanofluid type and receiver geometry) a maximum efficiency is reached at a solar concentrations of about 275-300 (or 275-300 kW/m^2 incoming solar flux). This maximum occurs as a slight positive function of outlet temperature – e.g. a higher outlet temperature leads to peak efficiency occurring at a slightly higher concentration ratio. Again these results

are dependent on the many constant system parameters, but the trends should be similar for other designs.

5.3. Nanofluid 'On Sun' Testing

In order to evaluate some of the predictions of this model, some experiments with a nanofluid dish collector were conducted. Previous work of the co-authors found that for low-temperature solar collectors the numerical model matches quite well with experimental data from a mini flat-plate solar collector (Otanicar, et al., 2010). To explore higher temperature collectors, a dish collector was chosen. The dish was selected because it is easy to work with and because we were able to build the whole collector system cheaply. A tracking/mounting system was designed and built in a few weeks using a graciously donated parabolic dish from the Physics Lab of Lake Havasu. Although this lab-scale dish collector is not directly comparable to the large-scale results found above, we believe the relative comparison between a nanofluid volumetric receiver and its base fluid with a semi-absorbing backing is valuable as validation of the model. Also, we use a relative comparison to divide out the losses present in our experimental system.

The system is composed of three parts: the tracking system, the dish, and the receiver. The tracking system is controlled in one axis throughout the day by two photodiodes connected by a simple control circuit to a step-motor. The

motors adjust when shade from a fin covers one of the photodiodes which keeps the normal axis of the dish parallel to the sun. The second axis of the dish – the tilt angle – is adjusted manually.

The dish is made of polished aluminum and has an intercept area of 0.46m. The manufacturer-quoted average dish reflectivity is >90% - however, this reflectivity is for the ideal flat material - i.e. normal incidence in pristine condition. Thus, in our experiments we expect slightly lower reflectivity.

The receiver was machined from two separate blocks of aluminum which are bolted together with glazing in the center. The thickness (i.e. depth) of the fluid flowing in the receiver is 1 mm. The experimental receiver design has double-paned, 2cm x 2cm, microscope slide glazing. In the modeling results above, the model only included a single pane of clean glazing. For simplicity, each additional glazing can be assumed to be another ~5% loss.

Figure 70 shows images of the dish and receiver used in these experiments. Removed from the receiver are the thermocouples (which measure the heat energy gain) and pressure probes (which determine the flow rate inside the receiver). Temperatures seen inside the receiver were up to 270 ^{o}C. Mass flow rates in the collector were on the order of 1 x 10^{-4} kg/s, giving laminar Reynolds numbers of approximately 15-25 for all steady flow conditions.

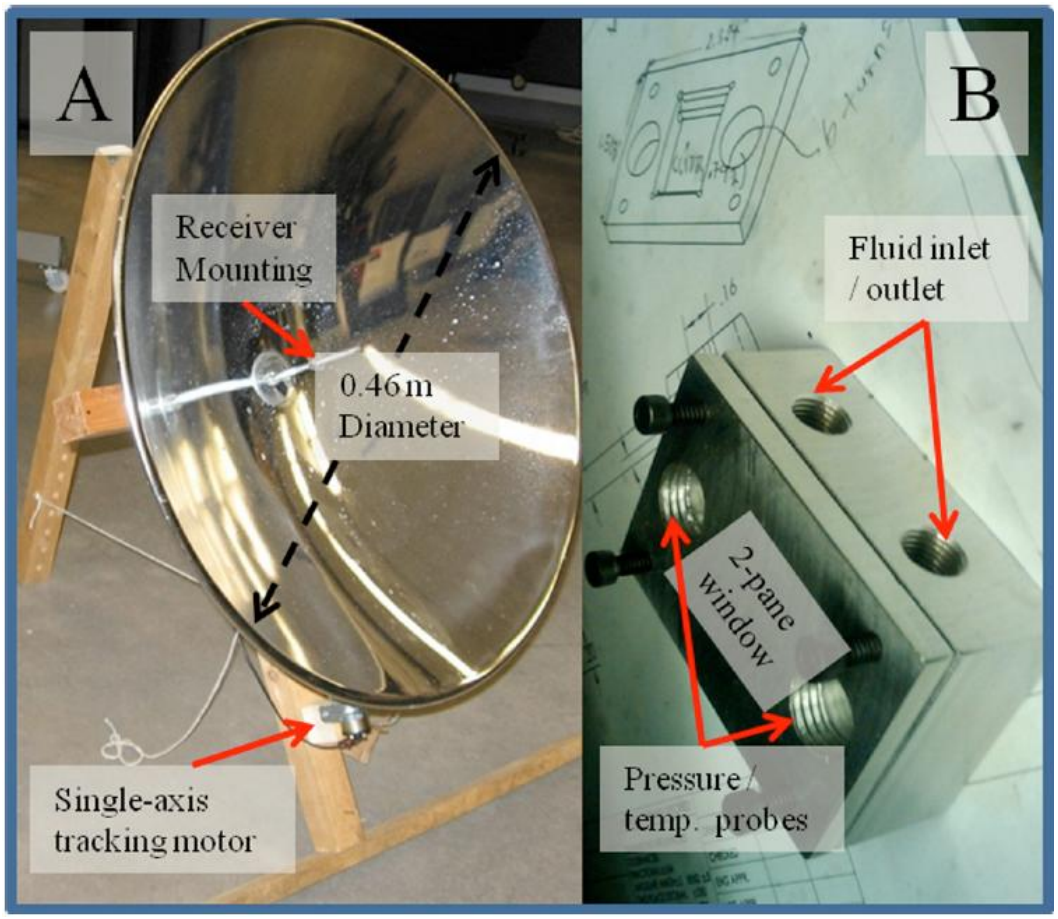

Figure 70. A. Lab-scale single-axis tracking, reflective dish. B. Aluminum machined receiver with instrumentation ports.

The receiver backing was left as machined aluminum which we assumed had a reflectivity around 0.5 since it was a dull finish. Tests with a reflected green laser indicated that this was a reasonable estimate. Further, we know the aluminum backing absorbs about half the incident light because tests with just the base fluid convert sunlight into heat at ~28% efficiency in our experiments. Reflection off the front glazing, reflections from the aluminum backing

transmitted out of the fluid, and heat losses presumably add to give base fluid efficiency of ~28%.

The base fluid used in these experiments is the same at that assumed in the model, Therminol VP-1 heat transfer oil (Solutia, 2010). Graphite nanoparticles were mixed into the Therminol oil since our analysis showed that they appear to be the cheapest and most efficient solar absorbers. The volume fractions used in this 1-mm deep channel are 0.125% and 0.25%. In these fluids, the particles will be closer to each other than the low volume fractions mentioned above, but we can still use the Rayleigh scattering approximation of the model. Also, in one pass (1 mm) through the collector these volume fractions are expected to absorb > 90% of the incoming solar spectrum, which is very similar to the modeling results above.

The dish collector has a geometric concentration ratio of ~ 400, which is very near the optimum concentration ratio of Figure 69. This concentration ratio is calculated using the measured intercept area of the dish and dividing by the measured spot size (found using burn paper). During testing the dish experienced direct normal irradiances of 800-950 W/m^2 (Tempe, AZ - from (NREL, 2010b)). It should also be noted that data of the global irradiance were also recorded periodically during the experiments. For this, a pyranometer from Matrix, Inc. (an MK 10 Sol-A-Meter) was used to confirm the data from (NREL, 2010b)). . At its peak, the nanofluid dish tracker achieved a maximum solar-to-thermal

energy conversion efficiency of ~34% at outlet temperatures ~250^{o}C. This is about 20% higher than the receiver with the Therminol oil alone under similar conditions. Figure 71 shows the steady-state efficiencies achieved in these experiments. Since we did not know the exact optical efficiency for the dish collector (e.g. spectral reflectivity of the dish and other components as well as shadowing from components), efficiencies are plotted as a ratio of the nanofluid steady-state thermal efficiency to the base fluid's steady-state efficiency under similar conditions. Figure 71 shows these results with error bars determined by a simple error propagation analysis.

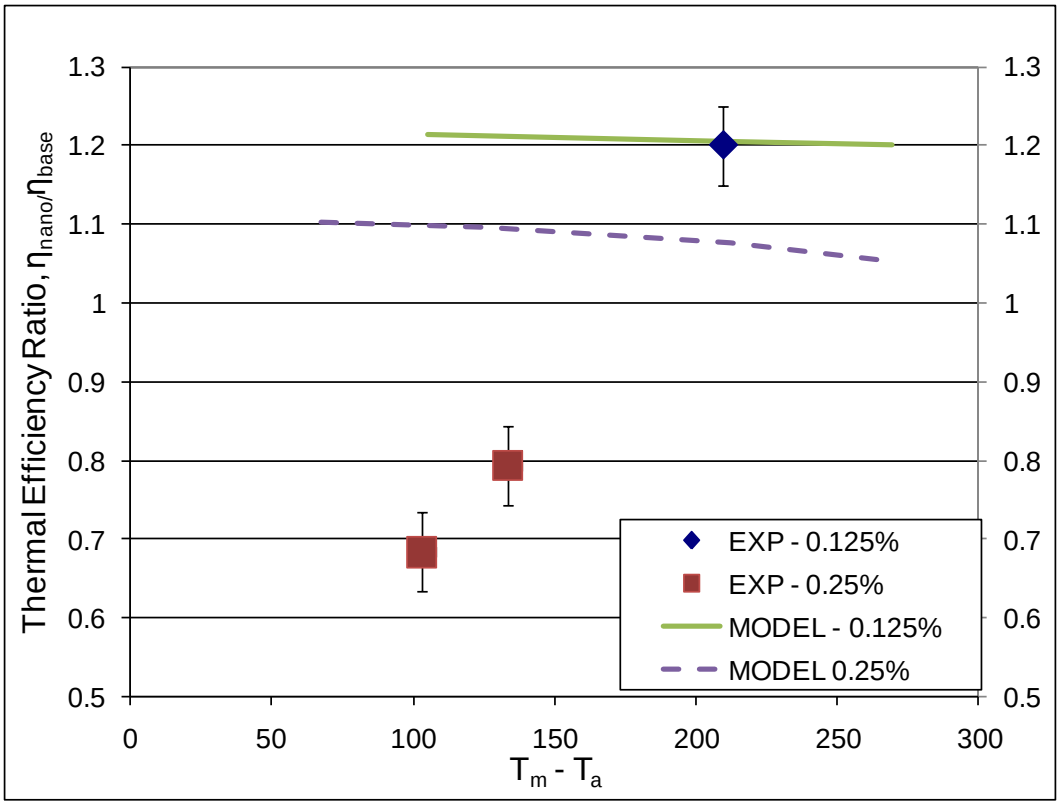

Figure 71. Normalized steady-state efficiencies for conventional collectors (lines) compared to our outdoor lab-scale dish experiments (data points).

These experiments indicate that nanofluids can only provide an advantage if the composition is chosen carefully and the fluid/tracking system is precisely controlled. For higher volume fractions >0.125% we had a difficult time achieving relative efficiencies near what the model predicted. One possible reason for poor results is that the nanofluids were unstable (i.e. the particles agglomerate, become large/heavy and settle out) at higher volume fractions. Another possible reason is that in a more concentrated nanofluid light will be absorbed in a thin upper layer of the fluid where it can easily transfer back out of

the receiver. While the model should predict thermal emission for an ideal, stable nanofluids, significant deviations are possible with high solar fluxes if particle agglomeration occurs. On the other hand, for lower volume fractions, our experiments found significant efficiency improvements which matched quite well with the model. A 0.125% volume fraction of graphite resulted in approximately an 11% improvement in steady-state efficiency over the base fluid.

Overall, our limited preliminary data shows similar efficiency improvements are possible in when the fluid is chosen and controlled carefully. However, if the nanofluid becomes unstable or if tracking is inaccurate, a nanofluid collector can become very inefficient indeed.

5.4. Economic Implications

It is estimated that less than 30kg or 300kg of nanoparticles would be needed in a 10MWe or 100MWe solar thermal power plant, respectively. Thus, at a nanoparticle price of ~$1,000/kg (MTI, 2011) (as mentioned above), the cost increase of using a nanofluid would still be less than 0.1% of the total plant capital investment - assuming $5/W (Kaplan, 2008). The cost of changing receivers was not estimated, but no exotic materials or fabrication methods would be needed to produce a large-scale nanofluid receiver. In fact, a receiver made of anti-reflective glass, steel, and insulation may actually be cheaper than a ceramic

mesh receiver. Table 7 gives an estimate of the costs for different nanofluid mixes.

Table 7. Solar thermal nanofluid comparison table (*assumes pure water base - where water + stabilizers = $0.5/L)

Type	**Graphite**	**Al**	**Copper**	**Silver**	**Gold**
Particle, %v	0.0004	0.001	0.004	0.004	0.004
Commercially Available	Yes	Yes	Yes	Yes	Yes
Surfactant, %v	0.5	0.25	0.25	0.25	0.25
1M NaOH, %v (achieve pH 9-10)	0.003	0.003	0.003	0.003	0.003
Sonication Time, min	45	30	30	30	30
Collector Depth, cm	10	10	10	10	10
~ Cost, $/L	**0.52**	**0.64**	**1.85**	**3.65**	**233**

It should be noted that operation and maintenance costs are more difficult to estimate. We believe (from observation of stagnant nanofluids stored in glass containers for up to 18 months) that very little extra maintenance would be required inside a nanofluid receiver in the short term. That is, a properly prepared nanofluid in a closed loop could be relatively stable and should not need replacement. Good design, operation, and maintenance (with occasional cleaning) could keep interior surfaces transparent and free of particle deposits. A closed system should also prevent any added environmental costs during the nanofluid's use phase. However, long-term studies have not been conducted and nanofluid leak/spill prevention and/or clean-up could be costly. For instance, re-

mixing of the nanofluid and cleaning of optical surfaces may be necessary on a regular basis, which could require specialized equipment. Expenses beyond the initial capital investment are not estimated in this study.

For simple economic comparison, we will conservatively assume an optimized nanofluid receiver can be about 5% more efficient than a conventional one. To demonstrate the advantage of this small change, Figure 72 (A) gives a comparison of yearly electricity generation between a conventional power plant with the characteristics of Abengoa's PS10 and a similar plant with a nanofluid receiver. That is both receivers have a solar concentration ratio, 620, receiver area, 265 m^2, outlet temperature, 250^oC, and power block efficiency, 27%, similar to the PS10. Both systems assume a capacity factor of 85% for the solar resource available at the given locations in Figure 72. In other words, we conservatively assume maintenance or other factors will take the plant out of service for 15% of the sunny hours. Thus, the only difference between the two systems is that the receiver is operating 5% more efficiently.

The locations in Figure 72 were chosen because they cover a wide range of solar resource conditions. As such, the results range from Seattle, WA to Tucson, AZ which, on average receive 2.9 to 7 kWh/m^2 of direct normal incident solar energy per day - as given by NREL for 2-axis trackers (NREL, 2010a). Comparison of different locations merely demonstrates that any enhancement

from a nanofluid receiver would become even more advantageous for areas with higher incoming solar energy.

Figure 72 (B) puts the comparison in monetary terms (assuming sale of electricity at 10 cents/kWh) and scales it up to a 100MW_e, commercial-sized plant. Again, a conservative power block efficiency of 26% was used, but for the larger scale plant we assume that 90% of the solar resource could be utilized. Even with conservative assumptions, this kind of enhancement adds nearly $3.5 million to the yearly revenue of a large plant - which could take about two years off the simple payback time of the plant (assuming $5/Watt, installed (Kaplan, 2008)). If peak prices and carbon credits are taken into account, a nanofluid receiver would look even more attractive.

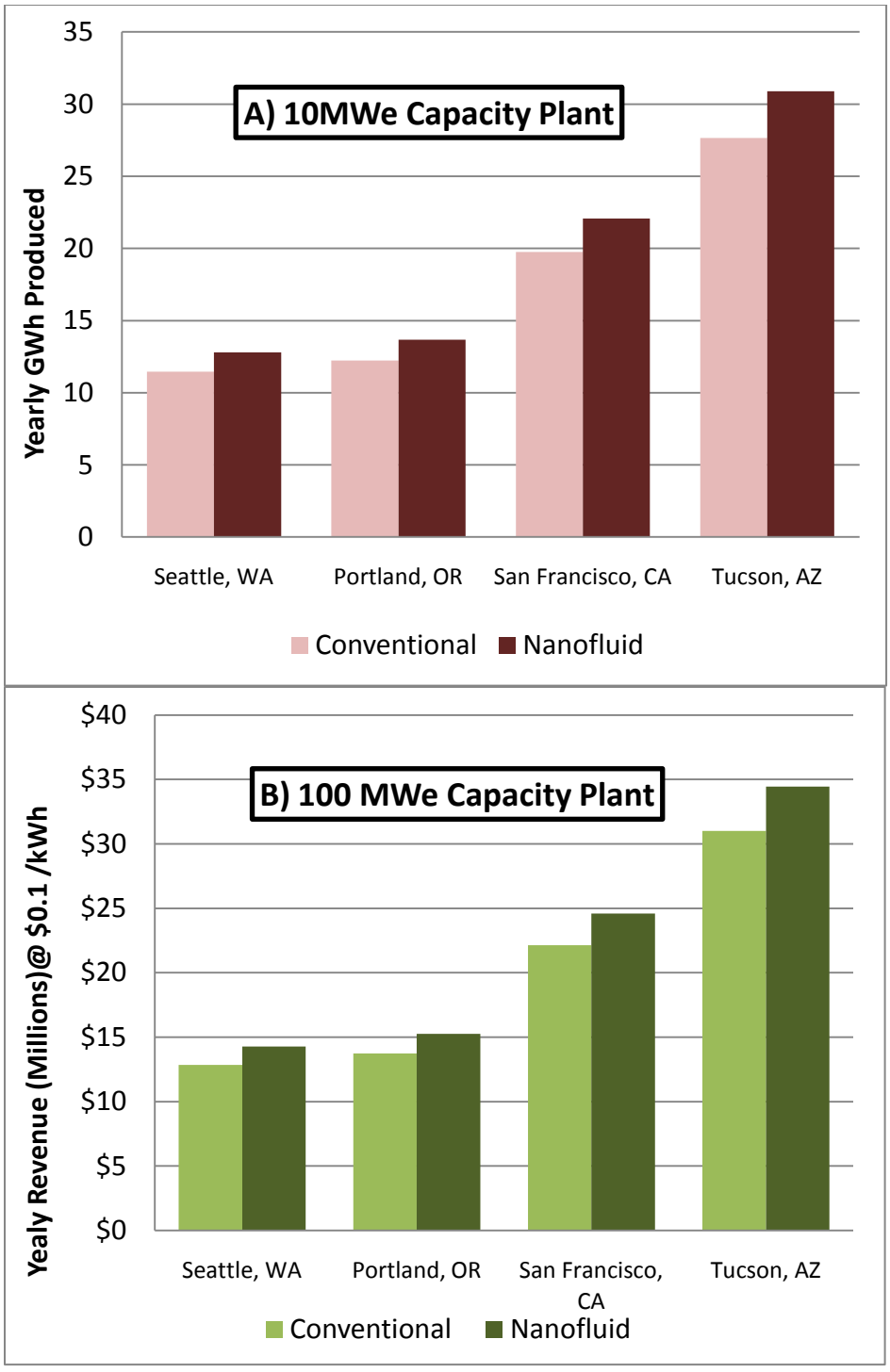

Figure 72. A) Comparison of yearly electricity generation for a plant rated at 10 MW_e, and B) Comparison of estimated revenues for a 100MW_e commercial scale plant.

Overall this analysis is considered to be a conservative, simplified analysis of how a nanofluid-based concentrating solar thermal system would compare to a conventional one. Based on the results of this study, nanofluids have excellent potential for power tower solar thermal power plants. Efficiency improvement on the order of 5-10% is possible with a nanofluid receiver. Ideally, these enhancements could be realized with very little change (in terms of materials, system design, and initial capital investment) to the entire solar thermal system.

Fundamental differences in volumetric absorption versus solid surface absorption drive this enhancement in thermal efficiency for a power tower solar plant. It should be noted, however, that nanofluids are not expected to be suitable for dish or trough solar thermal systems at this time, but further optimization (or cost reductions) might expand their range of applicability. In this study a particular nanoparticle material, shape, and some characteristic operation temperatures were chosen using engineering judgment, but further optimization is possible. It is expected that additional improvements could be made by tailoring the optical and thermal properties of the nanofluid more closely to specific system conditions. This also demonstrates that as solar thermal power plants move to larger scale (in good resource sites) nanofluid receivers show even more potential. A simple economic estimation shows that a 100MW_e nanofluid thermal plant

(operating in Tucson, AZ) could add $3.5 million to the yearly revenue of large scale plants under favorable conditions.

CHAPTER 6: CONCLUSIONS

This research has established the importance of finding new solar thermal technologies to meet economic, environmental, and social needs for society. The United States, being the pioneer in research and development of solar technologies still has plenty of opportunity to lead (and profit) in this market - which is potentially 100s of billions of dollars per year. The United States has a huge, largely untapped solar resource - 500 times our current energy usage. Since solar energy generates no emissions while in operation, this vast economic opportunity helps address local and global environmental challenges. Solar energy also improves quality of living by creating cleaner, greener cities, local jobs for installation and service, urban renewal and rural development, and it insures stably priced, reliable power (Astralux, 2011).

This research has also indicated that one possibly advantageous way to improve solar thermal technology is to employ nanofluids. If designed correctly, solar nanofluids can enhance convective, conductive, phase change[1], and radiative heat transfer - specifically volumetric photothermal conversion is enhanced. Of course, at extremely low volume fractions all but the photothermal conversion enhancements will be negligible, according to classical models. That is, with small particle additions, only small enhancements in properties like thermal

[1] Critical heat flux can be improved 30-300% as noted in section 4.3.4 - only ~30% was seen in this work.

conductivity are expected. Nonetheless, it was shown that most of these benefits can be achieved without significant pumping power or even cost increases.

This research has presented models which are simple, yet accurately predict nanofluid properties and performance for many test conditions. Specifically, a simple additive model of the base fluid extinction coefficient with the nanoparticle field extinction coefficient was developed to determine the extinction coefficient of promising solar nanofluid mixtures. Further, the numerical modeling work conducted in this research matches will with laboratory and 'on sun' testing of nanofluids.

Nanofluids were shown through experiments to increase boiling heat transfer by up to 10% for hot wire pool boiling - as compare to baseline fluid without nanoparticles. Nanofluids were also shown to undergo volumetric phase change at lower levels of irradiance than pure base fluids with black backing or black dyes which had similar absorption properties. Lastly, nanofluids have unexpectedly lower volumetric boiling heat transfer than base-fluids when compared to surface boiling heat transfer coefficients of their base fluids. One explanation for this is that there may be radiative losses from very high local temperatures around individual nanoparticles or nanoparticle agglomerates. Extremely high temperatures were recorded using infrared thermography as presented in section 4.4.

Overall, this research indicates than nanofluids are a promising medium for solar collection and for use in some thermal energy systems (Rankine cycles, absorption cooling, water purification, ethanol distillation, etc.). Importantly, nanofluids show particularly interesting behavior for applications where phase change is necessary. That is, absorbing nanofluids could be exploited to drive phase change with light energy ***volumetrically***, as opposed to conventional solar thermal systems in which a solid surface absorbs the sunlight and then transfers heat to the working fluid. Eliminating this additional heat transfer step makes volumetric radiative absorption potentially more efficient than conventional solar thermal collectors. To the author's knowledge this work is the first to explore this concept, albeit several studies have been directed towards using nanofluids for transient hyperthermia cancer treatments. Application to solar energy, which require steady state absorption of light, are only now beginning to be explored.

This manuscript indicates that up to 10% improvements in receiver efficiencies are possible, which could add up to $3.5 annually to a commercial solar power plant's (100 MW_e) revenue. Before these benefits can be realized in a real, large-scale system, however, there are many other engineering problems that need to be addressed.

CHAPTER 7: FUTURE WORK

The analytical, numerical, and experimental work presented in this manuscript shows and determines the potential for using nanofluids as concentrated solar thermal energy harvesting mediums. There are still many questions and further improvements that can be anticipated with these novel heat transfer fluids. These include, but are not limited to the following:

1. Full optimization: can different shapes, mixtures, and configurations be defined with achieves a true absolute optimum in performance for a given application.

2. Commercial-scale systems: Since this work was only in a prototype stage, several long-term tests and scaled-up tests will need to be conducted before these fluids can be put in commercial application. For example, long term thermal cycling and materials compatibility issues need to be addressed.

3. Stabilization treatments: The present research does not present a definite solution of how to make stable fluids at very high temperatures. In fact, the methods of preparing nanofluid used in this research (adding SDS or TWEEN surfactants) will definitely fail at high temperatures.

4. Catalytic nanoparticles: Can these nanoparticles be made of materials which would allow waste such as CO_2 gas to generate liquid fuels? Current work at Arizona State exploring this concept's feasibility.

5. Nanoscale studies: Since the equipment used in this study did not have good enough resolution to observe nanoparticles under heated conditions or the highly transient behaviors of some of transient photothermal conversion, a significant amount of future work could go into these efforts. It is expected that equipment such as atomic force microscopy, electron microscopy, and other advanced optical techniques will significantly add to our understanding of nanofluidic systems. (Kleinstreuer & Feng, 2011)

REFERENCES

Abengoa. (2010). Solutions to Climate Change :Power Tower Plants.

Andresen, P., Bath, A., Groger, W., Meijer, G., & Meulen, J. J. (1988). Laser-induced fluorescence with tunable excimer lasers as a possible method for instantaneous temperature field measurements at high pressures : checks with an atmospheric flame. *Applied Optics*, *27*(2), 365-378.

Astralux, S. (2011). Non-Energy Benefits of Solar. Retrieved May 11, 2011, from http://www.aessolarenergy.com/non_energy_benefits.htm.

Bang, I. C., & Chang, S. H. (2005). Boiling heat transfer performance and phenomena of Al 2 O 3 – water nano-fluids from a plain surface in a pool. *International Journal of Heat and Mass Transfer*, *48*, 2407-2419. doi: 10.1016/j.ijheatmasstransfer.2004.12.047.

Bertocchi, R., Kribus, A., & Karni, Jacob. (2004). Experimentally Determined Optical Properties of a Polydisperse Carbon Black Cloud for a Solar Particle Receiver. *Journal of Solar Energy Engineering*, *126*(3), 833. doi: 10.1115/1.1756924.

Bohren, C. F., & Huffman, D. R. (1998). *Absorption and Scattering of Light by Small Particles (Wiley science paperback series)* (p. 544). Wiley-VCH. Retrieved October 9, 2010, from http://www.amazon.com/Absorption-Scattering-Particles-science-paperback/dp/0471293407.

BP. (2010). Statistical Review of World Energy 2010. Retrieved May 12, 2010, from http://www.bp.com/

Bureau, U. C. (2010). International Data Base. Retrieved 2010, from http://www.census.gov/ipc/www/idb/informationGateway.php.

Carey, V. P. (2007). *Liquid-Vapor Phase-Change Phenomena: an introduction to the thermophysics of vaporization and condensation processes in heat transfer equipment* (2nd ed., p. 600). Taylor & Francis. Retrieved October 9, 2010, from http://www.amazon.com/Liquid-Vapor-Phase-Change-Phenomena/dp/1591690358.

Carslaw, H. S., & Jaeger, J. C. (1986). *Conduction of Heat in Solids* (p. 520). Oxford University Press, USA. Retrieved October 9, 2010, from

http://www.amazon.com/Conduction-Heat-Solids-H-Carslaw/dp/0198533683.

Cengel, Y., & Boles, M. (2010). *Thermodynamics: An Engineering Approach with Student Resources DVD* (p. 1024). McGraw-Hill Science/Engineering/Math. Retrieved April 5, 2011, from http://www.amazon.com/Thermodynamics-Engineering-Approach-Student-Resources/dp/0077366743.

Chang & Chang. (2008). Fabrication of Al2O3 nanofluid by a plasma arc nanoparticles synthesis system. *Journal of Materials Processing Technology*, *207*(1-3), 193-199. doi: 10.1016/j.jmatprotec.2007.12.070.

Chopkar, M., Das, a K., Manna, I., & Das, P. K. (2007). Pool boiling heat transfer characteristics of ZrO2–water nanofluids from a flat surface in a pool. *Heat and Mass Transfer*, *44*(8), 999-1004. doi: 10.1007/s00231-007-0345-5.

Cosgrove, T. (2010). *Colloid Science: Principles, Methods and Applications* (p. 394). Wiley-Blackwell. Retrieved April 6, 2011, from http://www.amazon.com/Colloid-Science-Principles-Methods-Applications/dp/1444320203.

Coursey, J. S., & Kim, Jungho. (2008). International Journal of Heat and Fluid Flow Nanofluid boiling : The effect of surface wettability. *International Journal of Heat and Fluid Flow*, *29*(6), 1577-1585. Elsevier Inc. doi: 10.1016/j.ijheatfluidflow.2008.07.004.

Das, Sarit K, Putra, N., & Roetzel, W. (2003). Pool boiling of nano-fluids on horizontal narrow tubes. *International Journal of Multiphase Flow*, *29*, 1237-1247. doi: 10.1016/S0301-9322(03)00105-8.

Das, Sarit Kumar, Choi, Stephen U S, & Patel, H. E. (2006). Heat Transfer in Nanofluids — A Review. *Heat Transfer Engineering*, *27*(778562169), 3-19. doi: 10.1080/01457630600904593.

DOE. (2008). Renewable Energy Data Book, EERE. *Department of Energy*. Retrieved from http://www1.eere.energy.gov/maps_data/pdfs/eere_databook_091208.pdf.

Duangthongsuk, W., & Wongwises, S. (2009). Heat transfer enhancement and pressure drop characteristics of TiO2–water nanofluid in a double-tube counter flow heat exchanger. *International Journal of Heat and Mass*

Transfer, *52*(7-8), 2059-2067. Elsevier Ltd. doi: 10.1016/j.ijheatmasstransfer.2008.10.023.

Duffie, J. A., & Beckman, W. A. (2006). *Solar Engineering of Thermal Processes* (p. 928). Wiley. Retrieved October 9, 2010, from http://www.amazon.com/Solar-Engineering-Thermal-Processes-Duffie/dp/0471698679.

Eapen, J., Williams, W., Buongiorno, Jacopo, Hu, L.-wen, Yip, S., Rusconi, R., et al. (2007). Mean-Field Versus Microconvection Effects in Nanofluid Thermal Conduction. *Physical Review Letters*, *99*(9), 1-4. doi: 10.1103/PhysRevLett.99.095901.

Eastman, J. a, Choi, S. U. S., Li, S., Yu, W., & Thompson, L. J. (2001). Anomalously increased effective thermal conductivities of ethylene glycol-based nanofluids containing copper nanoparticles. *Applied Physics Letters*, *78*(6), 718. doi: 10.1063/1.1341218.

EconStats. (2010). U.S. Energy Industry Revenues. Retrieved 2010, from http://www.econstats.com/.

Edmund Optics. (2010). Optics and Optical Components. Retrieved from http://www.edmundoptics.com.

EIA. (2010). *International Energy Outlook*. *EIA* (Vol. 484). Retrieved from www.eia.gov/oiaf/ieo/index.html.

Electronics, M. (2011). Resistor Products. Retrieved May 9, 2011, from http://www.mouser.com/.

Gerardi, C., Buongiorno, Jacopo, Hu, L.-wen, & McKrell, T. (2011). Infrared thermometry study of nanofluid pool boiling phenomena. *Nanoscale Research Letters*, *6*(1), 232. Springer Open Ltd. doi: 10.1186/1556-276X-6-232.

Gilbert, R., & Perl, A. (2010). *Transport Revolutions: Moving People and Freight Without Oil* (p. 448). New Society Publishers. Retrieved November 12, 2010, from http://www.amazon.com/Transport-Revolutions-Moving-Freight-Without/dp/0865716609.

Griffith, P. (1956). *Bubble Growth Rates in Boiling*. *Growth (Lakeland)* (pp. 1-38).

Gueymard, C. (2001). Parameterized transmittance model for direct beam and circumsolar spectral irradiance. *Solar Energy*, *71*(5), 325-346. doi: 10.1016/S0038-092X(01)00054-8.

Hecht, E. (2001). *Optics* (4th ed., pp. 1-680). Addison Wesley. Retrieved May 9, 2011, from http://www.amazon.com/Optics-4th-Eugene-Hecht/dp/0805385665.

Heinberg, R. (2010). *Peak Everything: Waking Up to the Century of Declines* (p. 240). New Society Publishers. Retrieved November 12, 2010, from http://www.amazon.com/Peak-Everything-Waking-Century-Declines/dp/0865716455.

Hielscher. (2011). Ultrasonic devices for liquid processing. Retrieved May 12, 2011, from http://www.hielscher.com/ultrasonics/products.htm?gclid=CKLy_9nO2agCFQEKbAodeAd3Ig.

Hong, T.-K., Yang, H.-S., & Choi, C. J. (2005). Study of the enhanced thermal conductivity of Fe nanofluids. *Journal of Applied Physics*, *97*(6), 064311. doi: 10.1063/1.1861145.

Hottel, H. C., & Sarofim, A. F. (1967). *Radiative Transfer (McGraw-Hill Series in Mechanical Engineering)* (p. 520). McGraw-Hill. Retrieved May 9, 2011, from http://www.amazon.com/Radiative-Transfer-McGraw-Hill-Mechanical-Engineering/dp/B0006BOZ9K.

Hunt, A. J. (1978). *Small Particle Heat Exchangers*.

Hwang, Y., Lee, J.-keun, Lee, J.-ku, Jeong, Y.-man, Cheong, S.-ir, Ahn, Y.-chull, et al. (2008). Production and dispersion stability of nanoparticles in nanofluids. *Powder Technology*, *186*, 145 - 153. doi: 10.1016/j.powtec.2007.11.020.

Incropera, F. P., DeWitt, D. P., Bergman, T. L., & Lavine, A. S. (2006). *Introduction to Heat Transfer* (p. 912). Wiley. Retrieved May 2, 2011, from http://www.amazon.com/Introduction-Heat-Transfer-Frank-Incropera/dp/0471457272.

Industries, M. W. (2011). Resistance Wire. Retrieved May 9, 2011, from http://www.mwswire.com/pdf_files/mws_tech_book/resistance_wire.pdf.

Jackson, J. E. (2007). *Investigation int the Pool-Boiling Characteristics of Gold Nanofluids*.

Jasco. (2011). UV-Vis/NIR Spectrophotometer V-670. Retrieved from http://www.jascoinc.com/Libraries/Product_Spec_Sheets/Leaflet_V670.sflb.ashx.

Jeong, Y., Chang, W., & Chang, S. (2008). Wettability of heated surfaces under pool boiling using surfactant solutions and nano-fluids. *International Journal of Heat and Mass Transfer*, *51*(11-12), 3025-3031. doi: 10.1016/j.ijheatmasstransfer.2007.09.023.

Kaplan, S. (2008). *Power Plants : Characteristics and Costs*. *CRS* (pp. 1-108). Retrieved from http://www.fas.org/sgp/crs/misc/RL34746.pdf.

Karni, J., Kribus, a, Rubin, R., & Doron, P. (1998). The "Porcupine": A Novel High-Flux Absorber for Volumetric Solar Receivers. *Journal of Solar Energy Engineering*, *120*(2), 85. doi: 10.1115/1.2888060.

Kearney, D. (2004). Engineering aspects of a molten salt heat transfer fluid in a trough solar field. *Energy*, *29*(5-6), 861-870. doi: 10.1016/S0360-5442(03)00191-9.

Keblinski, P., Cahill, D. G., Bodapati, A., Sullivan, C. R., & Taton, T. A. (2006). Limits of localized heating by electromagnetically excited nanoparticles. *Journal of Applied Physics*, *100*(5), 054305. doi: 10.1063/1.2335783.

Keblinski, P., Prasher, R., & Eapen, J. (2008). Thermal conductance of nanofluids: is the controversy over? *Journal of Nanoparticle Research*, *10*(7), 1089-1097. doi: 10.1007/s11051-007-9352-1.

Kim, D. K., & Kim, M. H. (2007). Surface Deposition of Nanoparticles During Pool Boiling of Nanofluids and its Effects on CHF Enhancement Using Nanofluids. *ICNMM2007-30071*.

Kim, H., Kim, J, & Kim, M. (2007). Experimental studies on CHF characteristics of nano-fluids at pool boiling. *International Journal of Multiphase Flow*, *33*(7), 691-706. doi: 10.1016/j.ijmultiphaseflow.2007.02.007.

Kim, H. D., & Kim, M. H. (2007). Effect of nanoparticle deposition on capillary wicking that influences the critical heat flux in nanofluids. *Applied Physics Letters*, *91*(1), 014104. doi: 10.1063/1.2754644.

Kim, J.H., & Kim, K. H. (2004). Pool Boiling Heat Transfer in Saturated Nanofluids. *IMECE04*.

Kim, S., Bang, I., Buongiorno, J, & Hu, L. (2007). Surface wettability change during pool boiling of nanofluids and its effect on critical heat flux. *International Journal of Heat and Mass Transfer*, *50*(19-20), 4105-4116. doi: 10.1016/j.ijheatmasstransfer.2007.02.002.

Kim, S.J., Bang, I.C., Buongiorno, J., Hu, L. W. (2007). Study of pool boiling an critical heat flux enhancement in nanofluids. *Bulletin of the Polish Academy of Sciences, Technical Sciences*, *55*(2), 211-216.

Kleinstreuer, C., & Feng, Y. (2011). Experimental and theoretical studies of nanofluid thermal conductivity enhancement: a review. *Nanoscale Research Letters*, *6*(1), 229. Springer Open Ltd. doi: 10.1186/1556-276X-6-229.

Kumar, S., & Tien, C.L. (1990). Dependent absorption and extinction of radiation by small particles. *Journal of Heat Transfer (Transactions of the ASME (American Society of Mechanical Engineers), Series C); (United States)*, *112:1*. Retrieved May 7, 2011, from http://www.osti.gov/energycitations/product.biblio.jsp?osti_id=6018600.

Kumar, S.A., Meenakshi, K, Narashimahan, B.R.V., Srikanth, S., Arthanareeswaran, G. (2009). Synthesis and characterization of copper nanofluid by a novel one-step method. *Materials Chemistry and Physics*, *113*, 57-62. doi: 10.1016/j.matchemphys.2008.07.027.

Lai, W.-Y. (2010). *Experiments on Laminar Convective Heat Transfer with gamma-Al2O3 Nanofluids*. Arizona State University.

Large, M. (1996). Incoherent reflection processes: a discrete approach. *Optics Communications*, *128*(4-6), 307-314. doi: 10.1016/0030-4018(95)00761-X.

Lee, J., Gharagozloo, P. E., Kolade, B., Eaton, J. K., & Goodson, K. E. (2010). Nanofluid Convection in Microtubes. *Journal of Heat Transfer*, *132*(9), 092401. doi: 10.1115/1.4001637.

Lee, S., Choi, S. U.-S., Li, S., & Eastman, J. a. (1999). Measuring Thermal Conductivity of Fluids Containing Oxide Nanoparticles. *Journal of Heat Transfer*, *121*(2), 280. doi: 10.1115/1.2825978.

Lenert, A., Zuniga, Y. S. P., & Wang, E. N. (2010). Nanofluid-Based Absorpers for High Temperature Direct Solar Collectors. *IHTC14-22208* (pp. 1-10).

Lewis, N. S. (2007). Toward cost-effective solar energy use. *Science (New York, N.Y.)*, *315*(5813), 798-801. doi: 10.1126/science.1137014.

Liu, D.-W., & Yang, C.-Y. (2007). Effect of Nano-Particles on Pool Boiling Heat Transfer of Refrigerant 141b. *ICNMM2007-30221*. Retrieved October 8, 2010, from http://link.aip.org/link/abstract/ASMECP/v2007/i4272X/p789/s1.

Liu, Z., Xiong, J., & Bao, R. (2007). Boiling heat transfer characteristics of nanofluids in a flat heat pipe evaporator with micro-grooved heating surface. *International Journal of Multiphase Flow*, *33*(12), 1284-1295. doi: 10.1016/j.ijmultiphaseflow.2007.06.009.

M.H., S., Shuai, M. Q., Chen, Z. Q., Li, Q., & Xuan, Y. M. (2007). Study on Pool Boiling Heat Transfer of Nano-Particle Suspensions on Plate Surface. *J. of Enhanced Heat Transfer*, *14*(3), 223-231.

Matsumoto, M., & Tanaka, K. (2008). Nano bubble—Size dependence of surface tension and inside pressure. *Fluid Dynamics Research*, *40*(7-8), 546-553. doi: 10.1016/j.fluiddyn.2007.12.006.

Merabia, S., Keblinski, P., Joly, L., Lewis, L. J., & Barrat, J.-louis. (2009). Critical heat flux around strongly heated nanoparticles. *Heat and Mass Transfer*, 1-4. doi: 10.1103/PhysRevE.79.021404.

Mikic, B. B., & Rohsenow, W. M. (1969). ON BUBBLE GROWTH. *Growth (Lakeland)*, (October), 657-666.

Milanova, D., & Kumar, R. (2005). Role of ions in pool boiling heat transfer of pure and silica nanofluids. *Applied Physics Letters*, *87*(23), 233107. doi: 10.1063/1.2138805.

Miller, F. J., & Koenigsdorff, R. W. (2000). Thermal Modeling of a Small-Particle Solar Central. *Journal of Solar Energy Engineering*, *122*(1), 23-29.

Modest, M. F. (2003). *Radiative Heat Transfer, Second Edition* (p. 860). Academic Press. Retrieved October 9, 2010, from http://www.amazon.com/Radiative-Transfer-Second-Michael-Modest/dp/0125031637.

MTI. (2011). Nanopowders: A-Z. Retrieved May 10, 2011, from MTI Corporation.

NanoAmor. (2010). Catalog of Nanoscale Particulate Materials. Retrieved from http://www.nanoamor.com/cat/catalog_nanoamor.pdf.

Nanomaterials. (2011). Nanotechnology Applications - Nanopowders. Retrieved May 10, 2011, from http://www.nanomaterialscompany.com/.

Narayan, G. P., Anoop, K. B., & Das, Sarit K. (2007). Mechanism of enhancement/deterioration of boiling heat transfer using stable nanoparticle suspensions over vertical tubes. *Journal of Applied Physics*, *102*(7), 074317. doi: 10.1063/1.2794731.

NREL. (2010a). 30-Year Average Monthly Solar Radiation. Retrieved from http://rredc.nrel.gov/solar/old_data/nsrdb/1961-1990/redbook/sum2/state.html.

NREL. (2010b). Measurement and Instrumentation Data Center. Retrieved from http://www.nrel.gov/midc/pfci/.

Otanicar, Todd P., Phelan, P. E., Prasher, R. S., Rosengarten, G., & Taylor, R. a. (2010). Nanofluid-based direct absorption solar collector. *Journal of Renewable and Sustainable Energy*, *2*(3), 033102. doi: 10.1063/1.3429737.

Otanicar, Todd Phillip. (2009). *Direct Absorption Solar Thermal Collectors Utilizing Liquid-Nanoparticle Suspensions*.

Pak, B. C., & Cho, Y. I. (1998). Hydrodynamic and Heat Transfer Study of Fluids with Submicron Metallic Oxide Particles. *Experimental Heat Transfer*, *11*(2), 151-170. Taylor & Francis. doi: 10.1080/08916159808946559.

Palik, E. D. (1997). *Handbook of Optical Constants of Solids, Five-Volume Set: Handbook of Optical Constants of Solids, Volume 3* (p. 999). Academic Press. Retrieved May 3, 2011, from http://www.amazon.com/Handbook-Optical-Constants-Solids-Five-/dp/0125444230.

Pettit, R. B., & Sowell, R. R. (1976). Solar absorptance and emittance properties of several solar coatings. *J. of Vac. Science Technology*, *13*(2), 596-602.

Prasher, R., Song, D., Wang, J., & Phelan, P. (2006). Measurements of nanofluid viscosity and its implications for thermal applications. *Applied Physics Letters*, *89*(13), 133108. doi: 10.1063/1.2356113.

Pylam (2011). Pylam Products, Inc. Retrieved May 15, 2011, from http://www.pylamdyes.com/.

Putnam, S. a, Cahill, D. G., Braun, P. V., Ge, Z., & Shimmin, R. G. (2006). Thermal conductivity of nanoparticle suspensions. *Journal of Applied Physics*, *99*(8), 084308. doi: 10.1063/1.2189933.

Putra, N., Roetzel, W., & Das, Sarit K. (2003). Natural convection of nano-fluids. *Heat and Mass Transfer*, *39*(8-9), 775-784. doi: 10.1007/s00231-002-0382-z.

Rosenhow, W. M. (1952). A Method of Correlating Heat-Transfer Data for Surface Boiling Liquids. *Trans. of the ASME, 74*, 969-975.

Rusconi, R., Rodari, E., & Piazza, R. (2006). Optical measurements of the thermal properties of nanofluids. *Applied Physics Letters, 89*. doi: 10.1063/1.2425015.

Senapati, P. K., Mishra, B. K., & Parida, a. (2010). Modeling of viscosity for power plant ash slurry at higher concentrations: Effect of solids volume fraction, particle size and hydrodynamic interactions. *Powder Technology*, *197*(1-2), 1-8. Elsevier B.V. doi: 10.1016/j.powtec.2009.07.005.

Shin, D., & Banerjee, D. (2011a). Enhanced Specific Heat of Silica Nanofluid. *Journal of Heat Transfer*, *133*(2), 024501. doi: 10.1115/1.4002600.

Shin, D., & Banerjee, D. (2011b). Enhancement of specific heat capacity of high-temperature silica-nanofluids synthesized in alkali chloride salt eutectics for solar thermal-energy storage applications. *International Journal of Heat and Mass Transfer*, *54*(5-6), 1064-1070. Elsevier Ltd. doi: 10.1016/j.ijheatmasstransfer.2010.11.017.

Sigma-Aldrich. (2010). Nanopowders. Retrieved from http://www.sigmaaldrich.com/materials-science/nanomaterials/nanopowders.html.

Simmons, M. R. (2006). *Twilight in the Desert: The Coming Saudi Oil Shock and the World Economy* (p. 464). Wiley. Retrieved November 12, 2010, from http://www.amazon.com/Twilight-Desert-Coming-Saudi-Economy/dp/0471790184.

Singh, A., Mikic, B.B., Rohsenow, W. M. (1976). Active Sites in Boiling. *Trans. ASME -J. Heat Transfer*, *98*, 401-406.

Solutia. (2010). Therminol VP-1. Retrieved from , http://www.therminol.com/pages/products/vp-1.asp.

Steinfeld, A., & Schubnell, M. (1993). Optimum Aperature Size and Opertating Temperature of a Solar Cavity. *Solar Energy*, *50*(1), 19-25.

Thirugnanasambandam, M., Iniyan, S., & Goic, R. (2010). A review of solar thermal technologies☆. *Renewable and Sustainable Energy Reviews*, *14*(1), 312-322. doi: 10.1016/j.rser.2009.07.014.

Tien, C L. (1988). Thermal Radiation in Packed and Fluidized Beds. *Trans. of the ASME*, *110*, 1230-1242.

Towers, P., Gonzalez-aguilar, R. O., & R, S. (2007). *PS 10 and PS 20 Power Towers in Seville, Spain*.

Trisaksri, V., & Wongwises, S. (2007). Critical review of heat transfer characteristics of nanofluids. *Renewable and Sustainable Energy Reviews*, *11*, 512-523. doi: 10.1016/j.rser.2005.01.010.

Truong, B. H. (2007). Determination of Pool Boiling Critical Heat Flux Enhancement in Nanofluids. Massachusetts Institute of Technology.

Tu, J., Dinh, N., & Theofanous, T. (2004). An experimental study of nanofluid boiling heat transfer. *6th Int. Symposium on Heat Transfer* (pp. 441-446).

Tyagi, H. (2008). *Radiative and combustion properties of nanoparticle-laden liquids*. Arizona State University.

Vassallo, P. (2004). Pool boiling heat transfer experiments in silica–water nano-fluids. *International Journal of Heat and Mass Transfer*, *47*(2), 407-411. doi: 10.1016/S0017-9310(03)00361-2.

Venerus, D. C., Kabadi, M. S., Lee, Sunmook, & Perez-luna, V. (2006). Study of thermal transport in nanoparticle suspensions using forced Rayleigh scattering. *Journal of Applied Physics*, *100*. doi: 10.1063/1.2360378.

Volz, S. (2010). *Thermal Nanosystems and Nanomaterials* (p. 587). New York, New York: Springer.

Wen, D. (2008). Mechanisms of thermal nanofluids on enhanced critical heat flux (CHF). *International Journal of Heat and Mass Transfer*, *51*(19-20), 4958-4965. doi: 10.1016/j.ijheatmasstransfer.2008.01.034.

Wen, Dongsheng, & Ding, Y. (2005). Experimental investigation into the pool boiling heat transfer of aqueous based γ-alumina nanofluids. *Journal of Nanoparticle Research*, *7*(2-3), 265-274. doi: 10.1007/s11051-005-3478-9.

Wen, Dongsheng, Ding, Y., & Williams, R. A. (2006). Pool Boiling Heat Transfer of Aqueous TiO2-Based Nanofluids. *J. of Enhanced Heat Transfer*, *13*(3), 231-244.

Williams, W., Buongiorno, Jacopo, & Hu, L.-W. (2008). Experimental Investigation of Turbulent Convective Heat Transfer and Pressure Loss of Alumina/Water and Zirconia/Water Nanoparticle Colloids (Nanofluids) in Horizontal Tubes. *Journal of Heat Transfer*, *130*(4), 042412. doi: 10.1115/1.2818775.

Witharana, S. (2003). *Boiling of Refrigerants on Enhanced Surfaces and Boiling of Nanofluids*.

Yang, X., & Liu, Z.-H. (2010). A Kind of Nanofluid Consisting of Surface-Functionalized Nanoparticles. *Nanoscale research letters*, *5*(8), 1324-1328. doi: 10.1007/s11671-010-9646-6.

You, S M, & Kim, J H. (2003). Effect of nanoparticles on critical heat flux of water in pool boiling heat transfer. *Applied Physics Letters*, *83*(16), 3374-3376. doi: 10.1063/1.1619206.

You, S. M., Kim, J. H., & Kim, K. H. (2003). Effect of nanoparticles on critical heat flux of water in pool boiling heat transfer. *Applied Physics Letters*, *83*(16), 3374. doi: 10.1063/1.1619206.

You, S. M. U. N., Bar-cohen, A., & Simon, T. W. (1990). Boiling Incipience and Nucleate Boiling Heat Transfer of Highly Wetting Dielectric Fluids From

Electronic Materials. *IEEE Transactions on Components, Hybrids, and Manufacturing Technology*, *13*(4), 1032-1039.

Zap-It. (2011). Zap-It Laser Allinement Products. Retrieved May 12, 2011, from http://www.zap-it.com/Departments/Products/ZAP-IT-Paper.aspx.

Zeinaliheris, S., Etemad, S., & Nasresfahany, M. (2006). Experimental investigation of oxide nanofluids laminar flow convective heat transfer. *International Communications in Heat and Mass Transfer*, *33*(4), 529-535. doi: 10.1016/j.icheatmasstransfer.2006.01.005.

Zhou, D. (2004). Heat transfer enhancement of copper nanofluid with acoustic cavitation. *International Journal of Heat and Mass Transfer*, *47*(14-16), 3109-3117. doi: 10.1016/j.ijheatmasstransfer.2004.02.018.

Zhou, S.-Q., & Ni, R. (2008). Measurement of the specific heat capacity of water-based Al2O3 nanofluid. *Applied Physics Letters*, *92*(9), 093123. doi: 10.1063/1.2890431.

Zhu, H.-tao, Lin, Y.-sheng, & Yin, Y.-sheng. (2004). A novel one-step chemical method for preparation of copper nanofluids. *Journal of colloid and interface science*, *277*(1), 100-3. doi: 10.1016/j.jcis.2004.04.026.

Zollinger, H. (2003). *Color Chemistry:Syntheses, Properties, and Applications of Organic Dyes and Pigments* (3rd ed., p. 637). Helvetica Chimica Acta.

Zou, S., Janel, N., & Schatz, G. C. (2004). Silver nanoparticle array structures that produce remarkably narrow plasmon lineshapes. *The Journal of chemical physics*, *120*(23), 10871-5. doi: 10.1063/1.176074